Universität Hamburg

DER FORSCHUNG | DER LEHRE | DER BILDUNG

Velocity-Map Imaging for Emittance Characterization of Field Emitter Arrays

Dissertation

zur Erlangung des Doktorgrades

an der Fakultät für Mathematik, Informatik und Naturwissenschaften

Fachbereich Physik

der Universität Hamburg

vorgelegt von

Hong Ye

Hamburg

2018

Gutachter:	Prof. Dr. Franz X. Kärtner
	Prof. Dr. Jochen Küpper
Prüfungskommission:	Prof. Dr. Franz X. Kärtner
	Prof. Dr. Jochen Küpper
	Prof. Dr. Henry N. Chapman
	Prof. Dr. Wilfried L. Wurth
	Prof. Dr. Daniela Pfannkuche
Datum der Disputation:	October 18, 2018

Acknowledgments

I am eternally indebted to my family who has supported and encouraged me for pursuing my dreams. I am very grateful to Prof. Dr. Franz X. Kärtner and Prof. Dr. Jochen Küpper for the great supervision, which has opened my mind, broadened my perspective, and benefited me greatly from the collaboration. I would like to extend my gratitude to my colleagues, Dr. Sebastian Trippel, Dr. Oliver D. Mücke, Dr. Arya Fallahi, Dr. Michele Di Fraia, and Dr. Phillip Donald Keathley, for unlimited sharing the profound knowledge with me; without your supervision, this work may not have been realized. I gratefully acknowledge the great laser support from Giulio Maria Rossi, Dr. Liwei Song, Dr. Yudong Yang, and Dr. Giovanni Cirmi; the helpful discussions with Dr. Dongfang Zhang, Dr. Jens S. Kienitz, Dr. Nele Müller, Dr. Guoqing Chang, and Dr. Nicolas Tancogne-Dejean; the expert technical support of Thomas Tilp; and the dedicated administrative support of our respectable group secretary Christine Berber. Finally, I thank all those who appear in my life and raise me up to who I am today.

Abstract

Electron beams of high quality, e.g., low emittance, are of crucial importance for cutting-edge scientific instruments, such as x-ray free electron lasers (XFELs) and ultrafast electron diffraction (UED) setups. A velocity-map-imaging spectrometer is demonstrated to characterize the normalized transverse emittance of photoemitted electron bunches. The spectrometer operated in both, spatial map imaging (SMI) and VMI modes. Therefore, spatial- and velocity-coordinates were recorded independently and quickly. The technique allows for fast complete emittance measurements, within minutes.

The two-dimensional (2D) projected velocity distribution images of photoemitted electrons are recorded by the detection system and analyzed to obtain the normalized transverse emittance. With the presented distribution function of the electron photoemission angles a mathematical method is implemented to reconstruct the three-dimensional (3D) velocity distribution curve. As a first example, multiphoton emission from a planar Au surface is studied via irradiation at a glancing angle by intense 45 fs laser pulses at a central wavelength of 800 nm. The reconstructed energy distribution agrees very well with the Berglund-Spicer theory of photoemission. The normalized transverse emittance of the intrinsic electron bunch is characterized to be 128 and 14 nm·rad in X- and Y-directions, respectively.

The 500 nm and 75 µm spacing Au-nanorod arrays, with nanorods itself of dimension 100×30 nm, were studied. For the one spaced by 500 nm, the same 4-th order photon emission has been observed as for the planar Au surface. The broad transverse velocity spread is contributed by the electrons photoemitted from the nanorod sidewalls. A patterned electron bunch was observed from the 75 µm spacing Au-nanorod array, each emitted from a single nanorod within the array. In the tunneling regime, upon photoemission, an electron is steered by the laser field resulting in fascinating physics. An energy plateau due to the re-scattering electrons was observed in the tunneling regime. A polarization dependent photoemission study was performed showing a smaller rms-normalized divergence of 0.8 mrad with the laser polarization normal to the sample surface, compared to 1.15 mrad while the polarization is parallel.

The demonstrated imaging spectrometer opens up new opportunities in the study of correlated electron emission from solid state. Meanwhile, the electron emission from a single nanotip or field emitter arrays, which are predicted to provide high-current low-emittance coherent electron bunches, foster the further development of free electron lasers, ultrafast electron microscopy and diffraction instruments.

Zusammenfassung

Elektronenstrahlen von hoher Qualität, z. B. mit einer geringen Emittanz, sind von entscheidender Bedeutung für neue, wegbereitende wissenschaftliche Instrumente wie Freie-Elektronen-Laser im Röntgen-Bereich (XFELs) sowie Versuchsaufbauten zur ultraschnellen Elektronenbeugung. In dieser Arbeit wurde ein Spektrometer entwickelt, um die normierte transversale Emittanz von photoemittierten Elektronenpaketen zu messen. Das Spektrometer kann in zwei Modi betrieben werden. Dies erlaubt es, sowohl die räumlichen Anfangsbedingungen als auch die transversale Geschwindigkeit der emittierten Elektronen bei der Geburt zu bestimmen. Die Technik ermöglicht eine vollständige Bestimmung der Emittanz innerhalb weniger Minuten.

Die zweidimensionale (2D) projizierte Geschwindigkeitsverteilung von photoemittierten Elektronen wurde gemessen und analysiert, um die normalisierte transversale Emittanz zu erhalten. Mit Hilfe der in der Arbeit dargestellten Verteilungsfunktion der Elektronen-Photoemissionswinkel wurde eine mathematische Methode implementiert, um die dreidimensionale (3D) Geschwindigkeitsverteilungskurve zu rekonstruieren. Als ein erstes Beispiel wird die Multiphotonenemission von einer planaren Gold- Oberfläche durch Bestrahlung unter einem Glanzwinkel mit intensiven 45-fs-Laserpulse, bei einer zentralen Wellenlänge von 800 nm untersucht. Die rekonstruierte Energieverteilung stimmt sehr gut mit der Berglund-Spicer-Theorie der Photoemission überein. Die normierte transversale Emittanz des intrinsischen Elektronenpaketes wurde auf 128 and 14 nm·rad in X- and Y-Richtung bestimmt.

In dieser Arbeit wurden 100×30 nm große Au-Nanostäbchen-Arrays mit Abständen zwischen den Stäbchen von 500 nm und 75 nm untersucht. Für die Arrays mit 500 nm Abstand wurde, wie im Fall der planaren Gold-Oberfläche, eine vierte nichtlineare Ordnung Photonenemission gemessen. Die breite transversale Geschwindigkeitsverteilung hat Beiträge von Elektronen, die von den Seitenwänden der Stäbchen emittiert werden. Ein räumlich strukturiertes Elektronenpaket wurde von der Gold-Nanostäbchen-Anordnung mit dem Abstand von 75 nm beobachtet. Die Elektronen wurden jeweils von einem einzelnen Nanostäbchen innerhalb der Anordnung emittiert.

Im Tunnelregime, direkt nach der Photoemission, wird ein Elektron durch das Laserfeld angetrieben, was zu faszinierender Physik führt. Ein Energieplateau aufgrund der zurückstreuenden Elektronen wurde im Tunnelregime in dieser Arbeit beobachtet. Es wurde eine polarisationsabhängige Photoemissionsstudie durchgeführt, die eine Standardabweichung der normalisierten Divergenz von 1.15 µm aufweist, wenn das Laserfeld senkrecht zur Probenoberfläche polarisiert ist. Im parallelen Fall wurde eine kleinere Standardabweichung der normalisierten Divergenz von 0.8 µm ermittelt.

Das demonstrierte Spektrometer eröffnet neue Möglichkeiten für die Unter-

suchung korrelierter Elektronenemissionen aus Festkörpern. Währenddessen fördert die Elektronenemission von einzelnen Nanospitzen- oder Feldemitterarrays, von denen vorhergesagt wurde, dass sie kohärente Elektronenpakete mit hohem Strom und niedriger Emittanz bereitstellen, die Weiterentwicklung von Freie-Elektronen-Lasern, ultraschnellen Elektronenmikroskopen und Elektronenbeugungsinstrumenten.

Contents

List of Figures

List of Tables

Chapter 1

Introduction

The quest to build modern particle accelerators began in 1911 when Rutherford discovered the atomic nuclei inside the atom. Since then, the technology of particle accelerator has been rapidly evolving to enable access to energetic particle beams with ever-higher qualities, which has led to significant advancements in the field of science and technology. As one of the elementary particles, high-quality electron beams are essential for successful operation of stupendous current and proposed electron accelerator applications, such as x-ray free electron lasers (FELs) [1, 2, 3], inverse Compton scattering (ICS) devices [4], as well as ultrafast electron diffraction (UED) [5] and microscopies (UEM).

Free-electron lasers (FELs), invented by John Madey [6] and first experimentally demonstrated by his group at Stanford [7, 8] in the 1970s, are of great interest in the production of high power, ultra-short, coherent photons with tunable wavelength [2]. High-gain FELs, e.g., Linac Coherent Light Source (LCLS) [9], SwissFEL [10] and the European XFEL, operated in self-amplified spontaneous emission (SASE) mode, have delivered coherent laser pulses with ultrahigh photon flux, ultrashort pulse durations and wavelengths down to Ångström level. The extremely bright and coherent x-ray FEL light sources have revolutionized the time-resolved x-ray imaging technique with picometer-femtosecond spatial-temporal resolution, which enables capturing real-time movies of dynamics from both transient molecular structure and condensed phase at their characteristic spatial and temporal scales [11, 12, 13, 14, 15, 16, 17]. The accessibility of different time and length scales by different light sources together with the typical time scales and length scales of physical, chemical, and biological processes is shown in Fig. 1.1 [18]. A review of the scientific results obtained from LCLS during its first five operation years, covering broad fields of physics, chemistry, biology and material sciences, is provided in Ref. [18]. The prospects of the x-ray FEL developments converge to the improvement of the spatial-temporal resolution and coherence, which determinately rely on the electron beam quality. A key measure of electron beam quality is the electron beam

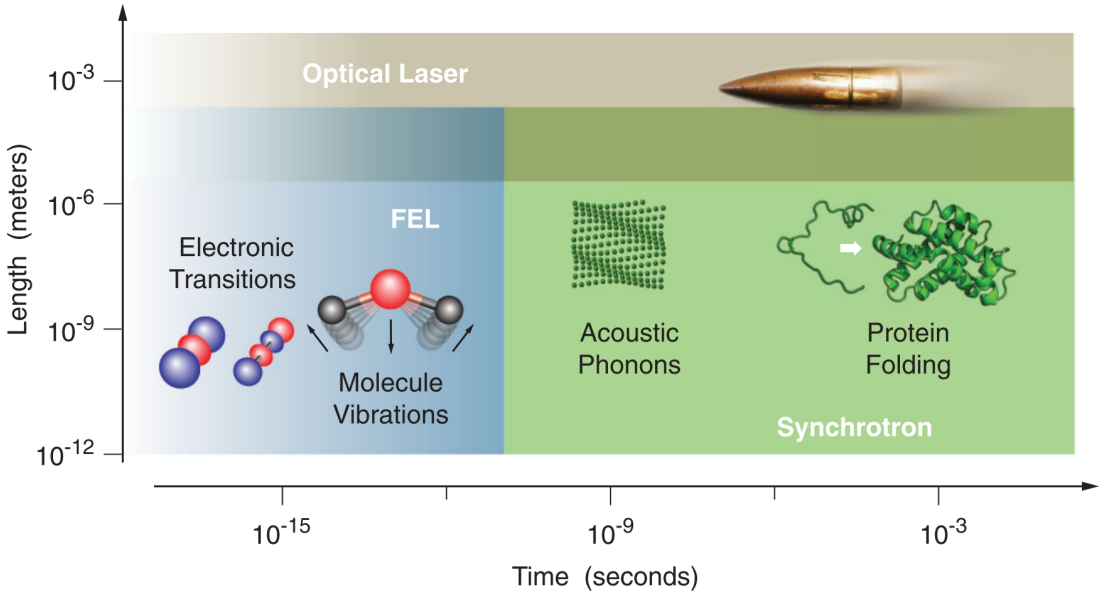

Figure 1.1: Schematics of typical time scales and length scales of physical, chemical, and biological processes. Shaded regions indicate the time scales and length scales accessed by different light sources. Taken from [18].

emittance, denoted as $\varepsilon_{x,y}$, which is the occupied area by an electron beam in a position-and-momentum phase space. According to the derivation from Kim [19], the rule-of-thumb criterion to operate a high-gain FEL is given by $\varepsilon_{x,y} \leqslant \lambda/4\pi$, which predicts the minimum wavelength λ achievable vigorously depends on the emittance. An electron beam of relatively low charge is preferred since it is usually accompanied by low emittance, therefore providing an easier way to achieve the shorter wavelength operation for a given beam energy. Simulations have shown promising results of implementing high quality electron bunches with relative low charge of $\sim$1 pC to achieve sub-femtosecond gigavolts-peak-power single coherent pulses at a wavelength of 1.5 Å [20].

Further reducing the operation wavelength to γ-ray regime opens up unprecedented opportunities for new science. There are, however, fundamental problems, i.e., random recoils of the electrons while emitting photons degrading the beam emittance, impeding FEL lasing action and making FEL operation at such short wavelengths very difficult. ICS of laser photons by an ultra-relativistic electron beam complements the laser synchrotron sources (LSS), enabling the generation of sub-picosecond x- to γ-ray pulses while preserving the initial polarization of the laser field [4]. Numerous applications, e.g., remote sensing of nuclear materials [21], continuously demand for optimized ICS sources operated at high-brightness MeV γ-ray. Recently, generation of partially coherent radiation from an ICS source (usually incoherent) has been proposed through emittance exchange of an advanced

electron beam, i.e., an array of electron beamlets emitted from a nanostructured field emitter array [22].

High-quality electron beams also find direct applications in state-of-the-art electron scattering instruments, such as as UED/UEM [23, 24, 25, 26]. In a scattering experiment, the scattering cross-section of electron beams is orders of magnitude larger than that of x-rays, which makes electron beams an excellent probe to reveal structures of gas specimens and thin crystal samples. In addition, electron beams are less damaging to specimen per useful elastic scattering event. Therefore, electron beams with short wavelengths ($\leqslant$ 1 Å) and pulse durations ($\leqslant$ 100 fs) grant strong capabilities to visualize structural changes at atomic length and femtosecond time scales.

Particle accelerators with accelerating field gradients orders-of-magnitude greater than present systems, that are on the order of MV/m, are needed for continuous explorations of particle physics at the energy frontier in the long term. Such advanced accelerators hold promise to dramatically reduce the cost and size of high energy colliders and synchrotron light sources. It allows compact light sources accessible to smaller laboratories, which may help relieve the existent situation that users must go through a highly competitive process to gain access to the x-ray FEL facilities, for severely restricted amount of beam time. The techniques alternatively approaching the high-gradient accelerating field are generally divided into the wake-filed and laser acceleration schemes. In the former method, multi GV/m acceleration gradients are realized by laser induced wake-fields in plasma [27]. Another way to approach the high-gradient acceleration is dielectric laser acceleration (DLA), in which infrared lasers are coupled to optical-scale lithographically fabricated dielectric structures to excite peak surface electric fields on the order of GV/m [28]. The ongoing project, AXSIS: exploring the frontiers in attosecond X-ray science, imaging and spectroscopy, extends the DLA technique utilizing the THz as the driving acceleration field [29]. Fig. 1.2 shows a schematic beamline of AXSIS, starting from nicely patterned electron beamlets, termed as "free-electron crystal". A compact, fully coherent, THz-driven attosecond x-ray source based on coherent ICS off a free-electron crystal is aimed to be developed. The monolayer of the 2D crystalline beamlets is structured as a result of the photoemission from an array of nanostructured emitters. The other dimension comes from the oscillation of the laser field according to the mechanisms of the field emission, which only happens close to the maximum field strength. The idea is to have an arranged electron bunch from 500 nm spacing field emitter array (FEA) strong-field emitted under a 50×50 μm^2 laser spot size. Let assume one electron emitted per laser cycle per nanoparticle, one would obtain a 10 fC electron bunch from a 10 cycle laser pulse, e. g., a 30 fs 800 nm laser pulse. To keep the crystalline structure of the electron bunch is very challenge. A THz gun, with a peak acceleration field of 600 MV/m, is designed to accelerate the free-electron crystal to sub-relativistic speed in 15 fs [30]

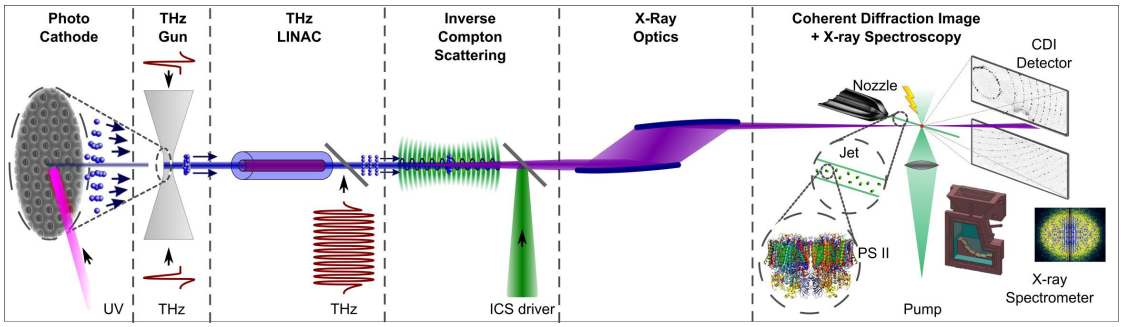

Figure 1.2: Schematic layout of the AXSIS setup currently under construction at DESY in Hamburg. Figure taken from Ref. [29].

and preserve the electron beam to the THz linac system for the further acceleration to the relativistic speed. To be able to resolve each individual beamlet right at the output of the THz gun, the beam divergence needs to be smaller than 6 meV if the initial beamlets are separated 500 nm away. Overall, the emittance, in terms of the size and divergence of each beamlet, is the crucial point to approach the goal, which directly motivates the investigation of generation of ultra-low emittance electron beams and further more patterned beamlets in this thesis work.

The overwhelming importance of high-quality (e. g., ultra-low emittance) electron beams in cutting-edge scientific instruments has driven the strive towards the development and the characterization of the electron sources. The emittance of an electron beam is finalized nascent at the cathode undergoing an emission process and degrade only afterwards. Therefore, investigation of the intrinsic electron beam emittance from the cathode becomes an imperative task. The fundamental lower limit of the beam emittance is determined by the electron temperature of the emission process [31]. Consequently, the emittance is often called the thermal emittance. In general, the emission mechanism are classified as three fundamental processes, i. e., thermionic emission, photoelectric emission and field emission. Strictly speaking, thermal emittance should only refer to the thermionic emission. However, commonly in the accelerator community, the concept of thermal emittance applies to all three fundamental emission processes. Thermionic emission was observed by Richardson in 1929, accounting the pure electron emission over the barrier taking place at electric field strength below 1 MV/m. Although thermionic electron sources provide large enough beam currents for electron diffraction applications and are easily available, the deficient beam quality and the insufficient temporal resolution of milliseconds limit the number of applications of thermionic sources. Therefore, in this dissertation, the work is focused on the latter two emission processes driven by the intense laser field, as photoelectric emission implemented to the experimental results of planar Au surface as a proof-of-principle of the emittance measurement discussed in chapter 4, and

field emission to interpret the experimental results from an array of Au nanorods aiming to develop the patterned electron beamlets with low emittance discussed in chapter 5. Moreover, a stricter term intrinsic emittance is used to described beam emittance obtained at the photocathode.

To decrease the intrinsic emittance, in principle, one needs to decrease either the emission area or the momentum spread. The former can be intuitively decreased by an extremely tight focal spot size or sharp tip surface, which geometrically limits the emission area. For instruments with electron beam charge $\leq$1 pC such as UEDs and UEMs, improvement of emittance by an order of magnitude can be achieved by reducing the size of the emission source to sub-micron levels, which can be realized by either restricting the physical dimensions of the emitter or focusing the laser by an optical system with a large numerical aperture. Another important pathway is to reduce the momentum/energy spread, simply referring to the mean transverse energy (MTE) distribution, of the electrons emitted from a cathode. By choosing a proper material with appropriate work function and irradiating it by a laser beam with matched photon energy, for example the photoemission of Cu under 266-nm laser irradiation, is expected to help. Further reduction is expected when entering the strong-field emission regime, where the electrons are considered to adiabatically tunnel through the surface barrier with zero initial momentum and are then driven by the instantaneous optical near field [32]. Under these conditions electrons are expected to be emitted with a relatively small divergence angle and significantly lower transverse momentum spread. Recently, nanostructured and plasmonic photocathodes under multiphoton or strong-field optical emission have been used as improved electron sources [29, 33, 34, 35, 36].

Meanwhile, accurate and fast characterization of the electron beam emittance is indispensable to assess various approaches in order to improve the emittance of the underlying electron source, which motivates the velocity-map-imaging (VMI) spectrometer demonstrated here, of which the details are described in chapter 3. The VMI spectrometer allows us to directly access the transverse momentum distribution of photoemitted electrons with an energy resolution of 0.02 meV in the imaging center, and the fast measurement of normalized transverse emittance within minutes.

To conclude, both the experimental characterization and the theoretical interpretation to quantify electron beam emittance as a function of photocathode material and morphology are highly important. The means to push ahead the limits of electron-based techniques is by advancing the electron source, which addresses the main goal of this Ph.D. work.

Outline of this dissertation

- Chapter 1 introduces the background and the motivation of this dissertation, meantime specifies the desire for low-emittance electron bunches, and gives an overview of this thesis.
- Chapter 2 provides both an introduction to the photoemission mechanisms along with the theoretical models and a brief description of the electron beam properties, highlights the important concept of electron bunch emittance and raises the demands on the direct access to the emittance measurement.
- Chapter 3 demonstrates the velocity-map-imaging spectrometer constructed in the laboratory in great details. A photocathode of planar Au surface was used to comprehensively calibrate the spectrometer.
- Chapter 4 discusses the experimental results from the planar Au surface, presents a mathematic algorithm for reconstructing the three-dimensional energy distribution, and benchmarks the performance of the VMI spectrometer on solid state samples.
- Chapter 5 deals with the recent experimental results obtained from Au-nanorod arrays, showing the promise of generating patterned electron bunches.
- Chapter 6 serves as a summary and gives an outlook to future investigations.

Chapter 2

Fundamental Concepts

This chapter covers the fundamental concepts required for this thesis study. The concepts are categorized into two sections: §2.1 emission mechanisms and §2.2 electron beam properties. In the first section, we introduce the two significant photoemission mechanisms: the photoelectric emission and the field emission. The semi-classical theoretical models, i. e., the Fowler-Dubridge model and Berglund-Spicer three-step model, are included to discuss the physics of the photoelectric emission, as well as the Fowler-Nordheim equation, which is well established for the field emission regime. The subsequent motion of electrons upon tunneling in a laser near field is discussed in §2.1.6, giving rise to the plateau and cut-off in the photoelectron energy spectrum. In the second, the properties of an electron beam are briefly reviewed. The phase-space formalism is introduced in §2.2.1. The concepts of beam emittance, peak current and beam brightness are illustrated in §2.2.2. A brief discussion of space charge effect and coherence length are given in §2.2.3 and §2.2.4. In the end, the state-of-the-art emittance measurement techniques are summarized in §2.2.5.

2.1 Emission mechanisms

2.1.1 Photoelectric emission

In 1887, the German physicist Heinrich Hertz observed that the sparks enhanced when electrodes were illuminated with ultraviolet light [62]. In 1905, Einstein discovered the law of the photoelectric effect and explained the experimental phenomenon on a quantum level, advancing the hypothesis that light energy is carried in discrete quantized packets [63], a work which earned him the Nobel Prize in Physics in 1921.

The mechanism of the photoelectric effect is sketched three steps in Fig. 2.1(a). A photon promotes an electron from an occupied state in the metal to a free

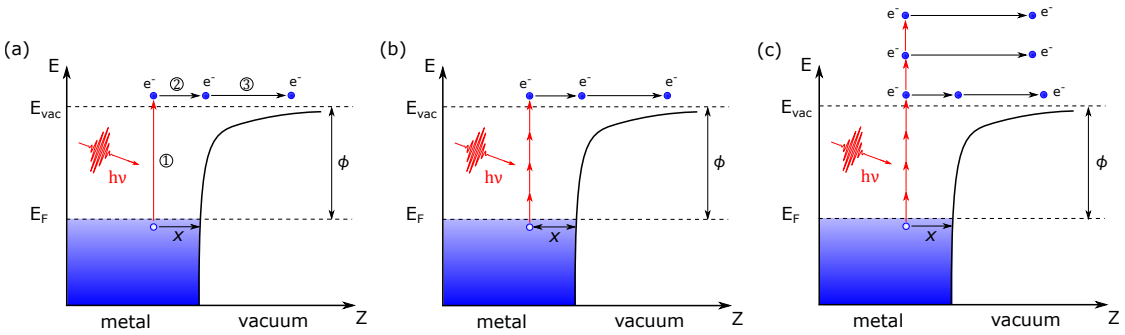

Figure 2.1: (a) Photoelectric effect. The three-step model describes the process by step ①: absorption a photon; step ②: electrons move to the surface; and step ③: electrons escape to vacuum. (b) Multiphoton emission. (c) Above-threshold emission. E_{vac} the vacuum level, E_{F} the Fermi level and ϕ the work function.

continuum state of the surrounding vacuum. In this elementary process, the photon energy $h\nu$ needs to be larger than the metal work function ϕ, typically 3–6 eV [64], to release the electron. Back then, only illumination with UV or higher energy radiation can lead to photoemission via the photoelectric effect. The maximum kinetic energy E_{kin} an emitted electron can attain after escaping is given by $E_{\text{kin}} = h\nu - \phi$. The photoelectric emission was theoretically studied by Berglund and Spicer in 1964 [65, 66, 67, 68]. More details are given in §2.1.3. With the development of modern laser technology, the photon flux is high enough to excite an electron by simultaneous absorption of several photons, known as the multiphoton emission, shown in Fig. 2.1(b). The emission current is well predicted by Fowler-Dubridge model, discussed in §2.1.2. Multiphoton photoemission was first studied in atoms [69, 70]. There are also some electrons which absorb energy from more than the minimum number of photons needed to over come the barrier, leading to a surplus in the kinetic energy, known as above-threshold emission. A physical picture is depicted in Fig. 2.1(c). The excess kinetic energy is quantized by the photon energy, therefore, multiple peaks appear in the resulting electron energy spectrum, nicely demonstrated experimentally in gases [71] and solids [72].

2.1.2 Fowler-Dubridge model

The Fowler-Dubridge model describes the photoelectric emission from a metal based on the Sommerfeld model, which takes into account the thermal agitation of electrons in the metal and predicts the photoelectric yield as function of temperature and the frequency of incident radiation. The Fowler-Dubridge model [73] for the n-th order photoelectric current can be written in a generalized form as

$$J \propto A(1-R)^n \, I^n \, F\left(\frac{nh\nu - e\phi}{kT}\right) \tag{2.1}$$

where n is the number of photons, h is the Planck constant, A is the Richardson coefficient, R the reflection coefficient from the metal surface, I the incident light intensity, ϕ the metal work function, and $F(x) = \int_0^\infty \ln(1 + e^{-(y+x)})\,\mathrm{d}y$ the Fowler function. According to Fowler-Dubridge model, the emission current scales with a power law in laser intensity.

2.1.3 Berglund-Spicer three-step model

As mentioned and shown in Fig. 2.1(a), Berglund and Spicer [65, 66] explained the photoelectric emission using a three-step model. In this model, the first step is the absorption of the incident photon(s) by an electron, described by the two important phenomena of reflectivity and absorption as the photons travel into the cathode. The assumption made here is that the distribution in direction of the excited electrons is isotropic. The second step contains the physics occurring while the electron drifts to the surface. The relevant effects are the electron-electron scattering, electron-phonon scattering *etc.* In this step, only inelastic scattering events are considered. The probability of inelastic scattering can be described in terms of a mean free path $l(E)$, which is a function only of the electron energy, without considering the wave vector $\mathbf{k}$. And the inelastic scattering is isotropic. In the third step the primary phenomenon is the abrupt change in electron angle across the metal-vacuum interface, determining the angular cone of escaping electrons. In order to escape over the surface barrier, the electron must have a component of its total momentum p_{total}, perpendicular to the surface which is greater than some critical value p_c in metal, i. e., the effective work function lowered by the Schottky effect. And the transverse component is conserved. A brief summary of the theoretical derivation is given in the following.

The electrons are excited from filled states in the valence band to empty states in the conduction band. According to the assumptions, the transition probability depends only on the density of states (DOS) at energy $E - h\nu$ in the valence band $N_{\mathrm{V}}(E - h\nu)$ and the DOS at energy E in conduction band $N_{\mathrm{C}}(E)$. The generation rate $G(E, x, h\nu)$ at depth x and energy E is given by

$$G(E, x, h\nu) = I \cdot (1 - R) \cdot \alpha(\nu) \cdot e^{-\alpha(\nu)x} \cdot \frac{N_{\mathrm{C}}(E) \cdot N_{\mathrm{V}}(E - h\nu)}{\int_{E_{\mathrm{F}}}^{E_{\mathrm{F}}+h\nu} N_{\mathrm{C}}(E) \cdot N_{\mathrm{V}}(E - h\nu) \cdot \mathrm{d}E} \quad (2.2)$$

where I is the incident photon flux, R is the reflectivity at normal incidence, and $\alpha(\nu)$ is the absorption coefficient of a solid at frequency ν defined as $\alpha(\nu) = \int_0^\infty \alpha_\nu(E)\,\mathrm{d}E$. Introducing

$$G_0(E) = \alpha_\nu(E) \cdot \frac{N_{\mathrm{C}}(E) \cdot N_{\mathrm{V}}(E - h\nu)}{\int_{E_{\mathrm{F}}}^{E_{\mathrm{F}}+h\nu} N_{\mathrm{C}}(E) \cdot N_{\mathrm{V}}(E - h\nu) \cdot \mathrm{d}E} \quad (2.3)$$

Thus

$$G(E, x, h\nu) = I \cdot (1 - R) \cdot e^{-\alpha(\nu)x}\,\mathrm{d}x \cdot G_0(E)\,\mathrm{d}E \quad (2.4)$$

The fraction of electrons, within the solid angle between φ and $\varphi + \mathrm{d}\varphi$, can escape after traveling a distance $x/\cos\varphi$, is given by

$$F(E,x) = \frac{1}{2} \cdot \int_{\varphi=0}^{\varphi_0} e^{\frac{-x}{l(E)\cdot\cos\varphi}} \cdot \sin\varphi \cdot \mathrm{d}\varphi \tag{2.5}$$

where φ_0 is defined as the maximum angle that the electron can escape over the surface barrier, which will be discussed more in §4.1. The total number of electrons escaped without inelastic scattering is given by

$$n(E,x,h\nu) = G(E,x,h\nu)F(E,x) \tag{2.6}$$

Integrating all possible values of x, we obtain the number of electrons photoemitted at energy E normalized to the absorbed photon flux $I_0 = I \cdot (1-R)$ as

$$N(E,h\nu) = \frac{\int_{x=0}^{\infty} G(E,x,h\nu)F(E,x)dx}{I\cdot(1-R)} \tag{2.7}$$

which is named the energy distribution curve (EDC), quantitatively expressing the number of electrons photoemitted at energy E. Substituting Eq. (2.3)–Eq. (2.6) into Eq. (2.7), the EDC is written as

$$N(E,h\nu) = \frac{G_0(E)dE}{2\cdot\alpha(\nu)} \cdot \left((1-\cos\varphi_0) - \frac{1}{\alpha l(E)} \cdot \ln\frac{\alpha l(E)+1}{\alpha l(E)\cos\varphi_0 + 1} \right) \tag{2.8}$$

Expand the logarithm term $-\frac{1}{\alpha l(E)} \ln\frac{\alpha l(E)+1}{\alpha l(E)\cos\varphi_0+1}$ with a Taylor expansion and introducing the threshold function defined as $C(E) = \frac{1}{2}(1-\cos\varphi_0)$, shown in Fig. 2.2, we obtain

$$N(E,h\nu) = \frac{1}{2}G_0(E)dE \cdot \frac{(1-\cos\varphi_0)\cdot l}{\alpha l + 1} \cdot K, \tag{2.9}$$

with

$$K = \frac{\alpha l + 1}{\alpha l} - \frac{\alpha l + 1}{2C(E)(\alpha l)^2} \ln\frac{\alpha l + 1}{\alpha l + 1 - 2\alpha l C(E)} \tag{2.10}$$

defined as the correction factor giving the adjustment that must be made when the angular distribution of electrons is taken into account. As plotted in Fig. 2.3, for any values of αl and $C(E)$, the correction factor can vary only between 0.5 and 1.

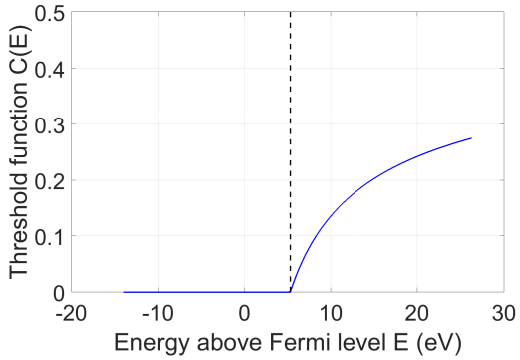

Figure 2.2: Threshold function $C(E)$

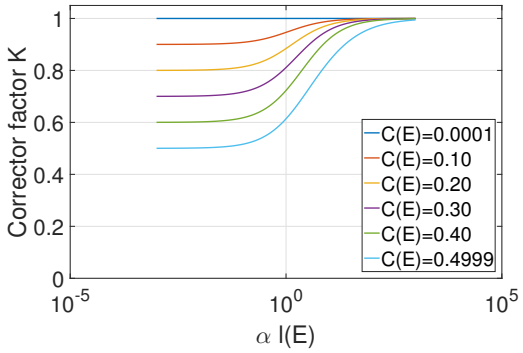

Figure 2.3: Correction factor K

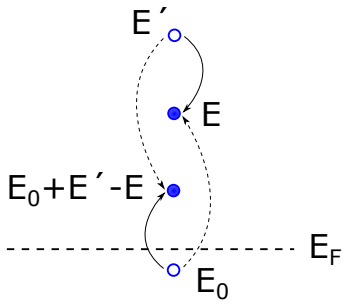

Figure 2.4: A diagram showing electron-electron scattering processes.

The probability of electron escape after one inelastic scattering once can be derived in a way similar to that for electron escape without scattering. Consider an electron excited to energy E' at distance x from the photoemitting surface, the rate of escape of electrons, which do not scatter and those which scatter once, with energy between E and $E + \mathrm{d}E$, is given by

$$N(E)\,\mathrm{d}E = \frac{KC(E)\,\mathrm{d}E \cdot l}{\alpha l + 1}\left[G_0(E) + \int_E^\infty \frac{1}{2}\left[\frac{1}{\alpha l'}\ln(1+\alpha l') + \frac{l}{l'}\ln(1+\frac{l'}{l})\right] \cdot p_2 \cdot G_0(E')\,\mathrm{d}E'\right] \tag{2.11}$$

where $l'(E)$ is the mean free path for inelastic scattering of an electron with kinetic energy E'. And p_2 is the probability that this electron will be scattered to an energy between E and $E + \mathrm{d}E$, depending on the scattering mechanism. For a particular case, the electron-electron scattering, shown in Fig. 2.4, as an important inelastic-scattering mechanism in metals holds a probability p_2, denote as $p_{\text{e-e}}$, given by

$$p_{\text{e-e}} = \frac{2p_s(E', E)dE}{\int_0^\infty p_s(E', E)dE} \tag{2.12}$$

with

$$p_s(E', E)dE = \int_0^\infty (2\pi/\hbar)\mathrm{DOS}(E_0)\mathrm{DOS}(E)\mathrm{DOS}(E_0 + E' - E) \times f_{\mathrm{FD}}(E_0)[1 - f_{\mathrm{FD}}(E)][1 - f_{\mathrm{FD}}(E_0 + E' - E)]dE_0 dE \tag{2.13}$$

where $f_{\mathrm{FD}}(E)$ is the Fermi-Dirac function. Substituting $p_{\text{e-e}}$ in to Eq. (2.11), the energy distribution curve, considering only primary electrons and those which scatter once with another electron is obtained. To simplify, we assume $\alpha l' \ll 1$, $l'/l \ll 1$ and the Fermi-Dirac function at absolute zero, the EDC is given by

$$N(E)\,\mathrm{d}E = \frac{KC(E)dE \cdot l}{\alpha l + 1}\left[G_0(E) + 2\int_E^{E_F + h\nu} \frac{p_s(E', E)dE}{P_s(E')} G_0(E')dE'\right] \tag{2.14}$$

This equation is later employed in §4.3 to explicate the experimental energy distribution of the photoemitted electrons from planar Au surface. For exhaustive

theoretical derivations, we refer the reader to [65] and [66]. Moreover, in §4.1, we extend the Berglund-Spicer model in order to derive the angular distribution of photoemitted electrons for data analyzing and reconstruction.

2.1.4 Field emission

Besides the photoelectric emission, another important emission process studied in this dissertation is field emission. The emission process strongly depends on the optical electric field instead of the laser intensity, compassing numerous interesting physical phenomena. Field emission, also known as cold field emission, is a process whereby an electron close to the Fermi level tunnels through a barrier into vacuum in the presence of a high electric field. This process becomes predominant when the field strength is on the order of GV/m. A sketch of field emission is shown in Fig. 2.5(a). The external electrostatic field F at the metal-vacuum surface modulates the shape of the potential barrier, known as the Schottky effect [85], with the amount of the surface barrier lowered by

$$\phi_{\text{Schottky}} = \sqrt{\frac{e^3 F}{4\pi\epsilon_0}} \tag{2.15}$$

where ϵ_0 is the vacuum permittivity. Typically, ϕ_{Schottky} has values on the order of a few eV at electric fields on the order of GV/m, which is the same order of magnitude as the work function of common metal photocathodes [64]. Instead, in the presence of a strong laser field, the barrier is suppressed each time the oscillating electric field passes its maximum, allowing the electron to tunnel out within a fraction of an optical cycle. This is called light-induced field emission, shown in Fig. 2.5(b).

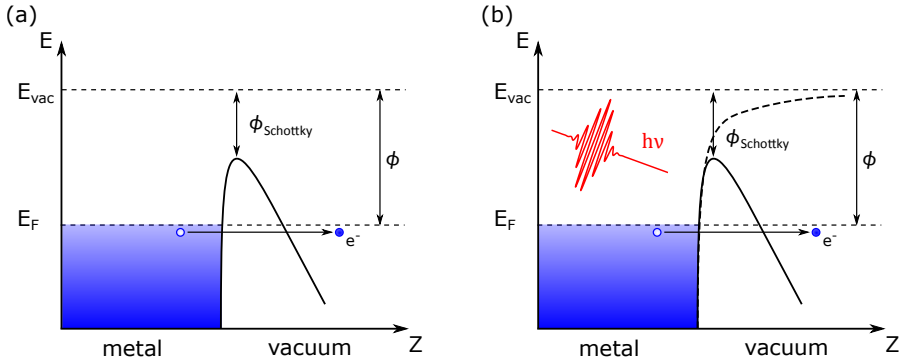

Figure 2.5: Sketch of (a) field emission: an external electrostatic field leads to the formation of a tunneling barrier, which electrons at the Fermi energy E_{F} may tunnel through; (b) light-induced field emission: the strong electric field bends the barrier each time the oscillating electric field passes its maximum, allowing the electron to tunnel out. The barrier is lowered due to the Schottky effect by amount of ϕ_{Schottky}.

2.1.5 Fowler-Nordheim equation

The theoretical explanation of the field emission mechanism has first been proposed by R. H. Fowler and L. Nordheim in 1928 [73], where they used quantum mechanics to study the emission current density dependence on the strength of the present electric field. The tunnel probability was derived from the 1D-time independent Schrödinger equation:

$$-\frac{\hbar^2}{2m^*}\frac{\mathrm{d}^2\Psi}{\mathrm{d}x^2} + U(x)\Psi = E\Psi \tag{2.16}$$

where $U(x)$ is the electron potential energy, E is the total electron energy associated with motion in the x-direction. For the exact triangular barrier $U(x) - E = \phi - eFx$, using the WKB (Wigner, Kramers, Brillouin) approximation [86], the Schrödinger equation can be solved, yielding the tunneling probability under the presence of a strong field expressed as

$$\Theta \propto \exp\left(-\frac{4}{3}\frac{\sqrt{2m^*}}{e\hbar}\frac{\phi^{\frac{3}{2}}}{F}\right) \tag{2.17}$$

where ϕ is the work function of the metal, and F is the electric field. The Fowler-Nordheim equation [87] provides the relation of the tunneling current density to the present electric field strength as

$$J(F) \propto F^2 \exp\left(-\frac{4}{3}\frac{\sqrt{2m^*}}{e\hbar}\frac{\phi^{\frac{3}{2}}}{F}\right) \tag{2.18}$$

The tunneling current therefore depends exponentially on the barrier height to the 3/2 power. To experimentally approach the strong-field regime, studies of field emission demonstrated that micro-protrusions, e. g., surface contaminants, can effectively enhance the field at the emitting surface [88] because the field lines are normal, not to the macroscopic surface, but the microscopic contour of the surface. Other studies have also reported the field enhancement due to the plasmonic enhancement [89, 90]. In these cases, one need to substitute F with $F = \beta_F \cdot F_c$, where β_F is the field enhancement factor and F_c is the external field before enhancement.

2.1.6 Electron rescattering in strong laser fields

Upon tunneling, the electron is still subject to the laser near field and the movement driven by it. A semiclassical model of intense laser-atom interactions, describing this phenomenon, was introduced by Corkum [32], Kulander [91] and Schafer [92], named the three-step model[1]. In this model, an electron first tunnels out the barrier

[1]Please note this is different from the Berglund-Spicer three-step model of photoelectric emission described in §2.1.3

through the light-induced field emission, gaining zero momentum. Once the electron appears at the tunnel exit, it is steered away from the parent atomic or molecular ion by the light wave until the field reverses its direction in about a quarter cycle. Depending on the emission time, most electrons directly move towards the detector undisturbed by the parent ion, while a small fraction of the electrons recollide with the parent ion. Four outcomes are conceivable from interacting with the parent ion [93]: detachment of another electron: non-sequential double ionization (NSDI); excitation of bound electrons upon inelastic collision with the parent ion; energetic photon emission upon the electron recombining into its ground state; and energetic electron emission by elastic backscattering of the electron. Intensive studies have been performed for gas phase targets [93] in the field of attosecond physics. The electron elastically backscattered from the parent matter acquires high kinetic energies, which leads to the formation of a plateau in the energy spectrum and the cutoff energy located at $10.007U_\mathrm{p}+ 0.538\phi$ according to quantum orbit theory [94], where U_p is the ponderomotive energy, i. e., the cycle-averaged quiver energy of a free electron in a strong electromagnetic field.

2.2 Electron beam properties

To systematically characterize electron beam properties upon photoemission, a phase-space formalism is introduced, in which the statistical mechanics over the position-and-canonical-momentum space of an ensemble of electrons is studied. Beam emittance, peak current, beam brightness and coherence length are important quantities derived from the phase-space formalism to characterize the electron beam quality. Based on the theoretical framework, experimental characterization techniques for electron beam properties have been developed over decades, deepening the understanding for generation of high-quality electron beams, as well as preservation of electron beam quality during beam transport.

2.2.1 Phase space for charged particle dynamics

The dynamical state of a charged particle is described in a six-dimension (6D) phase space by its position (x, y, z) and canonical momentum (p_x, p_y, p_z) in a Cartesian coordinate system. The coordinate z denotes the propagation direction, x and y are along the transverse directions. A distribution function $f(x, y, z, p_x, p_y, p_z)$ defined over the phase space is introduced for an ensemble of charged particles, or a *beam*. The distribution function satisfies $\iiint f(x, y, z, p_x, p_y, p_z)dxdydzdp_xdp_ydp_z = 1$. For most accelerator applications, the motions of charged particles among three mutually perpendicular directions can be considered with very good approximation as decoupled. The particle dynamics along each direction can be studied in-

dependently. Therefore, $f(x, y, z, p_x, p_y, p_z) = f(x, p_x)f(y, p_y)f(z, p_z)$. Further, $\int f(w, p_w)\,\mathrm{d}w\,\mathrm{d}w' = 1$, where w stands for x, y or z. Since a charged particle beam is mainly accelerated in the propagation direction z, the *paraxial approximation* is implemented, i.e., $p_z \gg p_{x,y}$ [37]. We define the horizontal and vertical divergence angles as $x' = p_x/p_z$ and $y' = p_y/p_z$, respectively. In the case with no particle energy acceleration, (x, x') and (y, y') are both conjugate variable pairs. As a result, charged particle beam dynamics is conveniently studied over the (x, x') and (y, y') space, or the *trace space*.

In the following sections, major electron beam properties over the transverse directions will be discussed. For simplicity, physical quantities are defined in the horizontal direction, x. Without exception unless mentioned, the definitions also apply for the vertical direction, y.

2.2.2 Emittance, peak current and brightness

Figure 2.6 shows a schematic of a charged particle distribution in the horizontal trace space. According to Liouville's theorem [38], in the absence of dissipative, frictional and collisional forces, the horizontal trace-space area, A_x, is conserved, i.e.,

$$A_x = \int \mathrm{d}x\,\mathrm{d}x' = \text{const.} \tag{2.19}$$

The horizontal beam emittance ε_x, is defined accordingly as

$$\varepsilon_x = \frac{\int \mathrm{d}x\,\mathrm{d}x'}{\pi} = \frac{A_x}{\pi}. \tag{2.20}$$

The above definition for beam emittance only considers the trace-space area occupied by the particles, which does not reflect the particle distribution. This may give misleading estimates for beam quality, as illustrated in Fig. 2.7. To take into account the particle distributions, a statistical emittance is introduced as follows. With the horizontal distribution function $f(x, x')$ which satisfies $\int f(x, x')\,\mathrm{d}x\,\mathrm{d}x' = 1$, the first moments are given by

$$\langle x \rangle = \int x f(x, x')\,\mathrm{d}x\,\mathrm{d}x', \tag{2.21}$$

$$\langle x' \rangle = \int x' f(x, x')\,\mathrm{d}x\,\mathrm{d}x', \tag{2.22}$$

and the second moments by

$$\langle x^2 \rangle = \int (x - \langle x \rangle)^2 f(x, x')\,\mathrm{d}x\,\mathrm{d}x' = {\sigma_x}^2, \tag{2.23}$$

$$\langle x'^2 \rangle = \int (x' - \langle x' \rangle)^2 f(x, x')\,\mathrm{d}x\,\mathrm{d}x' = {\sigma_{x'}}^2, \tag{2.24}$$

$$\langle x x' \rangle = \int (x - \langle x \rangle)(x' - \langle x' \rangle) f(x, x')\,\mathrm{d}x\,\mathrm{d}x' = \sigma_{xx'}, \tag{2.25}$$

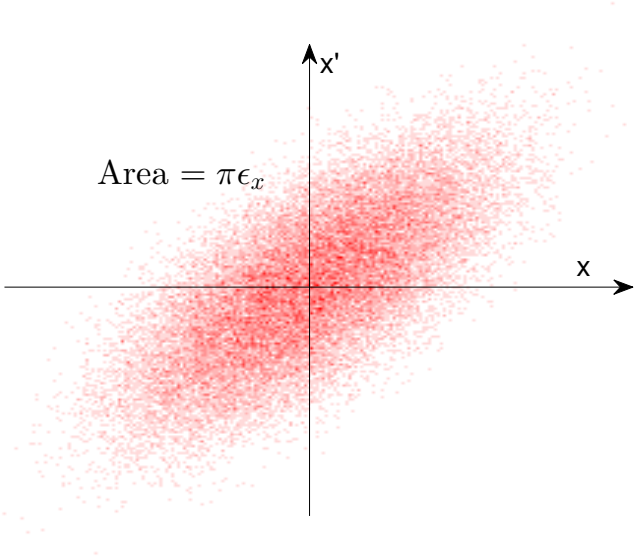

Figure 2.6: Schematic of a charged particle distribution in the horizontal phase space. The phase space area occupied by the beam is equal to $\pi\varepsilon_x$.

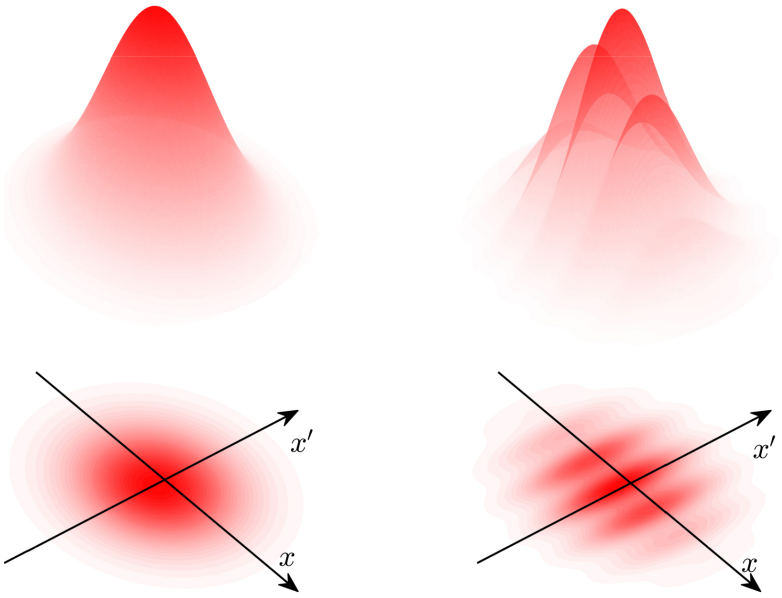

Figure 2.7: A schematic showing two different charged particle distributions in the horizontal phase space but with same occupied area.

where σ_x is the root mean square (rms) horizontal beam size, while σ'_x is the rms horizontal divergence. The horizontal *rms emittance* is defined as

$$\varepsilon_{x,\mathrm{rms}} = \sqrt{\langle x^2 \rangle \langle x'^2 \rangle - \langle x x' \rangle^2} \tag{2.26}$$

The emittance definitions given by Eq. (2.20) and Eq. (2.26) are also termed *geometric emittance*. In the presence of beam acceleration, the increase of longitudinal beam momentum p_z leads to the decrease of beam divergence $x' = p_x/p_z$. In such a circumstance, (x, x') are no longer conjugate variables, and the geometric emittance undergoes an adiabatic damping [39]. The horizontal *normalized emittance*, $\varepsilon_{n,x}$, is introduced as

$$\varepsilon_{n,x} = \beta\gamma\varepsilon_x, \tag{2.27}$$

where β and γ are the Lorentz factors. The horizontal *normalized rms emittance* is thus

$$\varepsilon_{nx,\mathrm{rms}} = \beta\gamma\varepsilon_{x,\mathrm{rms}}. \tag{2.28}$$

With the paraxial approximation that $p_{\mathrm{total}} = \sqrt{{p_x}^2 + {p_y}^2 + {p_z}^2} \approx p_z$,

$$\begin{aligned} \varepsilon_{nx,\mathrm{rms}} &= \frac{\beta\gamma}{p_{\mathrm{total}}} \sqrt{\langle x^2 \rangle \langle {p_x}^2 \rangle - \langle x p_x \rangle^2} \\ &= \frac{\sqrt{\langle x^2 \rangle \langle {p_x}^2 \rangle - \langle x p_x \rangle^2}}{m_0 c}, \end{aligned} \tag{2.29}$$

where m_0 is the electron rest mass and c is the speed of light. The normalized emittance is an invariant even in the presence of acceleration.

In the scenario of an electron source, e.g., a photocathode, with the assumption that there is no correlation between the transverse position and the momentum of the photoelectrons, i. e., $\langle x p_x \rangle^2 = 0$, Eq. (2.29) becomes

$$\varepsilon_{nx,\mathrm{rms}} = \frac{\sqrt{\langle x^2 \rangle \langle {p_x}^2 \rangle}}{m_0 c}. \tag{2.30}$$

In a more specific case, the normalized emittance can be represented as

$$\varepsilon_{nx,\mathrm{rms}} = \sigma_x \sqrt{\frac{h\nu - \phi_{\mathrm{eff}}}{3 m_0 c^2}}, \tag{2.31}$$

where $h\nu$ denotes the photon energy and ϕ_{eff} the effective work function of the photocathode material. Eq. (2.31) provides an intuitive estimation of the normalized emittance of a photoelectron beam that one would expect from the photocathode material and laser properties. However, it is limited to the photoelectric emission. For great details, we refer the reader to [40, 41].

As an important figure-of-merit parameter for beam quality, beam emittance measures the transverse phase-space area that a charged particle beam occupies,

which indicates how tightly the beam can be focused. A high-quality electron beam requires a low emittance, meaning narrow spread in particle positions and momenta. In this dissertation, Eq. (2.30) will be used to calculate the normalized emittance of the photocathode, with x and p_x directly measured by the velocity-map-imaging spectrometer.

The peak current, I_{peak}, is defined as

$$I_{\text{peak}} = \frac{q_{\text{bunch}}}{\tau_{\text{FWHM}}}, \tag{2.32}$$

where q_{bunch} denotes the beam charge, and τ_{FWHM} the full-width-at-half-maximum (FWHM) bunch length [41]. The beam brightness, $\mathcal{B}$, combines the peak current and beam emittance into a single parameter characterizing the electron current density over the phase space. The normalized beam brightness is defined as [38]

$$\mathcal{B}_n = \frac{2I_{\text{peak}}}{\pi^2 \varepsilon_{nx,\text{rms}} \varepsilon_{ny,\text{rms}}}. \tag{2.33}$$

High brightness, in addition to the low emittance, is critical for the electron-beam-based scientific instruments required very short electron pulses delivering from the photocathodes. For instance, application of electron beam with higher brightness for a high-gain XFEL results in higher efficiency of electron-to-photon energy conversion and shorter undulator length to achieve saturation [42]. On another hand, realization of UEM with high spatial-temporal resolution requires significant improvement in the state-of-the-art performance of electron beam current and emittance, which is essentially a demand on high-brightness electron beams.

2.2.3 Space charge effects

During the generation and transport of a charged particle beam, there are many mechanisms affecting the beam emittance, among which the space charge effect plays an important role.

The space charge effects originates from the interaction between the beam particles and the electromagnetic fields generated from the beam charge and current. The overall repulsive nature of these electromagnetic forces cause expansions of the beam in all dimensions, which leads to degradation of the beam emittance. Consider a cylindrically shaped beam with radius a and uniform charge distribution moving in the z-direction as shown in Fig. 2.8.

Figure 2.8: A cylindrical beam with uniform charge distribution.

According to the symmetry, the electric field is in the radial direction, while the magnetic field is along the azimuthal direction. Application of Gauss' law gives the radial electric field E_r as

$$E_r = \begin{cases} \frac{Ne}{2\pi\epsilon_0 a^2 L} r & \text{for } r < a, \\ \frac{Ne}{2\pi\epsilon_0 L} \frac{1}{r} & \text{for } r > a. \end{cases} \tag{2.34}$$

Similarly, according to Ampére's law, the azimuthal magnetic field B_θ is given by

$$B_\theta = \begin{cases} \frac{\mu_0 v N e}{2\pi a^2 L} r & \text{for } r < a, \\ \frac{\mu_0 v N e}{2\pi L} \frac{1}{r} & \text{for } r > a. \end{cases} \tag{2.35}$$

As a result, the Lorentz force experienced by a particle in the beam due to the space charge fields is

$$\begin{aligned} \vec{F} = & \quad e\vec{E} + e\vec{v} \times \vec{B} \\ = & \quad eE_r\hat{r} + ev\hat{z} \times B_\theta\hat{\theta} \\ = & \quad \frac{Ne^2}{2\pi\epsilon_0 a^2 L} r\hat{r} - \frac{\mu_0 v^2 N e^2}{2\pi a^2 L} r\hat{r} \\ = & \quad \frac{Ne^2}{2\pi\epsilon_0 a^2 L} r\hat{r} \left(1 - \frac{v^2}{c^2}\right). \end{aligned} \tag{2.36}$$

As shown in the equation, the electric and magnetic components of the Lorentz force tend to cancel each other, resulting in an overall repulsive force. The space charge effect will perturb the motion of charged particles in a beam. The impact of space charge effect becomes significant in the case of a high-intensity low-energy beam, i. e., $v \ll c$. Although space charge effect significantly affects the electron beam properties, in this thesis work, it is excluded since the average number of electrons emitted per pulse, in the experiments described later, is on the order of one or less.

2.2.4 Transverse coherence length

For an electron beam, whose emittance is hardly to be accurately characterized under the technologies nowadays, the transverse coherence length of the electron beam provides another way to determine the beam quality, compassing emittance, through the diffraction experiments. In a diffraction experiment, the ability of an electron beam to resolve large and complex structures depends crucially on the transverse coherence of the electron beam [43]. In order for constructive electron interference to occur, besides satisfying the Bragg condition, the electron beam has to be coherent. More precisely, the transverse coherence length L_x has to be larger than the unit-cell size of the sample. For an electron beam, the transverse

coherence length can be defined analog to laser optics, using a criterion of 88% for the visibility of interference. This definition is related to approaches based on the van Cittert-Zernike theorem under the assumption of an incoherent source [44]. The transverse coherence length L_x of an electron beam at the beam waist is given by

$$L_x = \frac{\lambda}{2\pi \cdot \sigma_{x'}}. \tag{2.37}$$

Using the de Broglie relation $\lambda = \frac{2\pi\hbar}{\sigma_{p_z}}$ and considering $\sigma_{x'} = \frac{\sigma_{p_x}}{\sigma_{p_z}}$, a more simplified relation is found for the beam coherence along the x coordinate

$$L_x = \frac{\hbar}{\sigma_{p_x}}. \tag{2.38}$$

The coherence length can also be expressed as a function of the beam emittance

$$L_x = \frac{\hbar \cdot \sigma_{x,\mathrm{rms}}}{m_0 \cdot c \cdot \varepsilon_{nx,\mathrm{rms}}}, \tag{2.39}$$

where $\sigma_{x,\mathrm{rms}}$ is the rms beam size, m_0 is the electron rest mass, c is the speed of light and $\varepsilon_{nx,\mathrm{rms}}$ is the normalized rms emittance. As is shown by Eq. (2.39), given a desired rms beam size $\sigma_{x,\mathrm{rms}}$, the lower the rms emittance, the longer the coherence length.

2.2.5 State-of-the-art emittance measurement

Since beam emittance is a key parameter for beam quality characterization, various experimental techniques for high-precision emittance measurement have been developed over the past decades. To understanding the work principles of the existing instrument is very important not only helps improve the our setup but also understanding nowadays experiments performed. Therefore, in this section, several state-of-the-art emittance measurements, e. g., the energy analyzer, waist scan, slit scan, free expansion are presented with some described in detail from a theoretical point of view.

Energy Analyzer

The transverse energy spread can be inferred using hemispherical analyzers as well as time-of-flight based (TOF) detectors in Angle Resolved Photoemission Spectroscopy (ARPES) experiments [45]. Such analyzers can map energy and angular distribution of emitted electrons via rotating the sample stage, from which it is possible to infer the mean transverse energy. However, due to the sensitivity of low energy electrons to stray magnetic fields and work function variations, the

analyzer is limited to the studies of the emission processes for higher (>1 eV) energy electrons.

Other techniques, such as the 2D energy analyzer [46], have been reported to measure the longitudinal and transverse energy distributions based on the principle of adiabatic invariance and the motion of low energy electrons in a strong magnetic field. The important property here is the conservation of energy of an electron in a magnetic field, indicating $W_\perp + W_\parallel - V = C$, where C is a constant, V the electrostatic potential, $W_\perp$ and $W_\parallel$ the transverse and longitudinal energies, respectively. Owing to the adiabatic invariance, the transverse energy $W_\perp$ changes only with the magnetic field strength. Therefore, the change in the potential V causes only the longitudinal energy $W_\parallel$ to change. While changing the magnetic field strength causes both the transverse energy and the longitudinal energy to change in order to satisfy the adiabatic invariance and the energy conservation. Consequently, the transverse energy can be inferred by measuring the longitudinal energy via varying electronic potential and magnetic field strength, before and after coupling with the transverse energy. However, this technique does not allow measurement under high electric fields. Thus, it cannot reproduce the conditions in an actual photoinjector and measure the dependence of mean transverse energy on the electric field.

Waist scan technique

The waist scan method [47, 48], is one of the simplest and most common ways to measure beam emittance. In such a measurement, the transverse beam size of a charged particle beam is focused by an electromagnetic lens, e. g., a solenoid or quadrupole magnet, and is measured at a downstream location. The inverse focal length of a solenoid magnet, $1/f_{\mathrm{sol}}$, is given by

$$\frac{1}{f_{\mathrm{sol}}} = \frac{e^2}{4 \cdot {p_z}^2} \cdot \int_{-\infty}^{\infty} B_{\mathrm{sol}}(z)^2 dz, \tag{2.40}$$

where $B_{\mathrm{sol}}(z)$ is the longitudinal magnetic field of a solenoid. On the other hand, the inverse focal length of a quadrupole magnet, $1/f_{\mathrm{quad}}$ is given by

$$\frac{1}{f_{\mathrm{quad}}} = \frac{e g_{\mathrm{quad}} \cdot L_{\mathrm{quad}}}{p_z}, \tag{2.41}$$

where g_{quad} is the magnetic field gradient and L_{quad} is the effective length of the quadrupole. With a given focal length, the minimum beam size is called a *beam waist*. For both magnets, varying the current to the magnet effectively changes the focal length, as well as the longitudinal position of the beam waist. With an appropriate experimental setup, a series of beam sizes including the beam waist are measured as a function of the foal length. The measurement results essentially

contain information of beam size, beam divergence, and their correlation, from which the beam emittance can be estimated.

Consider a beam line consisting of an electromagnetic lens with a focal length f and a drift space with a length L, the trace space coordinates of a particle are given by

$$\begin{pmatrix} x_1 \\ x_1' \end{pmatrix} = M \begin{pmatrix} x_0 \\ x_0', \end{pmatrix} \tag{2.42}$$

where the subscripts 0 and 1 denote longitudinal position at the entrance and exit of the beam line, respectively, while the transfer matrix M is given by

$$\begin{aligned} M = \quad & M_{\text{drift}} M_{\text{thin-lens}} \\ = \quad & \begin{pmatrix} 1 & L \\ 0 & 1 \end{pmatrix} \begin{pmatrix} 1 & 0 \\ -1/f & 1 \end{pmatrix} = \begin{pmatrix} 1 - L/f & L \\ -1/f & 1 \end{pmatrix}. \end{aligned} \tag{2.43}$$

With Eq. (2.42) and Eq. (2.43), the square of the rms beam size $\sigma_{x,1}^2$ is obtained as

$$\sigma_{x,1}^2 = \frac{a}{f^2} + \frac{b}{f} + c, \tag{2.44}$$

where $a = L^2\sigma_{x,0}^2$, $b = 2(L\sigma_{x,0}^2 + L^2\sigma_{xx'})$, and $c = L^2\sigma_{x',0}^2 + 2L\sigma_{xx',0} + \sigma_{x,0}^2$. Finally, the normalized emittance is calculated as

$$\varepsilon_{nx,0} = \beta\gamma\sqrt{\sigma_{x,0}^2\sigma_{x',0}^2 - \sigma_{xx',0}^2} = \beta\gamma\frac{\sqrt{4ac - b^2}}{2L^2}. \tag{2.45}$$

where β and γ are the Lorentz factors, and the coefficients a, b and c are obtained from fitting of the measured beam size versus inverse focal length.

Slit scan technique

Another popular way to measure the emittance in photoinjector is called slit scan. A schematic set up of the slit scan technique for vertical beam emittance estimation is shown in Fig. 2.9. An incident beam traverses a slit plate with the slits vertically spaced by equal distance and the slit widths much smaller than the beam size. Beamlet are formed after the slit plate, and their transverse profiles are captured on a downstream detector. From the slit position, beamlet intensity and size on the detector, the vertical emittance of a beamlet can be extracted. The vertical emittance of the full beam is estimated from those of the beamlets. Similarly, the horizontal beam emittance can be measured using a plate with horizontally spaced slits.

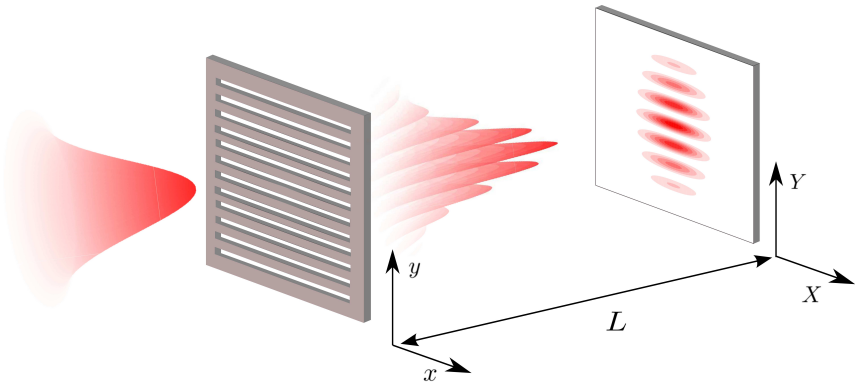

Figure 2.9: Schematic of the slit scan method for beam emittance estimation.

Considering a plate contains a number of p slits, the vertical trace space coordinates of a particle from the beamlet after the j-th slit is defined as (y_j, y'_j) with $j = 1, ..., p$. After a drift space with length L, the beamlet arrives at the detector, with the trace space coordinates (Y_j, Y'_j) given by

$$\begin{pmatrix} Y_j \\ Y'_j \end{pmatrix} = \begin{pmatrix} 1 & L \\ 0 & 1 \end{pmatrix} \begin{pmatrix} y_j \\ y'_j \end{pmatrix}. \tag{2.46}$$

Therefore, the divergence at the j-th slit position is given by $y'_j = (Y_j - y_j)/L$. Denote the number of particles in the j-th beamlet as n_j, the intensity of the j-th beamlet on the detector as I_j. With the total number N of beam particle before the slit, the first moments of the beam are estimated as

$$\begin{aligned} \langle y \rangle = & \quad \frac{1}{N} \sum_{i=1}^{N} y_i \\ \approx & \quad \frac{1}{N} \Big(\sum_{i=1}^{n_1} y_{1i} + \sum_{i=1}^{n_2} y_{2i} + \cdots + \sum_{i=1}^{n_p} y_{pi} \Big) \\ \approx & \quad \frac{\sum_{i=1}^{p} I_i y_i}{\sum_{i=1}^{p} I_i}, \end{aligned} \tag{2.47}$$

where y_{ij} stands for the position of the i-th particle passing through the j-th slit. Estimations for $\langle y' \rangle$, $\langle y^2 \rangle$, $\langle y'^2 \rangle$, and $\langle y y' \rangle$ can be derived in a similar manner [49]. Finally, the rms emittance is obtained according to Eq. 2.26 as $\varepsilon_{ny,rms} = \sqrt{\langle y^2 \rangle \langle y'^2 \rangle - \langle y y' \rangle^2}$.

Free expansion

Free expansion [50] is the technique most closely related to the VMI spectroscopy demonstrated later in chapter 3. Electrons photoemitted from a cathode are accelerated by a cathode-anode voltage, V, over a small gap, g, to a grid anode.

Electrons pass through the grid and then drift over several hundred millimeters to a detector. The layout of the measuring system is shown in Fig. 2.10. Electrons in the cathode-anode move on parabolic trajectories and arrive at the grid with a lateral position x and angle θ. The time of flight, t, of the electrons move along the axis of the instrument over the cathode-anode gap is given by

$$t = \frac{g\sqrt{2m}}{eV}(\sqrt{\varepsilon_z + eV} - \sqrt{\varepsilon_z}) \tag{2.48}$$

where ε_z is the initial electron kinetic energy in the longitudinal z direction. With a gap voltage applied, typically of the order of kV and much larger than the electron energies interested <1 eV for low emittance, the Eq. (2.48) can be simplified to $t = g\sqrt{\frac{2m}{eV}}$.

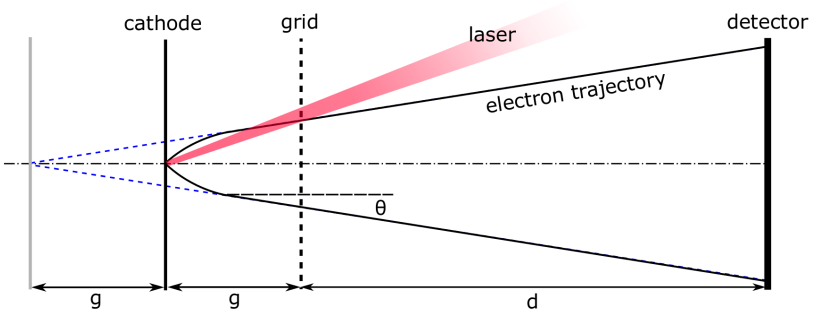

Figure 2.10: Schematic of free expansion system. Electrons emitted at the cathode plane are accelerated through a grid plane into a drift region. The intensity distribution of the beam is recorded on the detector.

Since it is desirable to have no transverse electric field, the transverse velocity is a constant of motion. As a result, the measured transverse position at the grid, x, is simply given by the product of the transit time and the transverse velocity and can further be translated into the transverse momentum as

$$p_x = \frac{x}{g}\sqrt{\frac{emV}{2}} \tag{2.49}$$

and the angular deviation at the grid given by

$$\theta = \frac{p_x}{p_z} = \sqrt{\frac{\varepsilon_x}{eV}} \tag{2.50}$$

where ε_x is the transverse energy which remains unchanged between the cathode and the grid. With a detector placed with a distance d to the grid, the transverse displacement L at the detector plane is given by

$$L = (2g + d)\sqrt{\frac{\varepsilon_x}{eV}} \tag{2.51}$$

and the transverse momentum is given by

$$\frac{p_x}{mc} = \frac{L}{2g+d}\sqrt{\frac{2eV}{mc^2}} \tag{2.52}$$

By adjusting the acceleration voltage, it is able to measure transverse energy and momentum to high precision over all the relevant low energy scale. This technique is conceptually the analog to the early ion imaging experiments before the invention of the velocity-map-imaging spectrometer [51]. Since the application of grid electrodes leads to transmission reduction, severe trajectory deflections and blurring due to the non-point source geometry. These problems are avoided with open lens electrodes. The very details of the VMI spectrometer can be found in the next chapter as well as a comparison to the existent techniques in §3.6.

Chapter 3

Experimental Apparatus

In order to study the photoemission process of solid-state materials, the first task of this thesis was the building of a velocity-map-imaging spectrometer. The concept "velocity map imaging" was first introduced by Eppink and Parker in 1997 [51]. Exploiting the focusing properties of electrostatic lenses, it has been demonstrated giving substantial improvement of the two-dimensional (2D) ion/electron imaging technique. Over the last decade, the velocity map imaging technique has been widely used in the field of atomic and molecular physics as well as physical chemistry, for studying photoelectron spectroscopy, ultrafast pump-probe spectroscopy, and chemical reaction dynamics [52]. The VMI spectrometer demonstrated in this dissertation aims to characterize the electron emittance of photocathodes, via characterizing the average spread of electron coordinates in position-and-momentum phase space. The spectrometer configured in the laboratory is described in §3.1. To perform the ultrafast photoemission experiments, an ultrashort-pulse laser system, described in §3.2, was used to generate the intense electric fields acting on various photocathodes. Both commercial softwares, SIMION and COMSOL, were employed to predict the spectrometer performance and presented in §3.3. §3.4 discusses a detailed calibration of the spectrometer, as a proof-of-principle experiment, employing a planar metal surface. Further more, the transverse energy resolution and systematic errors of the current spectrometer are discussed in §3.5. Finally, a comparison of the VMI spectrometer with other techniques/apparatuses discussed in §2.2.5 is provided in §3.6.

3.1 Velocity-map-imaging spectrometer

The velocity-mapping technique maps the particles of the same transverse velocity (in this thesis, the term *velocity* refers to the vector quantity whereas *speed* denotes the scalar) onto the same point on a 2D detector, to first order, irrespective of their initial spatial coordinates. To achieve this, a configuration of electrostatic lenses is

employed to spatially tailor the electric fields [51, 53]. The simplest case utilizes three parallel open electrodes, named repeller (R), extractor (E) and ground (G), forming the desired extracting electric field. As mentioned by Eppink and Parker already, the electrostatic lenses are capable to image and magnify the spatial coordinates suppressing the effect of velocity components as well. Analogous to the VMI, it is referred to as spatial-map imaging (SMI). A schematic graph of the principle on the operation of both SMI and VMI modes of the spectrometer is shown in Fig. 3.1. The particles following the red and blue trajectories have the same initial transverse momentum, respectively. Three starting positions (one for each transverse velocity) have been simulated. With the potential of the repeller and ground electrodes fixed, via varying the potential of the extractor, the particles fall on the detector according either to the initial spatial coordinates (SMI mode in Fig. 3.1(a)) or initial momentum coordinates (VMI mode in Fig. 3.1(b)).

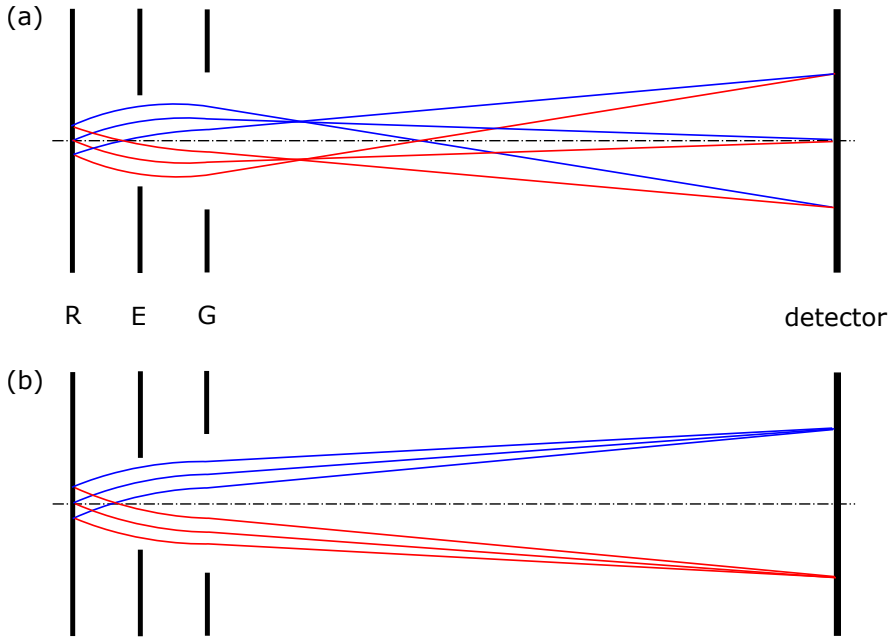

Figure 3.1: Particle trajectories when spectrometer is operated in the (a) spatial map imaging (SMI) mode; (b) velocity map imaging (VMI) mode. R: repeller, E: extractor, G: ground.

Fig. 3.2 shows the CAD drawing of the VMI spectrometer designed for this thesis study. The spectrometer contains two substantive vacuum chambers, the load-lock and the main chamber, connected by a CF40 valve. The sample is mounted on the top of the sample holder (colored bright red), which can be retracted into the load-lock chamber. This permits to exchange the sample without breaking the ultra-high vacuum (UHV) of the whole imaging system. The main chamber is kept a magnitude better of the vacuum than the load lock. When performing the imaging experiments, the sample holder is transferred into the main chamber using the

Figure 3.2: An overview model of the velocity-map-imaging (VMI) setup showing the components including: chambers, manipulator, pumps, gauges and the drift tube.

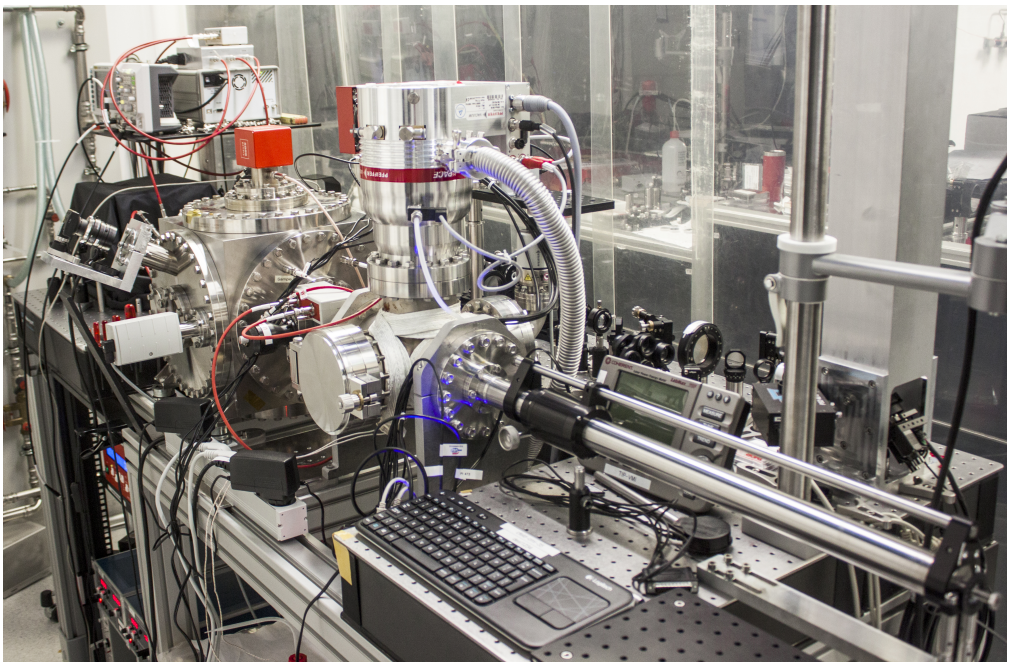

Figure 3.3: A photograph of the VMI spectrometer configured in the laboratory.

manipulator and brought in contact with the repeller plate to make sure they are at the same electric potential. The main chamber contains a stack of three cylindrically symmetric plates, arranged in parallel, separated by 15 mm, and with applied potentials serve as the electrostatic lens. This is followed by a $\sim$0.5 m drift tube, which ends with a detector assembly consisting of a double micro-channel plate (MCP) and a phosphor screen for imaging the electron distributions. The images are recorded by a CMOS camera and the data acquisition system is programmed using LabVIEW. The full configuration is shielded against stray fields by a µ-metal tube (colored purple in Fig. 3.2). A photo of the spectrometer which has been constructed in the laboratory is displayed in Fig. 3.3.

3.1.1 Vacuum system

It is important that the systems used to study the light-matter interaction dynamics are kept in ultra-high vacuum. In order to accurately determine the spatial or velocity distribution of the particles, they must be nascent, i. e., they must not undergo a collision with another species as this alter their travel trajectories to the detector.

A combination of a turbo pump (Pfeiffer HiPace 300 M) backed up by a turbo pumping station (Pfeiffer HiCube 80 Eco) was used to approach the incipient high vacuum of the chambers. The turbo pumping station, incorporating a turbo pump (Pfeiffer HiPace 80) and a matched backing diaphragm pump (Pfeiffer MVP 015-2), pre-pumps the system to reach a fore-line pressure in the magnitude of mbar. The

HiPace 300 M, a magnetically levitated (minimizing vibrations) turbo pump with pumping speed of 300 l/s, is attached to the top of the load-lock chamber (see Fig. 3.2) and evacuates the whole system to the pressure of 10^{-9} mbar. In addition, an ion getter pump (IGP, SAES NEXTorr D500-5) was mounted on the top of the main chamber. When the vacuum reaches 10^{-9} mbar, switching on the IGP further decreases the pressure as low as to 10^{-10} mbar. The reason for choosing an IGP is to avoid vibrations, usually worse with the turbo pumps, to the main chamber where the experiments are performed. The IGP is kept operating to maintain the high vacuum when both the pre-pump and load-lock are vented for exchanging the samples. For the first evacuating the chamber or after long time exposure to air, the system was essentially baked with temperature ∼150 °C for a few days to reach the UHV. The instant vacuum conditions of the system were monitored by three pressure gauges located at different positions. The ones used for both the load-lock (Gauge 02 in Fig. 3.2) and pre-pump (now shown) are Pfeiffer Compact FullRange™ Gauge PKR 251 with the measurement range from 5×10^{-9} to 1000 mbar. The main chamber is monitored by a Pfeiffer Compact FullRange™ BA Gauge PBR 260 (Gauge 01 in Fig. 3.2), which is able to detect the pressure down to 5×10^{-10} mbar.

3.1.2 Detection system

Micro channel plates (MCPs), that intensify single particles or photons by the multiplication of electrons via secondary emission, have been widely used for the detection of charged particles [54]. The micro-channels are typically approximately 10 µm in diameter, parallel to each other, hexagonally packed to form a plate and often enter the plate at a small angle to the surface (∼8 ° from normal). The position sensitive detection in our experiments was implemented by a chevron configured MCP (Beam Imaging Solution, BOS-40-OPT01-MS). In a chevron MCP, two micro-channel plates with angled channels rotated 90 ° from each other are either pressed together or have a small gap between them to spread the charge across multiple channels. The electrons that exit the first plate start the cascade in the next plate, showing the advantage of significantly larger gain (10^7 for our case) at a given voltage over the straight channel MCP. A phosphor screen is conventionally attached to the MCP exhibiting the phenomenon of luminescence induced by particle collisions. The phosphor powder P46 with a decay time of 300 ns was chosen and ideal for particle detection experiments operating in a repetition rate of 1 kHz in this thesis work.

The luminescence images were recorded by a CMOS camera (Optronis CL600×2) with a frame rate of 1 kHz and a resolution of 480×480 active pixels. Both the MCP and the CMOS camera were trigged by the electric signal from the laser system through a pulse/delay generator (BNC model 575 Pulse/Delay Generator). The BNC generator input trigged by the laser is referenced as T_0. During the

experiments, the MCP back (adjacent to the phosphor screen) was applied with 1500-2000 V using a high voltage supply (iseg NHQ 204M), while the MCP front grounded and the MCP middle left floating. The phosphor screen was applied with 4500-5000 V by iseg NHQ 108L. A gating system, a combination of a high voltage switch (Behlke, HTS 31-03-GSM) and a home-made voltage divider, is connected between the MCP back and high voltage supplies. The voltage divider outputs two voltages, V_{low} and V_{high}, with one voltage input V_{input}, as $V_{\text{low}} = x \cdot V_{\text{high}}$ with $0 < x < 1$. The Behlke switch rests at V_{low}, which is below the threshold for detection, as a default. When triggered by a TTL pulse from the BNC box, it switches to V_{high} for as long as the trigger pulse (>100 ns) dictates. The raising time of the voltage from V_{low} to V_{high} is determined by the switch properties. In our experiments, the $V_{\text{high}} = V_{\text{input}}$ and $x = 0.5$, the Behlke switch enables fast switching between the voltages with a rise/fall time of 14 ns and the minimum pulse duration of 100 ns.

3.1.3 Acquisition system

The acquisition system is programmed in LabVIEW. The particles hitting on the MCP detector are recorded in LabVIEW using a "centroiding" algorithm. Fig. 3.4 shows three typical cases for the fluorescence images caused by the electron collision on the MCP. The fluorescence images usually occupy several grids, according to the MCP voltage applied. When MCP voltage is relatively low, the number of the grids occupied by the fluorescence image of one electron increases with increasing MCP voltage until the detector gets saturated, i. e., the number of the grids stays the same with increasing the MCP voltage. At the point it starts saturation, it records electrons with the highest efficiency and in a safe operating voltage range. In Fig. 3.4(a), with one single electron, the "centroiding" algorithm recognizes the electron position by fitting images to a 2D Gaussian distribution to calculate the centroid of the images using a C++ program, and writes all centroids into the LabVIEW output file. By synchronizing the laser system and CMOS camera, the electron count is related to each exciting laser shot. Fig. 3.4(b) shows a case of two electrons coinciding on a close position but can still be resolved with the real count by the current centroiding algorithm. In Fig. 3.4(c), multiple electrons appear on the detector which are too close to be resolved as individual ones. Consequently, they are recognized as one electron. Therefore, the electron density can not be correctly reflected and calculated from the certain detection area where photoemitted electrons overlaying on the MCP. This normally happens when there are more than hundred electrons incident on the detector at once, yielding a double blob (DBL) ratio of ∼10%. This will influence the quantum efficiency determination in the experiments (e. g., in §5.3) under the strong-field regime which usually accompanied with more electrons photoemitted.

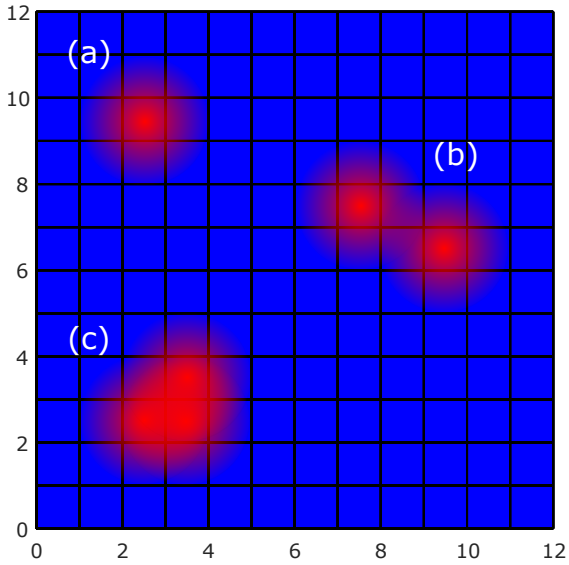

Figure 3.4: A graph of (a) single electron; (b) two close electrons; and (c) multiple close electrons incident on the MCP detector. The grid represents the camera resolution.

3.2 Laser system

Ultrashort laser pulses were used to illuminate the sample at a glancing incidence angle. Pulses at the separate central wavelengths (800 nm, 1300 nm, and 266 nm) can be used for the photoemission experiments. The beam paths for the three wavelengths are shown in Fig. 3.5. wavelength. The beam is stabilized upstream using the position-sensitive beam stabilizer (TEM PSD 4D) in order to compensate/minimize the laser position drift on the sample. A photo, Fig. 3.6, is attached showing the beam line built up in the laboratory.

According to Fig. 3.5, both the middle (800 nm) and bottom (400/266 nm) beam paths are directly derived from a 800-nm 35-fs Ti:sapphire laser amplifier (Coherent Elite Duo) with a 3-kHz repetition rate. A half-wave plate (HWP) combined with a thin film polarizer (TFP), which reflects >99.8% s-polarized beam, are used to vary the laser pulse energy. The transmitted beam, i. e., the fundamental 800 nm, is sent through a refracting telescope using two lenses to magnify the beam size by $M = f_2/f_1$, which enables the small focus spot size with a certain focus length. A pinhole was placed in the minimum position of the laser waist between the two lenses to spatially filter the mode of the laser beam. The enlarged beam was then focused onto the sample surface by a 500 mm focus lens through the input window of the vacuum chamber. The focus lens was mounted on a 3D motorized stage to precisely control the laser focus position on the sample with micrometer accuracy. The other HWP, mounted on a motorized rotation stage, was placed in front of the chamber window for varying the polarization, which is interesting for the laser-matter interactions during the electrostatic imaging experiments. All

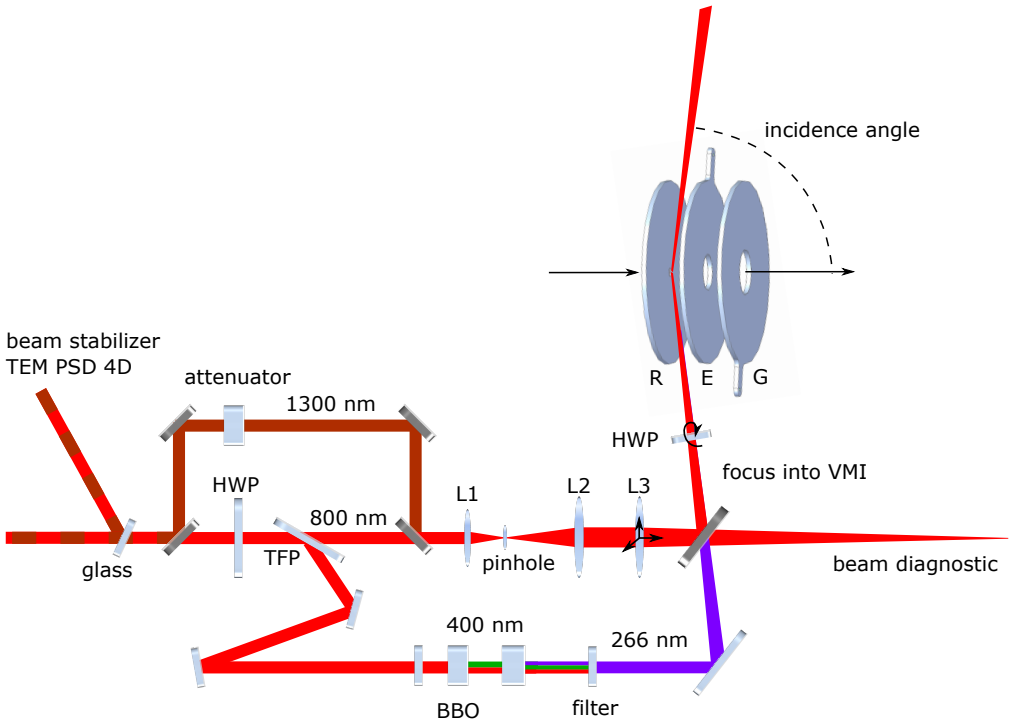

Figure 3.5: The three paths of the laser beam built up as labeled with different central wavelength, top: 1.3 µm; middle: 800 nm; bottom: 400 nm or 266 nm. The dark colored optics were mounted on magnetic retention bases in order to be inserted or removed from the optical path with a high degree of repeatability.

the motorized stages were implemented into the acquisition system programmed using LabVIEW to automatically record the experimental data. The beam profile was measured using Spiricon SP620U, showing a focal spot size of ∼30 µm full-width-half-maximum (FWHM). After propagating a distance and traveling through dispersive materials, the pulse duration grows and was measured to be 45 fs by frequency-resolved optical gating (FROG). The beam reflected by the TFP was sent through a Beta Barium Borate (BBO, 29.2 °, type I) crystal to generate the second-harmonic (SHG) at 400 nm by frequency doubling of the fundamental 800 nm pulses. In addition, via sum-frequency generation of the fundamental and second harmonic, the third-harmonic (THG) at 266 nm can be produced for the experiments as an alternative source.

In order to explore the photoemission process driven with a longer wavelength, a separate beam line at 1.3 µm was built up. The 1.3 µm pulses, exhibiting a pulse duration of about 100 fs, were generated by a custom-made optical parametric amplifier (OPA) [55]. In the OPA, a few µJ portion of a 800 nm 150 fs pulse generated by another Ti:sapphire amplifier (Cryo PA, from Coherent) is spectrally broadened by focusing it into a few mm long transparent crystal (YAG) so that it extends into the IR region. Such process is called supercontinuum generation

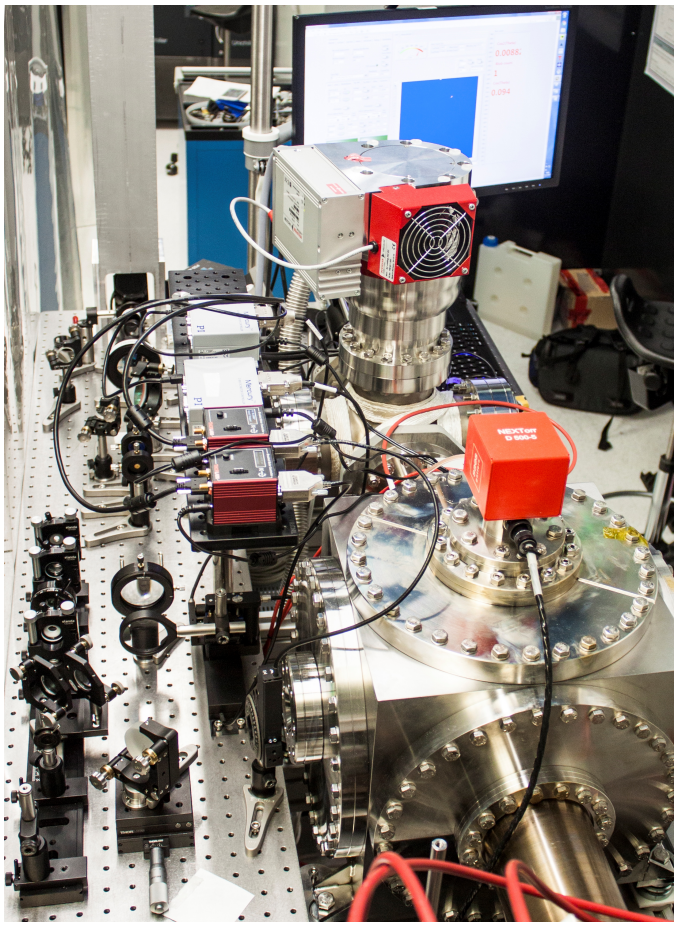

Figure 3.6: A photograph of laser beam path built up in the laboratory. The beam enters the setup from the periscope (seen at the back) connecting the VMI breadboard to the laser table.

or white light generation [56], and allows to generate a weak spectrum that is spanning over more than 2 octaves and it is phase-locked to the driving laser pulse. A narrow band portion of the broadened spectrum centered around 1300 nm it is then amplified by a 500 µJ portion of the 800 nm pulse in two consecutive BBO crystals (28 °, Type II, thicknesses of 2 and 3 mm). Such process is known as optical parametric amplification [57] and allows, under certain conditions, to transfer energy from a strong pulse (named pump) to a weaker and longer wavelength pulse called signal. In the process due to energy conservation, a third beam, named idler, is generated. Due to the collinear geometry, a dichroic mirror is employed to separate the signal beam (at 1.3 µm) from the pump (800 nm) and the idler (2.08 µm). The final energy in the signal beam is about 70 µJ. The signal beam is then collimated and transported to the VMI spectrometer. The same pointing stabilizer used for the Ti:sapphire pulses is used to stabilize the 1.3 µm beam, leading to a very similar level of pointing stability.

3.3 Simulation of the spectrometer

The simulations for evaluating and predicting the VMI spectrometer performance were carried out using either SIMION® [58] or COMSOL® [59] software, which have their own advantages and drawbacks.

3.3.1 SIMION

SIMION® allows one to adjust parameters during the simulation and to immediately visualize the resultant fields and particle trajectories, after importing the configuration of electrodes of defined voltages. SIMION was mostly utilized, in this dissertation, for simulating the operating parameters of the spectrometer due to it fast run speed. In SIMION, two group of particles, i. e., same position but different velocities and same velocity but different positions, were categorized for determining the SMI and VMI prerequisites, according to the principle schematic in Fig. 3.1.

As will be discussed in §3.4, the calibration of the VMI spectrometer, the simulations from the planar metal surface were carried out using SIMION and match very well with the experimental results, which makes the prediction of the spectrometer performance very reliable, therefore qualified to guide the experiments. However, SIMION is limited to the simulation with systems of huge dimension difference, e. g., the electron trajectories in a hundreds-of-millimeter-long drift tube from a nanometer scale tip emitter. Therefore, COMSOL came with more possibilities as well as, however, more complexity and incontrovertibly slower executing speed.

3.3.2 COMSOL

COMSOL Multiphysics® is a general-purpose software platform, based on advanced numerical methods, for modeling and simulating physics-based problems and further expanding the simulation platform with dedicated physics interfaces and tools for electrical, mechanical, fluid flow, and chemical applications [59]. COMSOL has the possibility for modeling the systems with different and large range mesh settings, which is very important for predicting the future experiments on nanotips. Since the presence of the nanotips introduce inevitable field distortion between repeller and extractor, it therefore disturbs the focusing behavior of electrostatic lens of the spectrometer. Therefore, to interpret the imaging and extract the information relies decisively on the reliable simulation. A COMSOL simulation on a tungsten nanotip, for the future experiments, has been simulated and is detailed in Appendix A.

3.4 Calibration of the spectrometer

The electron spectrometer has been characterized experimentally, accompanied by simulations, in order to determine the focusing conditions for the SMI and VMI modes. The experiments performed to characterize the spectrometer as a first proof-of-concept experiment has been achieved from the Au thin film photocathode.

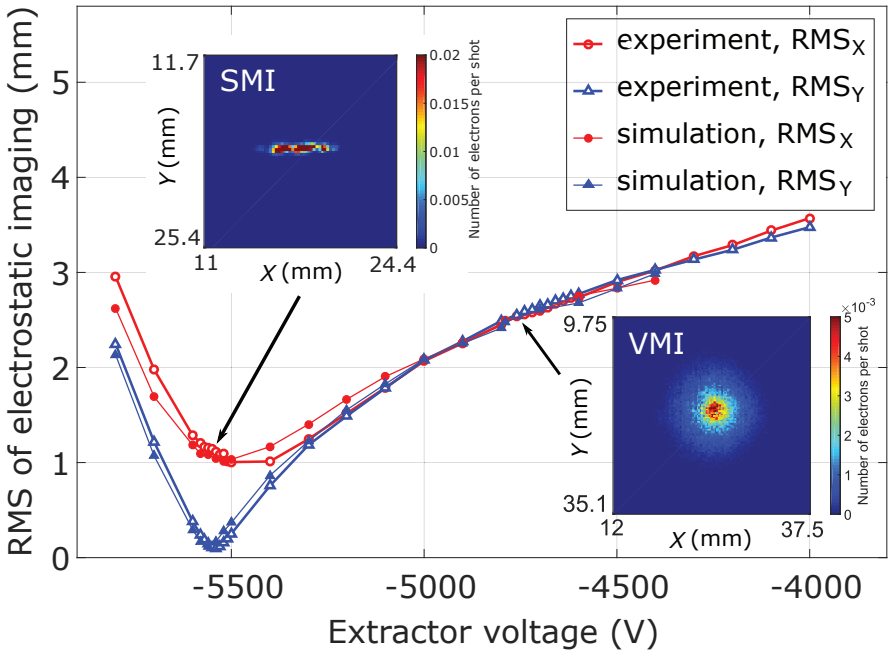

Figure 3.7: Experimental (hollow) and simulated (solid) root-mean-square deviations of electron spatial distributions on the 2D detector versus focusing extractor voltage in both X and Y-directions. The insets show SMI and VMI detector images for the indicated positions.

Fig. 3.7 shows the measured root-mean-square (RMS) in the X- and Y-directions of the spatial electron distribution on the detector as a function of the extractor voltage, together with the results from SIMION simulations. A similar behavior is observed from [60]. The strongest focusing of the electron bunch onto the detector is achieved at an extractor potential of -5560 V, which is thus identified as the SMI voltage. The RMS at this voltage shows the magnified laser-surface-interaction area. The slightly different focusing behavior of the electron bunch in the X and Y-directions is attributed to the asymmetric initial electron bunch size, due to the glancing incidence irradiation, and the finite kinetic energy of the electrons. When increasing the extractor voltage, the electron bunch diverges. Based on our simulations, the extractor voltage for VMI is approximately -4790 V. For a full calibration of the spectrometer, the simulations were used to study the field configuration and the electron trajectories in those fields for the given electrode

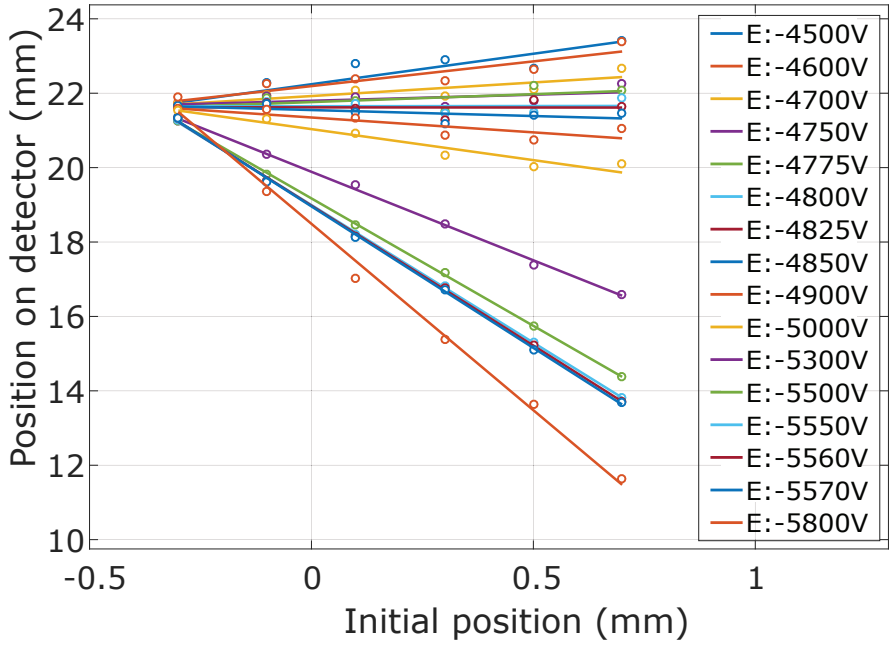

Figure 3.8: Position dependence of COM of the electron distribution on the detector on the initial source position for various extractor potentials from -5800 V to -4500 V.

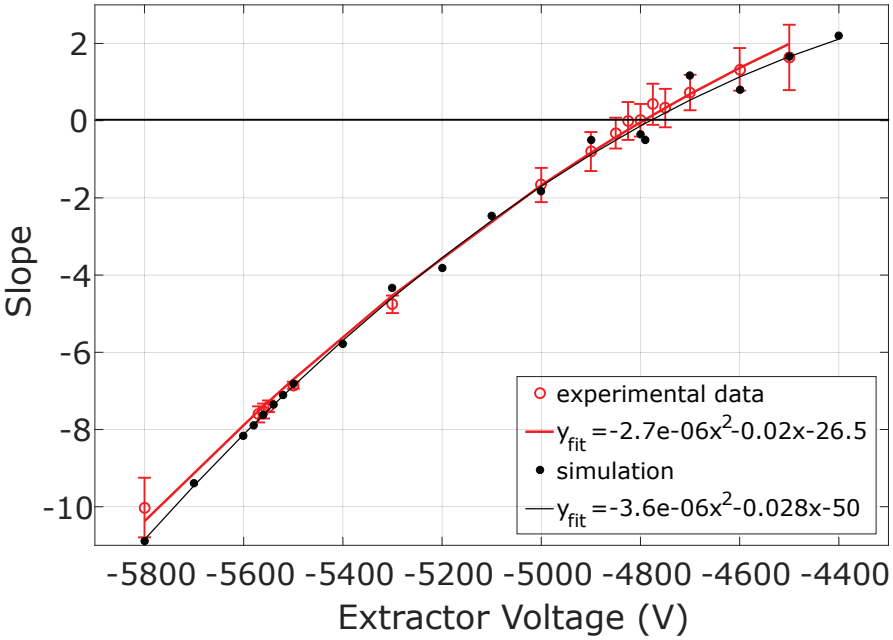

Figure 3.9: Slope of the experimental laser position dependent COM of the spatial distribution at the detector as function of the extractor voltage (red circles) with a quadratic fit (red line). Black points and the black line indicate the corresponding simulated results.

configurations and the particles initial distributions. In Fig. 3.7 the simulated RMS of the electron bunch, with electrostatic imaging, at the detector position is plotted as function of extractor voltage. The simulations were carried out given an initial spatial 2D Gaussian distribution of 2000 electrons for each simulated point. The center of mass (COM) of this distribution was given by $(X, Y) = (0, 0)$ and a Z-coordinate matching the sample surface with standard deviations of $\sigma_X = 140$ µm and $\sigma_Y = 15$ µm. The initial momentum distribution was given by a uniform half sphere with an uniform kinetic energy distribution of electrons in the range of $[0.1, 0.6]$ eV.

The COM of the electron distribution as a function of the initial starting position of the electrons, i. e., the laser focus position on the sample, was used to experimentally calibrate the voltage for velocity-map imaging. Fig. 3.8 shows the COM as function of the laser position for various voltages together with straight-line fits. A decrease of the slope with decreasing extractor voltage is observed. Fig. 3.9 depicts the slope of each measurement in Fig. 3.8 as a function of the extractor voltage together with a quadratic fit and corresponding simulation results. The error bars for the experimental points are given by the first-order coefficient error of each fitting curve with 95% confidence bounds. The VMI mode is obtained at the zero crossing of this curve, i. e., at -4790 V, as for this voltage the distribution, to first order, becomes independent of the starting position. The data shows a good agreement with the simulations, confirming that the extractor voltage for operating the VMI is -4790 V. From the simulations the imaging setup is calibrated regarding the transverse electron velocities to 8014 m/s/pixel on the detector. The resulting voltages for operation in the SMI and VMI modes are listed in Table 3.1.

Table 3.1: Voltages (in V) applied for operation in SMI and VMI mode

	Repeller	Extractor	Ground	Sample
SMI	-6000	-5560	0	-6000
VMI	-6000	-4790	0	-6000

Fig. 3.10 shows experimental and theoretical COM of the electron distribution at the detector as function of the lens position, that is used to focus the laser beam onto the sample for SMI (E:-5560 V). The straight lines are fits to the data. The difference in the slope between the X- and Y-directions is due to the glancing incidence angle θ. The laser spot position on the sample moves $1/\cos\theta$ times farther in X than in Y when displacing the laser beam by the same distance using a translation stage. For the Y-direction we obtain a magnification factor of $\sim$7.5 from the fit. For the X-direction a slope of $\sim$ 72.7 is obtained. This results in a ratio of 9.7 between the two slopes that corresponds to an incident angle of 84 °.

The SIMION simulation results, also shown in Fig. 3.10, are in good agreement with the data.

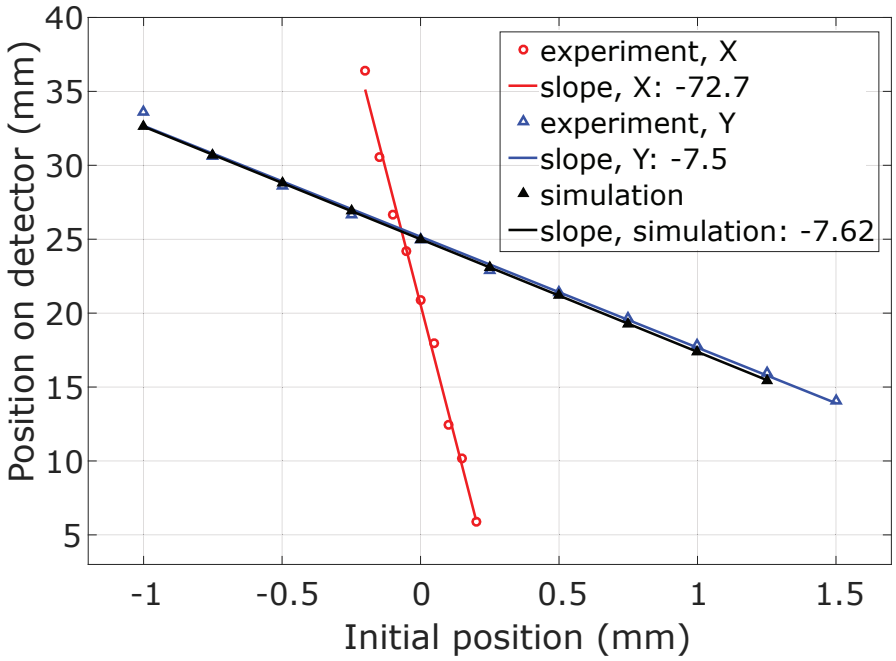

Figure 3.10: The COM of electrostatic imaging on the detector as a function of the initial source position for SMI mode, i. e., an extractor voltage of -5560 V. The slope in Y-direction is the spatial magnification factor. The ratio between X- and Y-directions confirms the incidence angle of the laser beam of 84 °.

The focusing conditions for the SMI and VMI mode depend strongly on the position of the sample inside the velocity-map imaging spectrometer. Fig. 3.11 shows the simulated extractor voltages necessary for SMI and VMI mode for various sample displacements with respect to the front surface of the repeller plate. These simulations show that either the sample position has to be known, or at least be reproduced, to a very high precision or calibration measurements have to be performed when a new sample is inserted into the spectrometer. Fortunately, with the protocol described in this dissertation, this calibration can be done quickly. In addition the dependence of the extractor voltage on the flight distance has been investigated (red points and lines). Our simulations show that this uncertainty is uncritical compared to the exact sample position in the spectrometer.

3.5 Energy resolution and systematic errors

The transverse energy resolution $\mathrm{d}E = mv_{2\mathrm{D}}\,\mathrm{d}v_{2\mathrm{D}}$ is linearly increasing with the transverse velocity $v_{2\mathrm{D}}$ in a VMI spectroscopy. In our case, the spatial resolution of the detector, the Chevron MCP, is 100 µm which matches in addition the

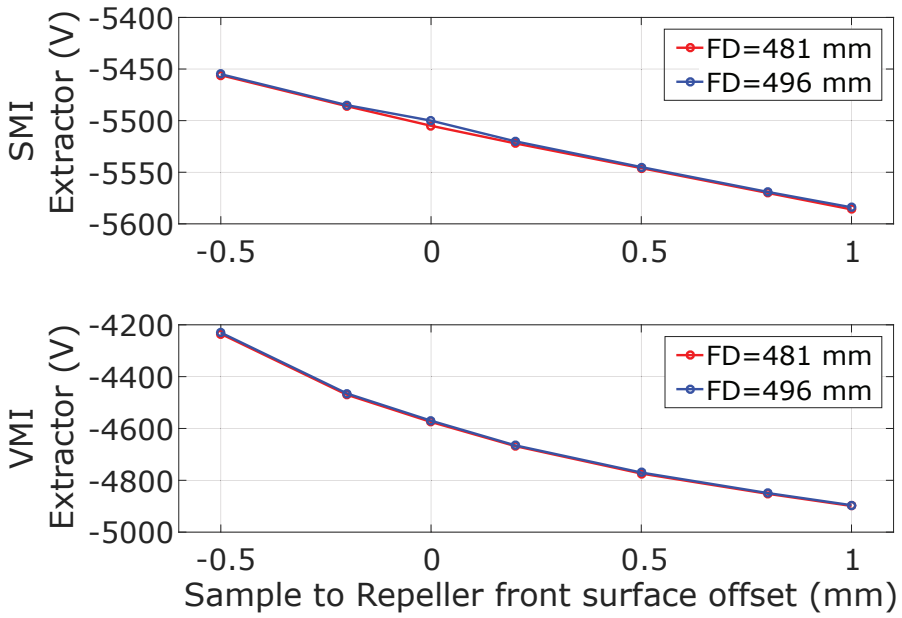

Figure 3.11: Top: SMI and bottom: VMI extractor potential for different position offsets from sample front to the repeller front surfaces. FD stands for flying distance in the figure legend.

resolution of a single camera pixel (dv_{2D}=8014 m/(s·pixel). This results in a transverse energy resolution of the spectrometer given by 0.2 meV $\leqslant dE \leqslant$ 90 meV. The lower boundary corresponds to the resolution in the detector center, whereas the upper boundary is the resolution at the edge. Therefore, compared to other techniques, our spectrometer has an unprecedented transverse energy resolution in the center. For our current settings the maximum detectable transverse energy is about 10 eV. This gives rise to a relative resolution of 1 % at the edge of the detector. It should be noted that the current transverse energy resolution could in principle simply be increased by using a larger detector, longer drift region, and a higher resolution camera. With, e. g., a detector with a diameter of 12 cm and a 1.5 m drift tube, a three times better resolution of 0.07 meV $\leqslant dE \leqslant$ 30 meV can be reached on a high resolution camera.

We further discuss systematic errors with respect to the resolution of the spectrometer. First, the power supply (in our case, HCP 14-12500 from FUG) applies the actual voltage, referring to the absolute voltage, to the repeller and extractor within an error of 25 V. The radius on the detector corresponding to a transverse velocity v_{2D} is given by $r = c\mathrm{TOF}v_{2D}$, where TOF denotes the time of flight (TOF) of the electrons. The magnification factor $c \approx 1$ of the spectrometer for velocity mapping is, fortunately, independent of the specific voltages applied to the spectrometer as long as the ratio of the repeller and extractor voltages is fixed, which can be calibrated and simulated with sufficient precision. The error for

the mapping is in principle only given by the TOF deviation due to the absolute repeller voltage bias. A voltage of 6000±25 V results in a TOF of 10.88±0.02 ns. This results in an error in the radius on the edge of the detector of 40 µm which is twice smaller than the resolution of the detector assembly. In addition, taking into account the work function of a material, typically on the order of few volts, therefore is also negligible. The other systematic error raised from the distance deviation between the cathode plane and the detector, i. e., 1 mm, results in a change in the time of flight of ∼20 ps. This error is therefore again negligible compared to the resolution of our detector.

3.6 Comparison with other techniques

Most of existing methods to characterize ultra-low-emittance photocathodes have already been presented in §2.2.5. They all have in common that the apparatus and corresponding transfer functions have to be modeled. The transversal energy resolution is typically worse compared to the one obtained with our spectrometer. The most outstanding advantage the VMI spectrometer holds is that single entire Newton spheres is captured at once and various Newton spheres are simply superimposed. This implies that the mapping is non-destructive in the sense that no filter functions like retarding voltages in combination with pinholes need to be applied as, e. g., for the 2D energy analyzer [46]. It avoids, therefore, slow electrons with trajectories extremely sensitive to any stray fields. Free expansion, reported as the simplest method by far [61], is the closest technique to the VMI spectroscopy demonstrated here. This technique is conceptually the analog to the early ion imaging experiments before the invention of the velocity-map-imaging spectrometer [51] as the common presence of the grids leads to transmission reduction, severe trajectory deflections and blurring due to the non-point source geometry. In addition, the incident laser, in the demonstrated free expansion setup [50], was focused onto the sample first through the grid which seriously deforms the starting intensity distribution. The high energy resolution of the VMI in comparison with the free expansion technique is attributed, as in the case of imaging molecular reaction dynamics, to the inhomogeneous electric field in the spectrometer. This allows, to first order, to get rid of the spatial contribution in the velocity coordinates. Therefore, a single measurement is sufficient to obtain the velocity map without contributions from the initial source distribution. Furthermore, non-cylindrically symmetric velocity distributions, e. g., obtained from nanotips, can be measured as well. As a final touch, operating the spectrometer under SMI conditions allows the mapping of the initial source distribution, which prevents the modeling of the active laser-matter interaction area. Overall, the simplicity of the VMI spectrometer and the super short experiment duration, typically in a few minutes, enables the easy

integration into more sophisticated electron sources.

Chapter 4

Multiphoton Emission from Planar Au Surface

After the calibration of the VMI spectrometer, as the first proof-of-concept experiment, the quantitative measurements of multiphoton emission and velocity distribution of photoemitted electrons from a planar Au surface are demonstrated in this chapter. The Fowler-Dubridge model and Berglund-Spicer three-step model previously described in chapter 2 have been implemented for analyzing the experimental results. In our experiments, the 2D transverse velocity/momentum distribution of photoemitted electrons was directly imaged onto the detector of the spectrometer. To compare with the theoretically derived 3D-space energy distribution, a mathematical algorithm is introduced to reconstruct the experimental 3D energy distribution from the measured 2D velocity distribution in §4.4, based on the angular distribution derived from the Berglund-Spicer model in §4.1.

4.1 Angular distribution

The angular distribution is of great importance for our data analysis, especially the reconstruction epitomized in §4.4. Here, we derive the angular distribution of photoelectrons. Starting from Eq. (2.9), for unscattered electrons, the intensity

This chapter is based on the articles:
H. Ye, J. S. Kienitz, S. Fang, S. Trippel, M. E. Swanwick, P. D. Keathley, L. F. Velásquez-García, G. Cirmi, G. M. Rossi, A. Fallahi, O. D. Mücke, J. Küpper, and F. X. Kärtner, "Velocity map imaging of electrons strong-field photoemitted from si-nanotip arrays," *Ultrafast Phenomena XIX* **162**, 663–666 (2015).
H. Ye, S. Trippel, M. Di Fraia, A. Fallahi, O. D. Mücke, F. X. Kärtner, and J. Küpper, "Velocity-map imaging for emittance characterization of multiphoton electron emission from a gold surface," *Phys. Rev. Applied*, 044018 (2018).

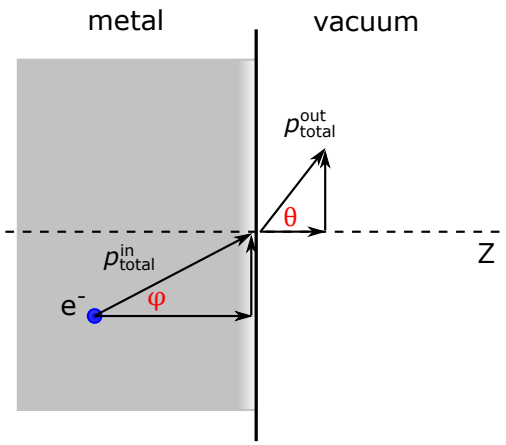

Figure 4.1: A diagram showing the conservation of momentum at the metal-vacuum interface.

$I(E_i, \theta)$ of the photoelectrons with energy E_i has the form [74]

$$\begin{aligned} I(E_i, \varphi) &= \frac{\aleph(E_i, h\nu)}{\int_0^{\varphi_0} 2\pi \cdot \sin\varphi \cdot \mathrm{d}\varphi} \\ &\propto K \cdot G_0(E_i) dE_i \cdot \frac{l}{\alpha l + 1} \end{aligned} \tag{4.1}$$

Again, φ denotes the angle between the wave vector of the excited electron in the metal and the normal to the surface. Fig. 4.1 shows a diagram of the electron's transition at the metal-vacuum interface. An electron at angle φ will be refracted to an angle θ at the vacuum-metal boundary, requiring conservation of transverse momentum across the metal-vacuum interface. Therefore,

$$P^{\text{in}}_{\text{total}} \cdot \sin\varphi = P^{\text{out}}_{\text{total}} \cdot \sin\theta \tag{4.2}$$

and

$$\aleph \equiv \frac{\sin\varphi}{\sin\theta} \tag{4.3}$$

expresses the electron analogy of refraction at the vacuum-metal boundary. The total momentum inside and outside the metal cathode of an electron absorbing photon energy $\hbar\omega$ with initial energy E are [75]

$$\begin{aligned} P^{\text{in}}_{\text{total}} &= \sqrt{2m(E + \hbar\omega)} \\ P^{\text{out}}_{\text{total}} &= \sqrt{2m(E + \hbar\omega - E_{\text{F}} - \phi_{\text{eff}})} \end{aligned} \tag{4.4}$$

Therefore,

$$\aleph \equiv \frac{\sin\varphi}{\sin\theta} = \frac{\sqrt{E + \hbar\omega - E_{\text{F}} - \phi_{\text{eff}}}}{\sqrt{E + \hbar\omega}} \tag{4.5}$$

The electron in the metal in the range $\delta\varphi$ will be refracted to the range $\delta\theta$ in the vacuum.

$$\aleph \cdot \cos\theta\delta\theta = \cos\varphi\delta\varphi, \qquad \frac{\delta\theta}{\delta\varphi} = \frac{\cos\varphi}{\cos\theta} \cdot \frac{\sin\theta}{\sin\varphi} = \frac{\tan\theta}{\tan\varphi} \tag{4.6}$$

Estimate a reduction factor

$$\frac{\delta\Omega}{\delta\Omega'} = \frac{\sin\varphi \cdot \tan\varphi}{\sin\theta \cdot \tan\theta} \tag{4.7}$$

where $\delta\Omega$ and $\delta\Omega'$ denote the solid angles subtended at O and O', respectively. The assumption is made that the distribution in energy of photoemitted electrons is similar to the distribution in energy of electrons in the solid after optical excitation [74]. Therefore,

$$\begin{aligned} I(E_i,\theta) = I(E_i,\varphi)\frac{\delta\Omega}{\delta\Omega'} \quad &\propto K \cdot G_0(E_i)dE_i \cdot \frac{l}{\alpha l+1} \cdot \frac{\sin\varphi \cdot \tan\varphi}{\sin\theta \cdot \tan\theta} \\ &\propto K \cdot G_0(E_i)dE_i \cdot \aleph^2 \cdot \frac{l}{\alpha l+1} \cdot \frac{\cos\theta}{\cos\varphi} \end{aligned} \tag{4.8}$$

As $\cos^2\varphi = 1 - \aleph^2 \cdot \sin^2\theta$,

$$I(E_i,\theta) \propto \aleph^2 \cdot \cos\theta \cdot \frac{l}{\alpha l+1} \cdot \frac{1}{(1-\aleph^2 \cdot \sin^2\theta)^{\frac{1}{2}}} \tag{4.9}$$

Assuming the photoemitted electron angular distribution is a linear combination of angular distributions over all the photoelectron energies, the angular distribution curve (ADC) is expressed as

$$I(\theta) = \sum_{E_i=0}^{E_{\max}} I(E_i,\theta). \tag{4.10}$$

Fig. 4.2 shows an example of an ADC plot for electrons photoemitted from Au planar surface illuminated by 800 nm Ti:sapphire laser pulses. In the following sections, the 4-photon emission is observed during the experiments giving the photon energy of $4 \times h\nu = 6.2$ eV. The Fermi level and work function of the Au metal is taken as 5.53 eV and 5.31 eV, respectively. As shown in Fig. 4.2, the distribution is nearly a cosine function. This can also be understand from the Eq. (4.9), the term $(1-\aleph^2 \cdot \sin^2\theta)^{\frac{1}{2}} \approx 1$ when $\aleph \ll 1$, which often happens for the photoemission from metal with the minimum required photon energy comparable to the work function. Please note, the photon energy in Eq. (4.5) need to be adapt to the multiphoton case. The angular distribution of photoemitted electrons provides us the opportunity to reconstruct the three dimensional velocity distribution from the two dimensional distribution.

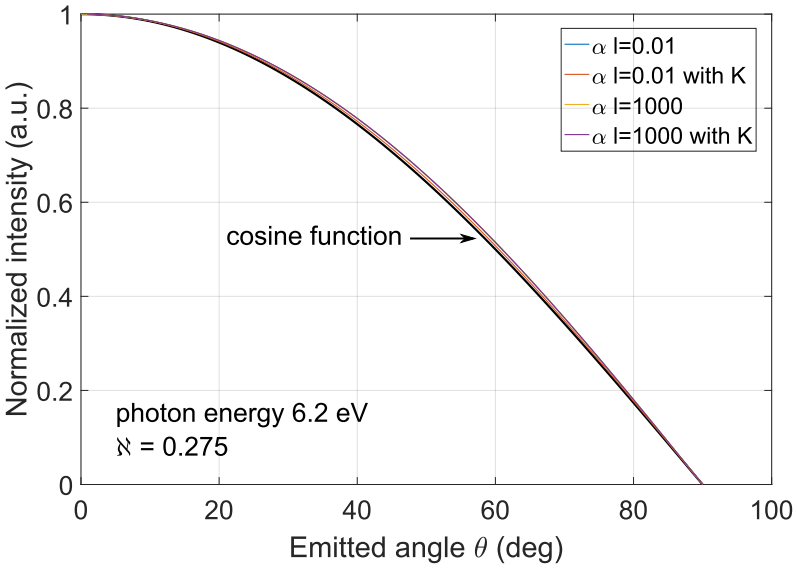

Figure 4.2: Angular distribution curve (ADC) of electron photoemitted from a planar Au surface illuminated at 800 nm by Ti:sapphire laser pulses. The Fermi level is 5.53 eV and work function is 5.31 eV. K is the corrector factor. The coefficient αl is varied from 0.01 to 1000 and hardly make a difference on the angular distribution. The black line is a cosine function plotted as a reference.

4.2 Quantum yield dependence

Fig. 4.3(a) shows, on a logarithmic scale, the photoemitted electron yield as a function of incident laser energy. The error bar shows the standard deviation of the photoemitted electron counts due to the laser fluctuations.

According to the Fowler-Dubridge model discussed in §2.1.2, the experimental data in Fig. 4.3(a) follow a power law with a slope of ~ 3.94, in agreement with a 4-photon emission process according to the nonlinear photoelectric effect, which indicates that simultaneous absorption of 4 photons (photon energy 1.55 eV at 800 nm) has to take place to overcome the metal work function ϕ [76], which is reported as 5.31–5.47 eV for Au [77]. As shown in Fig. 4.3(b), varying the laser polarization angle, the photoemitted electron intensity reaches a maximum when the laser is p-polarized (electric field normal to the sample surface), and appears minimum when it is s-polarized. For multiphoton emission at a certain incident light intensity, the electron yield mostly depends on the bulk absorption coefficient, expressed as term $(1-R)^n$ in the Fowler-Dubridge model [76]. R is calculated by Fresnel equations with $n_1 = 1$ and $n_2 = 0.189 + i4.71$ [78] at an incidence angle of $84\,^\circ$. The plotted $(1-R)^4$ curve fits very well with the data, which proves again the 4-th order multiphoton process.

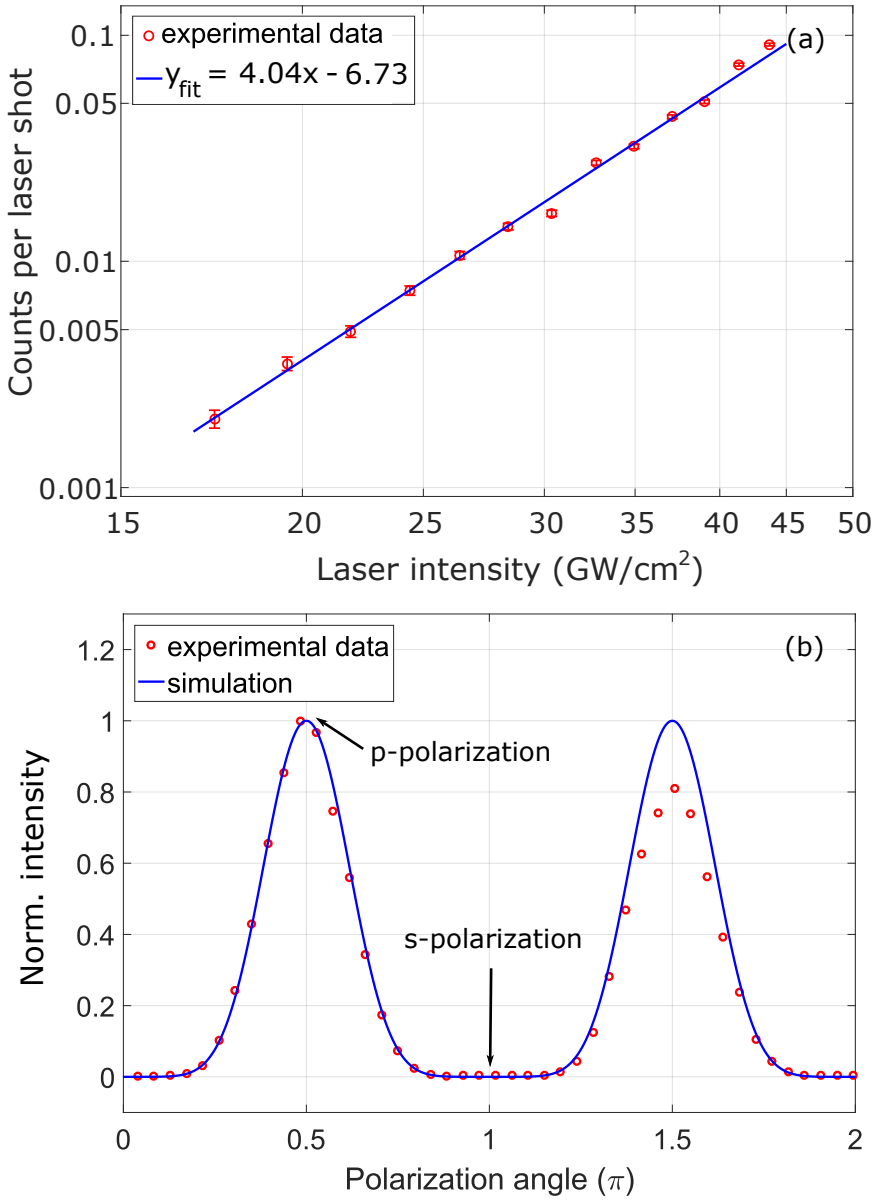

Figure 4.3: Counts of the photoemitted electrons as function of (a) laser peak intensity and (b) laser polarization angle. The experimental data for polarization angles $> \pi$ is of reduced quality due to laser drifting and *etc.*

4.3 Energy distribution

A velocity-map image from a planar Au surface is shown in the inset of Fig. 4.4(a). The image was integrated over 6×10^4 laser shots with an energy of $\sim$ 50 nJ, corresponding to a peak intensity of 4×10^{10} W/cm^2 on the cathode. Generally, in laser-induced multiphoton emission, the emitted electron velocity vectors exhibit cylindrical symmetry along the direction normal to the sample surface. Therefore, the center of mass (COM) of the image is set as coordinate origin. The corresponding angle-integrated radial velocity distribution of the projected electrons is plotted in Fig. 4.4(a) as black line. To allow for comparison with the theoretical model, the 3D velocity/energy distribution is required. Introducing a novel mathematical method similar to the Onion Peeling algorithm [79], we are able to reconstruct the momentum/energy distribution when the angular distribution of emitted electrons is known. As discussed in §4.1, for multiphoton emission, the intensity of photoemitted electrons at various angles θ can be derived from the Berglund-Spicer model [66] as

$$I(\theta) \propto \aleph^2 \cos\theta \cdot \frac{1}{1+\alpha\, l(E)} \cdot \frac{1}{\sqrt{1-\aleph^2 \cdot \sin^2\theta}} \tag{4.11}$$

where α is the optical absorption coefficient, $l(E)$ is the electron-electron scattering length for an electron of kinetic energy E, and $\aleph$ expresses the electron analogy of refraction at the vacuum-metal boundary [40]. For a small $\aleph$ (our case, $\aleph = 0.275$), meaning the photon energy $nh\nu$ is comparable to the work function ϕ, the equation can be simplified to $I(\theta) \propto \cos\theta$ [75, 74]. Therefore, the 3D velocity distribution can be reconstructed as is described in detail in §4.4.

The reconstructed velocity distribution is plotted as blue line in Fig. 4.4(a), and the smoothed energy distribution shown in Fig. 4.4(b). The energy distribution of the emitted electrons shows an energy spread of $\sim$ 1 eV, which corresponds to the energy difference between a four-1.55 eV-photon excitation and the Au work function of 5.31 eV.

The Berglund-Spicer three-step model is employed as the analytic expression for the kinetic energy distribution of the photoemitted electrons. As the model is derived for single-photon emission, it is implied in our analysis that the electrons at an initial energy state E_0 absorb sufficient number of photons simultaneously, rather than sequentially, to be pumped to a higher energy state $E = E_0 + nh\nu$. The kinetic energy distribution for single-photon emission [65] is adapted to multiphoton emission as

$$N(E)\,\mathrm{d}E \propto \frac{K\,C(E)\,\alpha}{\alpha + 1/l(E)}\,\mathrm{d}E \times \left[1 + 4\left(\frac{E-E_\mathrm{F}}{nh\nu} - 1 + \ln\frac{nh\nu}{E-E_\mathrm{F}}\right)\right] \tag{4.12}$$

where $C(E) = 0.5 \times (1 - \sqrt{\phi/E})$ for $E \geqslant \phi$ is a semiclassical threshold function. $l(E)$ is the electron-electron scattering length, which is proportional to $E^{-3/2}$. The

absorption efficient α is calculated from the extinction coefficient $k = 4.71$ as $\alpha = 4\pi k/\lambda$ and taken as a constant $\alpha = 7.7 \times 10^5$ cm^{-1} independent of electron energy. K is a correction factor related to both $C(E)$ and $\alpha\, l(E)$, which is between 0.5 to 1. To evaluate Eq. (4.12), the probability of a photon carrying energy $h\nu$ is calculated from the measured laser spectrum in the range from 760 to 850 nm. To overcome the barrier of 5.31 eV, an electron is assumed to always absorb four photons ($n \equiv 4$). Absorption of various photon energies leads to slight difference of the quantum yield at a certain emitted kinetic energy as one can see from Fig. 4.4(b). The main consequence of absorbing photons with various energies is the spectral/intensity broadening, which is illustrated by the color coding in Fig. 4.4(b), but with an essentially unchanged spectral shape. We mention that Eq. (4.12) only includes the emitted electrons that experience none or one electron-electron scattering process during transport to the metal-vacuum surface. Electron-electron scattering is dominant over electron-phonon scattering and reshapes the energy distribution on a fast timescale, i. e., during an ultrashort laser pulse.

The density of states (DOS), i. e., the number of states available for electrons at a certain energy level, is shown in the inset of Fig. 4.4(b). During the photoemission process, an energy state E_0 is first occupied by an electron, which is then excited to a higher energy state E, which was empty. As fermions, electrons obey the Pauli exclusion principle. In thermal equilibrium, the possibility of electrons to occupy an available energy state is given by the Fermi-Dirac (FD) distribution f_{FD}. However, excitation of a metal with ultrashort strong laser pulses initially creates a nonequilibrium distribution that then thermalizes via electron-electron scattering towards a Fermi-Dirac distribution. In gold, this thermalization occurs on a timescale of hundreds of femtoseconds [80, 81]. Subsequently, the electrons cool down by dissipating energy into the lattice via electron-phonon scattering occurring on a longer picosecond timescale. In the following discussion, where we employ the Berglund-Spicer model in our analysis, we assume that the electronic system can be described by a Fermi-Dirac distribution with quasi-equilibrium electron temperature T_e. Hence, the appropriate densities of states and FD distributions are multiplied with the energy distribution as $N(E)\mathrm{d}E\; f_{\mathrm{FD}}(E_0)\; \mathrm{DOS}(E_0)\; (1 - f_{\mathrm{FD}}(E))\; \mathrm{DOS}(E)$, resulting in the spectrum shown in Fig. 4.4(b).

The best fit with our reconstructed experimental energy distribution is obtained for an electron temperature of 6000 K. This is comparable to previously observed electron temperatures of 7000 K in surface-enhanced multiphoton emission from copper [82]. A two-temperature model (TTM), describing energy transfer between electrons and lattice through the time evolution of electron temperature T_e and phonon/lattice temperature T_l [83], is studied but does not predict these high T_e temperatures. More details are discussed in Appendix B. Therefore, the high energy tail of the spectrum indicates that very "hot" electrons are photoemitted by the femtosecond laser pulse, consistent with the high excess energy deposited

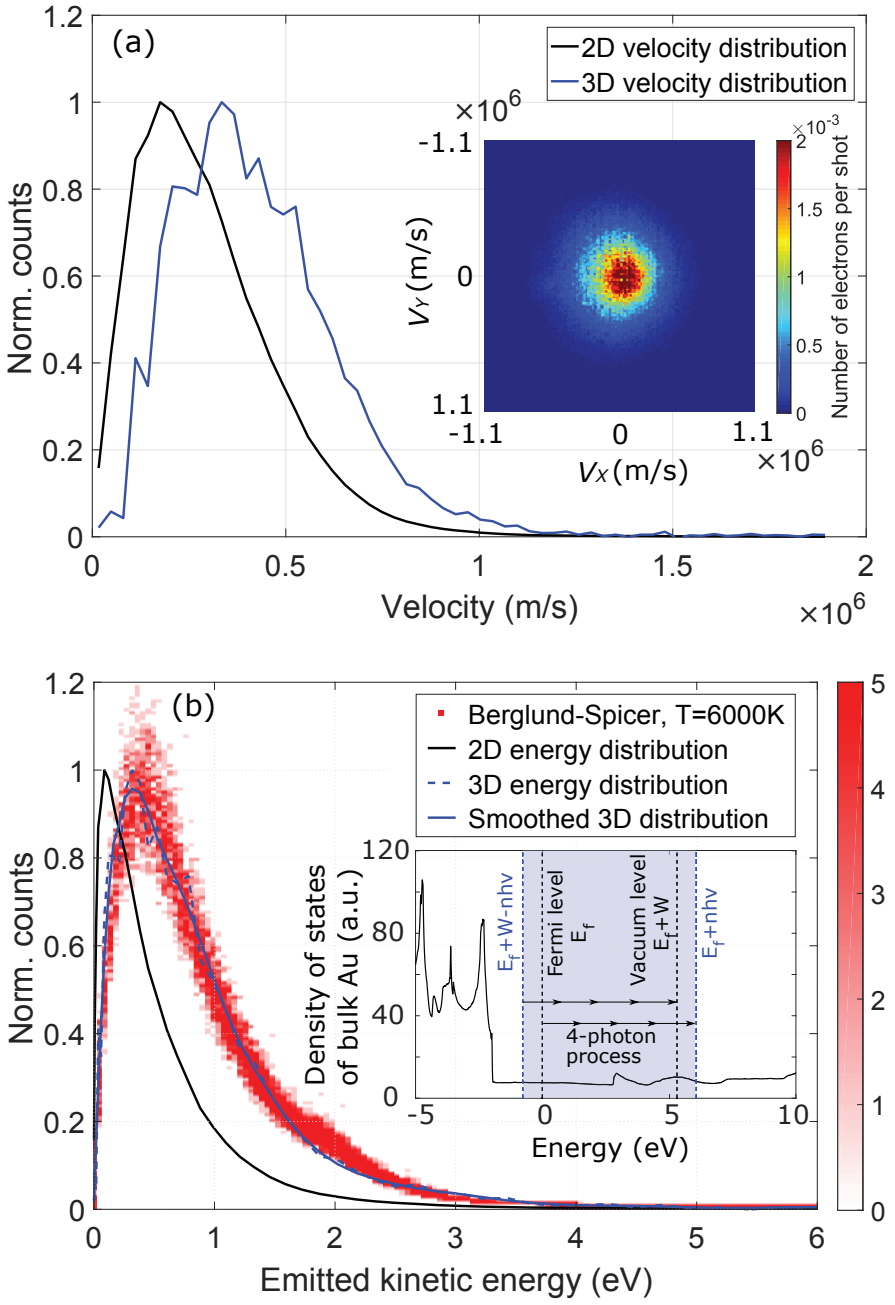

Figure 4.4: (a) Projected 2D (black curve) and reconstructed 3D (blue curve) radial velocity distribution of the measured velocity-map image that is shown in the inset. (b) Reconstructed kinetic-energy distribution and its simulation using the Berglund-Spicer model assuming an electron temperature of 6000 K. The color bar represents the probabilities of photoelectron kinetic energies due to the photon-energy spectrum of the laser. The inset shows the density of states calculated for bulk Au, which is used in the Berglund-Spicer model simulation. The blue area depicts the four-photon-ionization range.

into the electronic system. For the energy tail up to 4 eV, except for the high temperature, another process that might need to be taken into account is above-threshold photoemission (ATP), i. e., the absorption of one (or more) extra photon(s), occurring together with the four-photon process [84]. Moreover, for our experimental conditions, we can neglect tunnel ionization, which could result in high-energy emitted electrons. We estimate the absorbed peak intensity for the recorded image (inset Fig. 4.4(a)) to be $\sim 4 \times 10^9$ W/cm^2 taking into account Fresnel losses. This implies a Keldysh parameter $\gamma = \sqrt{\phi/2U_\mathrm{p}} \approx 17 \gg 1$, which is well in the multiphoton emission regime; here, $U_\mathrm{p} \propto \lambda^2 I$ is the ponderomotive energy with laser wavelength λ and intensity I.

Since both the measured quantum yield and the momentum distribution are in quantitative agreement with the Fowler-Dubridge and Berglund-Spicer models, as one would expect from multiphoton emission from a planar Au cathode, the VMI spectrometer has been proven as a tool to characterize the photoemitted electrons from cathodes, especially to directly measure the transverse momentum distribution. Assuming there is no correlation between the location of emission and the transverse momentum [40], the normalized rms emittance given by Eq. (2.30)

$$\varepsilon_{nx,\mathrm{rms}} = \frac{\sqrt{\langle x^2 \rangle \langle {p_x}^2 \rangle}}{m_0 c}. \tag{4.13}$$

From the velocity map image shown in the inset of Fig. 4.4(a), the normalized rms emittance of the planar Au photocathode irradiated by 45-fs 800-nm laser pulses with a focal spot size of $\sigma_x = 161$ µm and $\sigma_y = 17$ µm is characterized to be $\varepsilon_{n,x} = 148$ nm·rad and $\varepsilon_{n,y} = 14$ nm·rad in the x and y-directions, respectively.

4.4 Reconstruction algorithm

Our reconstruction algorithm for the conversion of the 2D projected velocity distribution to the 3D distribution is based on the assumption that the angular distribution of the photoemitted electrons is known. For our simulations, a cosine function $I(\theta) \propto \cos\theta$ [75, 74], derived from the Berglund-Spicer model [66] as discussed in §4.1, is applied in the algorithm. In addition, it is assumed that for multiphoton emission the angular distribution is independent of the modulus of the three dimensional velocity vector. The 3D velocity distribution is then obtained from the 2D projected distribution by a matrix method similar to Onion Peeling [79]. For multiphoton emission from a planar Au surface, the electrons are assumed to be photoemitted within a half sphere of $\varphi \in [0,\ 2\pi]$, $\theta \in [0,\ \pi/2]$. The photoemitted electron distribution has cylindrical symmetry with respect to the surface normal of the sample.

Fig. 4.5(a) shows a scatter plot for a single 3D velocity v_i distribution given by $f(v, \theta) = \delta(v - v_i)\cos\theta$. Fig. 4.5(b) shows the projection of this distribution onto

the 2D detector surface. It can be derived that the projected velocity distribution for this special case is

$$P_i(v_x, v_y) = \int f(v, \theta)\, \mathrm{d}v_z = \begin{cases} C & \text{for } v_{x,y} < v_i, \\ 0 & \text{otherwise} \end{cases}$$

where C is a constant. As shown in Fig. 4.5(b), the projected velocity distribution of $f(v, \theta)$ is constant inside the circular phase-space area of radius v_i. Furthermore, Fig. 4.5(c) shows the radial distribution obtained from the projected velocity distribution given by

$$\rho_i(v_{2\mathrm{D}}) = \int P_i(v_x, v_y)\, \mathrm{d}\theta_{2\mathrm{D}} = \begin{cases} 2\pi C \cdot v_{2\mathrm{D}} & \text{for } v_{2D} < v_i \\ 0 & \text{otherwise} \end{cases}$$

where $v_{2\mathrm{D}} = \sqrt{{v_x}^2 + {v_y}^2}$. In the reconstruction, each radial distribution $\rho_i(v_{2\mathrm{D}})$ is built up by a triangle as sketched in Fig. 4.5(d). v_i is taken equally spaced and form the intervals confined by the neighboring gray dashed lines. The 2D projected distribution is related to the 3D distribution f_i by a transfer matrix $\mathbf{M}$.

$$\rho_i = \mathbf{M} f_i, \tag{4.14}$$

with $\mathbf{M}$ given by:

$$\mathbf{M} = \begin{pmatrix} 1 & 1/4 & 1/9 & 1/16 & \cdots \\ 0 & 3/4 & 3/9 & 3/16 & \cdots \\ 0 & 0 & 5/9 & 5/16 & \cdots \\ 0 & 0 & 0 & 7/16 & \cdots \\ \vdots & \vdots & \vdots & \vdots & \ddots \end{pmatrix} \tag{4.15}$$

The 3D distribution can finally be obtained by inversion of the measured 2D-projected distribution

$$f_i = \mathbf{M}^{-1} \rho_i. \tag{4.16}$$

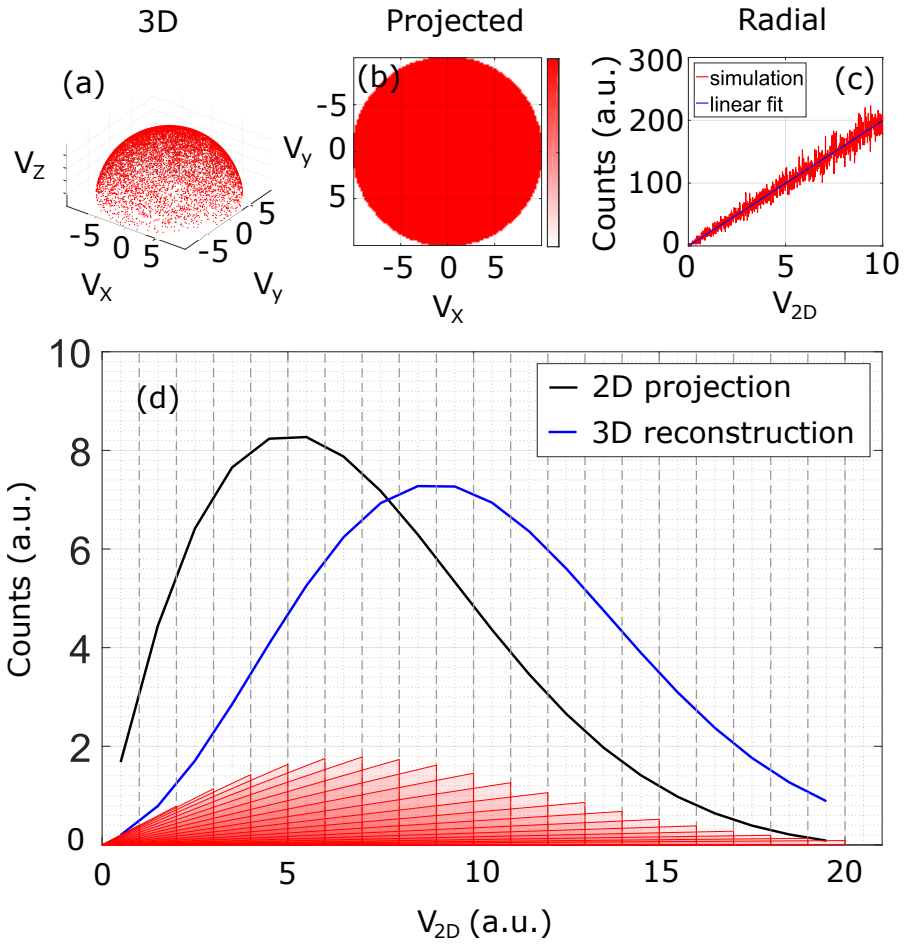

Figure 4.5: (a-c) Representation of a simulated electron bunch with a single 3D velocity v_i and an angular distribution of a cosine function: (a) in 3D, forming a spherical surface; (b) in 2D, yielding a uniform distribution in the detector plane; (c) in 1D, showing a linearly increasing radial velocity v_{2D} with distance from distribution COM. (d) A conceptual diagram of the reconstruction algorithm: The area of each red triangle at the bottom indicates the number of photoemitted electrons having the same 3D velocity. The corresponding distribution curve is plotted as blue curve. The black curve is the 2D projection distribution curve, summing up the number of photoemitted electrons within each interval of the same transverse velocity. The gray dashed lines indicate the transverse-velocity intervals used in this projection.

Chapter 5

Field Emission from Field-Emitter Arrays of Au nanorods

In this chapter, the experimental results obtained from field-emitter arrays of Au nanorods are presented. The photoemission dependency on the laser power and polarization have been studied for field-emitter arrays with different space between the Au nanorods. A patterned electron bunch has been achieved from the 75 µm spacing Au-nanorod array. In addition, a plateau in the energy spectrum due to the rescattering electrons has been observed from the 75 µm spacing Au-nanorod array under the condition when the electric field is normal to the surface. In the end, the emittance values obtained from various photocathodes in this thesis study are summarized.

5.1 Experimental layout

An experimental perspective of the laser spot illuminating an array of Au nanorods is shown in Fig. 5.1. The sinusoid represents the oscillated electric field. In the following experiments, the laser polarization was varied. To avoid confusion, the polarization is referred, in the experiments, with respect to the incident plane by convention, i. e., in Fig. 5.1, s-polarized electric field (black sinusoid) is parallel to the substrate plane. While p-polarized electric field (white sinusoid) has a component, which is perpendicular to the substrate plane and parallel to the electron flying direction towards the detector.

The samples used in the experiments are 1 mm×1 mm square of arrays of Au nanorods resting on a 30 nm indium tin oxide (ITO) layer on a 4 mm×4 mm

This chapter is based on the proceeding of IPAC2018:
H. Ye, A. Fallahi, S. Trippel, G. M. Rossi, O. D. Mücke, J. Küpper and F. X. Kärtner, "Characteriztion of Polarization-Dependent Emittance From an Array of Au Nanorods using Velocity-Map-Imaging Spectrometer," pre-released.

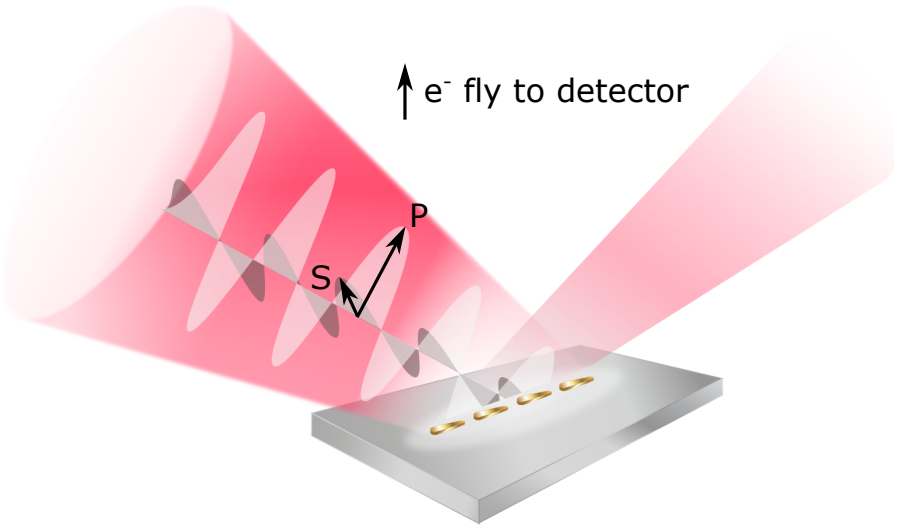

Figure 5.1: The layout of the Au-nanorod-array sample in the spectrometer with regard to the laser propagation. P and S depict the s- and p-polarized electric field used in the following experiments, respectively.

square SiO_2 substrate. Fig. 5.2 shows the scanning electron microscopy (SEM) images of two field-emitter arrays of Au nanorods used in the following experiments, spaced by different distances: 500 nm and 75 µm. The nanorods themselves have a dimension of 100 nm by 30 nm. Since the 75 µm spacing is considerably large compared to the nanorod dimension. The array can not be imaged by SEM at one time with the certain resolution. Therefore, the Fig. 5.2(b) shows an isolated Au nanorod.

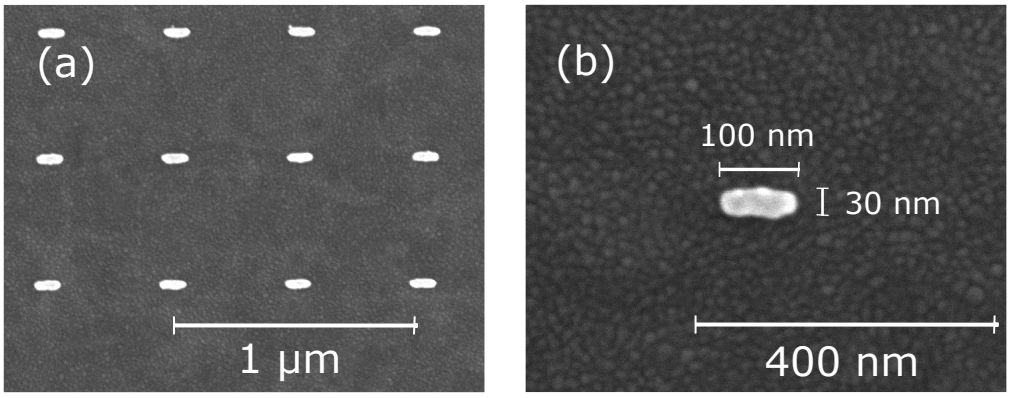

Figure 5.2: SEM images of (a) 500 nm and (b) 75 µm spacing Au-nanorod arrays. The nanorod itself has the dimension of 100×30 nm^2.

5.2 Experimental results from 500 nm spacing Au-nanorod array

In this section, ultrashort optical pulses at 800 nm from the 3 kHz Ti:sapphire laser system were employed to perform the experiments on the 500 nm spacing Au-nanorod array. With a laser focus spot size of ∼30×30 μm^2, projecting ∼300×30 μm^2 on the sample surface, about 4×10^6 nanorods were illuminated. However, the spatial resolution of the current spectrometer is several tens of microns, which lacks the ability to resolve the individual nanorods within the dense array in the SMI mode. Therefore, as shown in Fig. 5.3(a), the SMI image of the electron distribution looks very much like the one observed from the planar Au surface, portraying the shape of the laser spot on the sample. Varying the laser intensity and polarization, the experimental results shown in Fig. 5.3(b) and (c) both agree with a 4-th order photon emission process according to the Fowler-Dubridge model. In Fig. 5.3(b), the blue and red data were taken under different polarizations, 0° and 60° (p-polarization), respectively. They were both fitted to a linear function using logarithmic scales on both the horizontal and vertical axes, yielding slopes of 3.81 and 4.12, respectively. The quantum yield difference between the two polarizations is two orders of magnitude, which is consistent with the plot of the polarization dependence shown in Fig. 5.3(c). The curve is fitted to the term $(1-R)^n$ of the Fowler-Dubridge model, with R applied the Fresnel reflection coefficients at an incidence angle of 84°, and $n = 4$. The agreement with the experimental data points proves the 4-th order photon emission. During the experiments, we observed that the velocity distributions of the photoelectrons, i. e., VMI images, are identical under various polarization, except for the variation in the numbers of the photoelectrons due to the absorption coefficient discrepancy among the polarization. We inset two VMI images in Fig. 5.3(c) taken under two polarizations clarified in the figure. The unchanging velocity distributions reveal that the emission process depends, to a large extent, on the laser intensity rather than the field, which in turn serves as an evidence of multiphoton emission. Usually for velocity mapping, the broadness of a VMI image tells the expansion of the velocity coordinates. Therefore, compared to the VMI image taken from planar Au surface (see Fig. 4.4(a)), also under multiphoton emission regime, the emission from nanorods produces a slight broader velocity spread than the one from planar surface, mostly due to the electrons photoemitted from the sidewalls of the nanorods. A more comparison of momentum distributions from various samples will be presented in §5.4.

So far, the approach to the strong-field regime is prevented by the detector limitation. Since the photocurrent from a metal increases with the applied electric field in the multiphoton regime, not only overflowing electrons may beyond the

MCP threshold, but also the detector hardly acquire the accurate centroiding coordinates of all the photoelectrons to restore an valuable experimental image. In the following sections, we move to the 75 µm spacing Au-nanorod array, whereby less charge is expected due to sparse nanorods within the same laser illumination area.

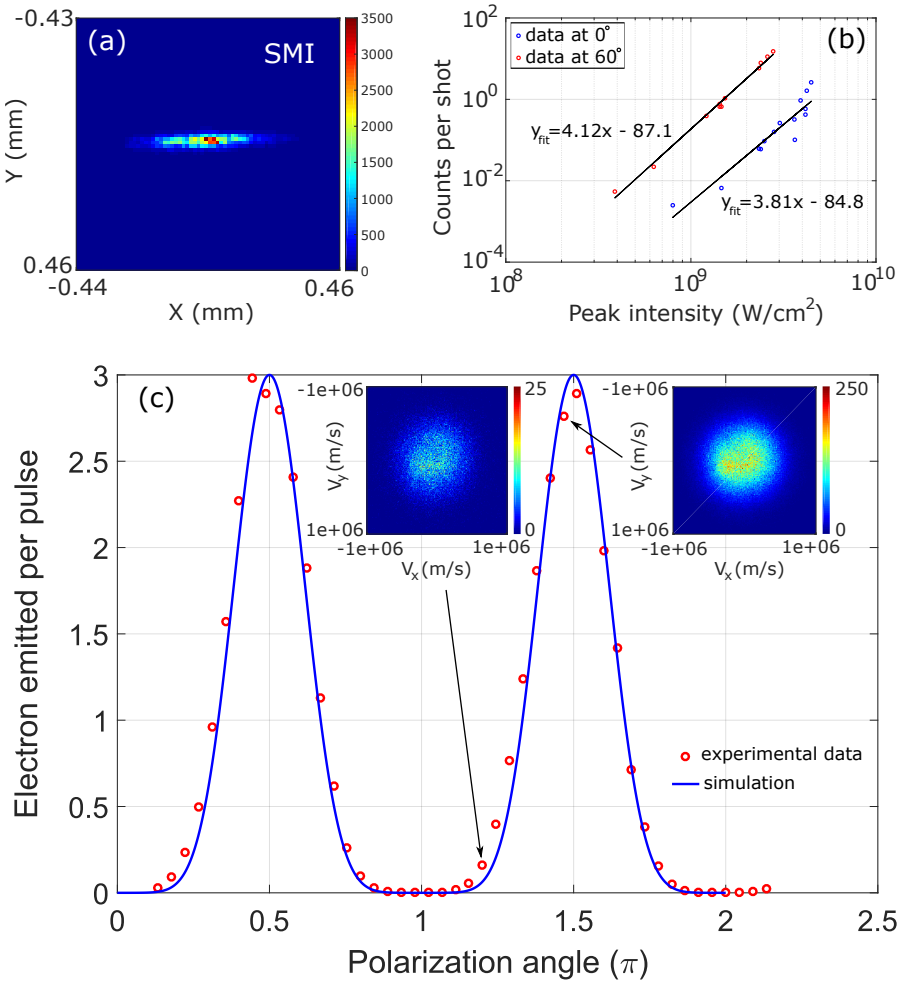

Figure 5.3: Experimental results for the 500 nm spacing Au-nanorod array. (a) SMI image; (b) the power dependence at polarization angles 0 ° (blue points) and 60 ° (red points); (c) the polarization dependence. The insets show two VMI images for different polarizations as indicated by the arrows.

5.3 Experimental results from 75 µm spacing Au-nanorod array

Optical pulses at center wavelength of 1.3 µm were focused onto the 75 µm spacing Au-nanorod array with a repetition rate of 1 kHz and a pulse duration of 100 fs.

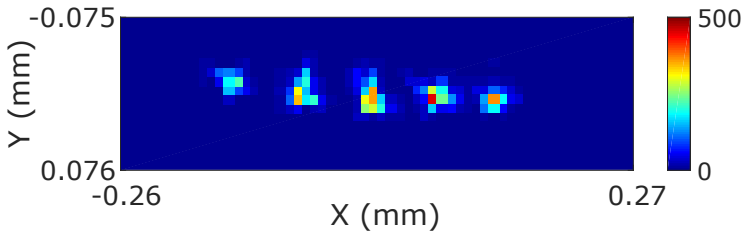

Figure 5.4: SMI image from 75 µm spacing Au-nanorod array showing five individual electron beamlets.

The size of the focus spot was intentionally kept as 300×30 µm^2 on the sample, by means of adjusting the optical telescope (a combination of lens L_1 and L_2 in Fig. 3.5). A foretype SMI image recorded from the 75 µm spacing Au-nanorod array is shown in Fig. 5.4, which is entirely different from the SMI images of both planar Au surface and 500 nm spacing Au-nanorod array. A spatially patterned electron bunch was observed, each emitted from a single nanorod within the field-emitter array, therefore spaced by 75 µm.

5.3.1 Laser intensity dependence

The photocurrent dependence on the laser intensity has been studied on the 75 µm spacing Au-nanorod array, showing results in Fig. 5.5. The double-blob ratio, plotted in Fig. 5.5(a), indicates the ratio of the electrons hitting on the same/adjacent position on the MCP, which can hardly be resolved as individual ones. When the double-blob ratio is above 10%, limited by the centroiding algorithm, the number of electrons is erroneous, therefore, the corresponding data points are marked hollow in Fig. 5.5(b). During the experiments, different MCP voltages, labeled in the legend, were applied for detecting photoelectrons, while the phosphor screen voltage was kept at 5 kV. Decreasing the MCP voltage helps resolve individual electrons, however, as a trade-off, it deteriorates the entire efficiency of the MCP that then detects less electrons.

The Keldysh parameter $\gamma = \sqrt{\phi_{\text{eff}}/2U_{\text{p}}}$ is commonly used to discriminate between photoelectric emission ($\gamma > 1$) and field emission ($\gamma < 1$). During the experiments, the maximum laser energy applied was 75 nJ. With an estimated enhancement factor of 3–5 due to the field confined by the nanostructures, the Keldysh parameter γ is 0.684–1.201 for the present field on the sample surface. This is consistent with the raw data plotted in Fig. 5.5(b), showing the photocurrent as a function of the laser field. The photocurrent first scales up with the laser field to the power of twice the minimum number of photons required to overcome the surface barrier, and grows smoothly into the tunneling regime. The data falls at the kink of the trend, which indicates the emission intertwines the multiphoton and

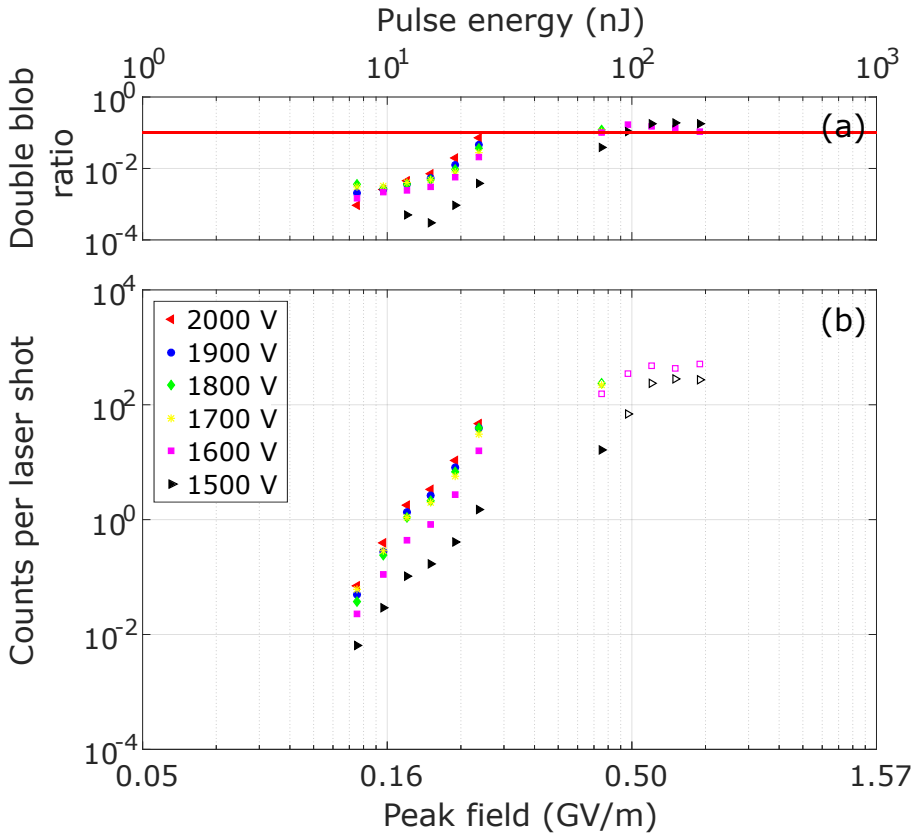

Figure 5.5: (a) Double-blob ratio of the data points; (b) counts of the photoemitted electrons per shot as function of laser energy or peak field. When the double blob ratio is beyond 10%, the data is marked hollow. The data points were recorded using different MCP voltages, labeled in the legend.

tunneling electrons. For the later experiments, most data were taken with laser energy of 75 nJ, allowing us to mostly approach the tunneling regime.

5.3.2 Laser polarization dependence

During the experiments, we deliberately moved the laser illumination spot on the sample, through controlling the focus lens position (lens L_3 in Fig. 3.5) via a 3D motorized stage, with each step of 10 µm in the horizontal direction and 10 steps in total. Due to the glancing incident angle, the position shift on the sample surface is roughly 10 times, i. e., 100 µm for one step. For each step, we scan the polarization of three polarization periods, i. e., 570 °, and record the SMI images with centroiding coordinates of photoemitted electrons shot by shot synchronized to the laser. By cutting the event range, we count only the electrons inside the chosen area of the images. Consequently, we are able to select the photoemitted electrons from certain nanorods, denoted as a, b and c in the SMI images of Fig. 5.7(c)

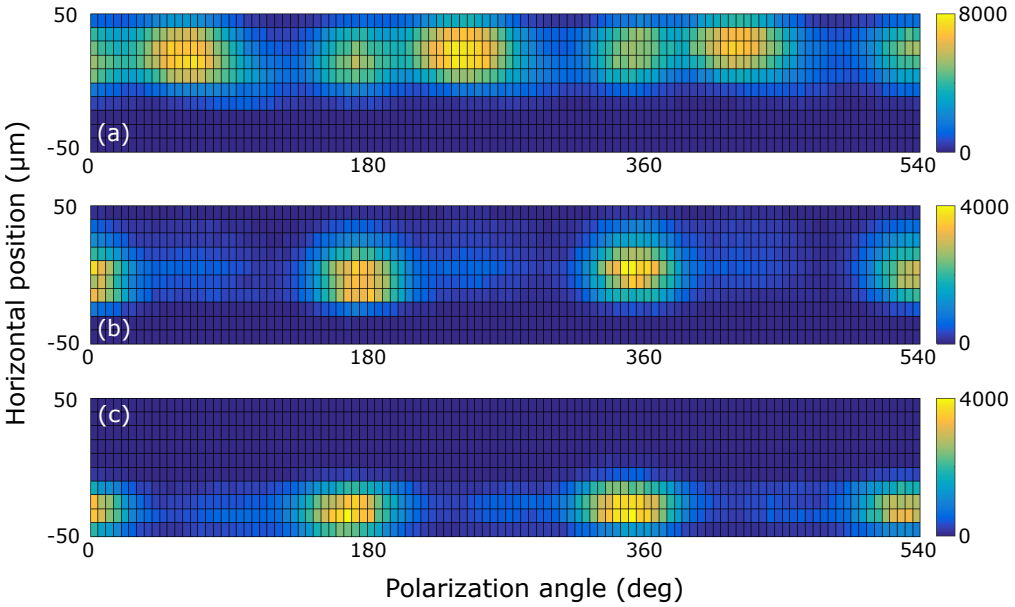

Figure 5.6: Surface plot of polarization dependence of (a) nanorod a; (b) nanorod b; and (c) nanorod c. The y-axis is the position shift of the focus lens in µm, which results in the laser focusing position shift on the sample surface with a factor of 10 times in the horizontal direction.

and (d), as well as the cutting range by white rectangular, and to investigate the polarization dependence on individual nanorods. The polarization dependence are show in Fig. 5.6(a)–(c) for nanorod a–c, respectively. The surface plot shows the polarization dependence as a function of laser focusing position (the horizontal position of lens L_3) with electron count number indicated by the color. For nanorod a, corresponding to Fig. 5.6(a), the quantum yield of photoelectrons shows a peak at s-polarization and a sub-peak at p-polarization. For nanorod b and c, see Fig. 5.6(b) and (c), the number of electron photoemitted at p-polarization is greater than at s-polarization by several hundreds times. We find that as far as the pulse is strong enough to excite electrons, the tendency of polarization dependence on nanorods has no dependency on the laser focus position within 1 mm range. The laser focus position, represented by the y-axis, has no influence in the quantum yield peak location along the polarization. We are aware that the rotation of the half wave plate leads to a shift of the laser position on the sample by less than 10 µm going from p- to s-polarization. Since all the three surface plots of position-polarization dependence are originally from one series of SMI images, no uncertainties or fluctuations are necessarily to be considered. We therefore believe that the variance of the polarization dependence is caused only by the nanorod uniqueness.

5.3.3 Transverse velocity and energy distribution

We look back to the spatial and velocity distributions from this field emitter array. The similarity and difference of the electron distributions, as recording images shown in Fig. 5.7, have been observed in the interest of the geometry of nanorods that are not tremendously identical for high-order nonlinear photoemission process. VMI images under p- and s-polarizations are shown in the top and bottom row, respectively, at three positions A, B and C, corresponding to horizontal position of -20, 0, and 20 µm in Fig. 5.6. The corresponding SMI images are placed on top of the VMI images to provide an intuitive reference of the ejected electrons appointed to the nanorod emitters within the array. Hot spots have been observed in the SMI images from certain nanorods.

Velocity distributions for all three positions are of interesting difference. Since the measurements were performed in the tunneling regime, where emitted electrons may be steered by the laser field. For the s-polarized laser field, the electric field results in a gain of the transverse momentum of photoemitted electrons, giving rise to a further velocity spread in the transverse direction, leading to broad VMI images. We are convinced that the VMI images under s-polarization containing the information of the nanorod morphology, nonetheless, difficult to interpret at the moment. Acceleration in the transverse direction amplifies the effect of photoelectrons emitted from the edges of the nanorods on the velocity distributions. Therefore, the VMI images under s-polarization of three positions differ from one another. In contrast, for a linearly p-polarized laser filed, the VMI images of three positions behave with a great similarity, even excluding the high nonlinearity symptom seen in the SMI images. As there is a field component perpendicular to the substrate surface, which accelerate electrons towards the detector. And the transverse components of the input laser field is canceled by the output one. Therefore, electrons photoemitted gain an additional longitudinal momentum from the laser field. With the transverse momentum kept as initialized, the divergence angle of photoelectrons is decreased, which is promising for improving the emittance.

The 2D energy distribution curves of the VMI images are plotted in Fig. 5.7(g). For the electron velocity distribution under s-polarization, although the VMI images are diversified, the shapes of energy distribution curve are comparable. The broadening of the energy distribution curve is attributed to the electrons photoemitted from the sidewalls. For the velocity distribution under p-polarization, the spectrum is an overall exponential decay followed by a plateau, a region of almost constant count rate extending from ∼2.2 eV to a cut-off located at ∼4.6 eV. As discussed in §2.1.6, the appearance of the plateau indicates that elastic rescattering of electrons is taking place. A fraction of the photoelectrons reencounters with the parent ion and elastically backscatters toward the detector. The highest energy the electrons can reach in this process is $E_{\text{cut-off}} = 10U_{\text{p}} + 0.538\phi$. With the pulse energy

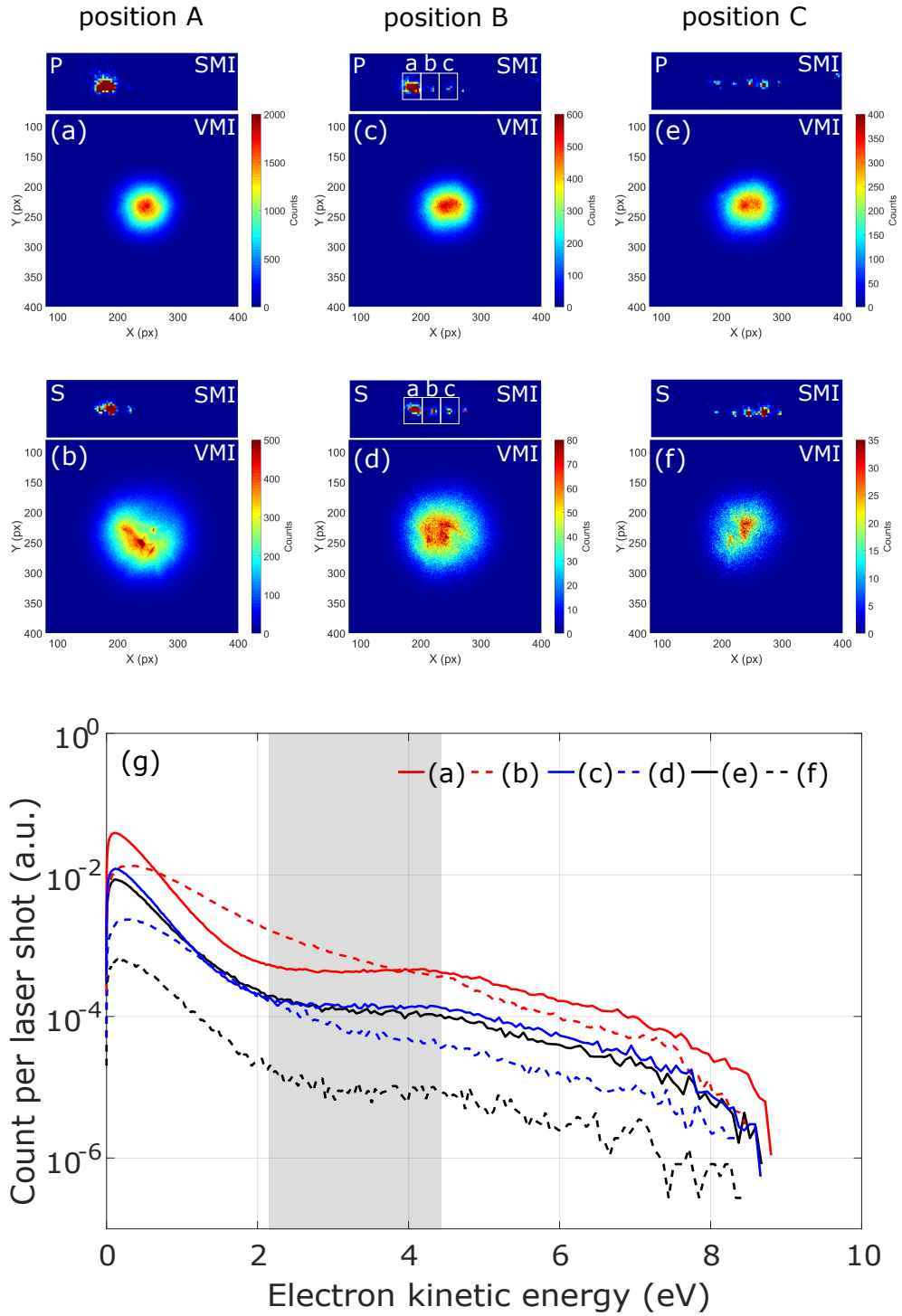

Figure 5.7: The VMI and SMI images at three positions A, B and C aligned in column. (a)(c)(e) were recorded with laser at p-polarization while (b)(d)(f) at s-polarization. (g) The energy distribution curves corresponding to the VMI images displayed.

of 75 nJ and an estimate enhancement factor of 3, U_{p} is equal to 1.368 eV and the $E_{\text{cut-off}}$ would be around 16.52 eV. However, the value drastically deviates from the cut-off energy of 4.6 eV conjectured in the energy spectrum. We speculate that large amount of the kinetic energy has contributed to the longitudinal dimension, which cause the significant reduction here. Unfortunately, the reconstruction of 3D velocity distribution, so to the 3D energy spectrum, is not feasible. Compassing too complex physics, no single angular distribution can be derived or approximated.

5.4 Emittance comparison

Although the interpretation can be complicated by inhomogeneous broadenings from nanostructures and the inclusion of complex photoemission mechanisms, there is no conflict for the characterization of the emittance as it is, compassing all the practical imperfections of the photocathodes and laser pulses. We exhibit the VMI and SMI images measured for various photocathodes in Fig. 5.8 and compare the emittance. From all the SMI images, the emission area is equal to or smaller than the laser illumination area on the sample. For the emission processes with relative low charge, meaning the space charge effect excluded, the σ_x and σ_y are proportional to the focal diameter of the laser beam. The momentum spread σ'_x and σ'_y is what we are interested in, holding the promise to decrease the emittance through pioneering control on the light-matter interactions. The normalized momentum spreads obtained from various photocathodes are summarized in Table 5.1 as well as the experimental conditions.

Table 5.1: Normalized momentum spread (in mrad) compared for various photocathodes.

Experiments	Emission	σ'_x	σ'_y
planar surface: 800 nm p-polarization	multiphoton	0.801	0.842
500 nm array: 800 nm p-polarization	multiphoton	1.100	1.070
75 µm array: 1300 nm p-polarization	strong field	0.889	0.847
75 µm array: 1300 nm s-polarization	strong field	1.111	1.083

Overall, the optimum minimal velocity spread is found from the planar Au surface. We believe that the artificial nanostructures expand the emission angle, therefore broadening the divergence angle of an electron bunch, in spite of different emission mechanisms. In the strong-field emission regime, the laser polarization plays an important role on the transverse energy spread. A smaller rms-normalized divergence of ∼0.85 mrad with the laser polarization normal to the sample surface has been obtained, compared to the ∼1.1 mrad for the parallel case. From the

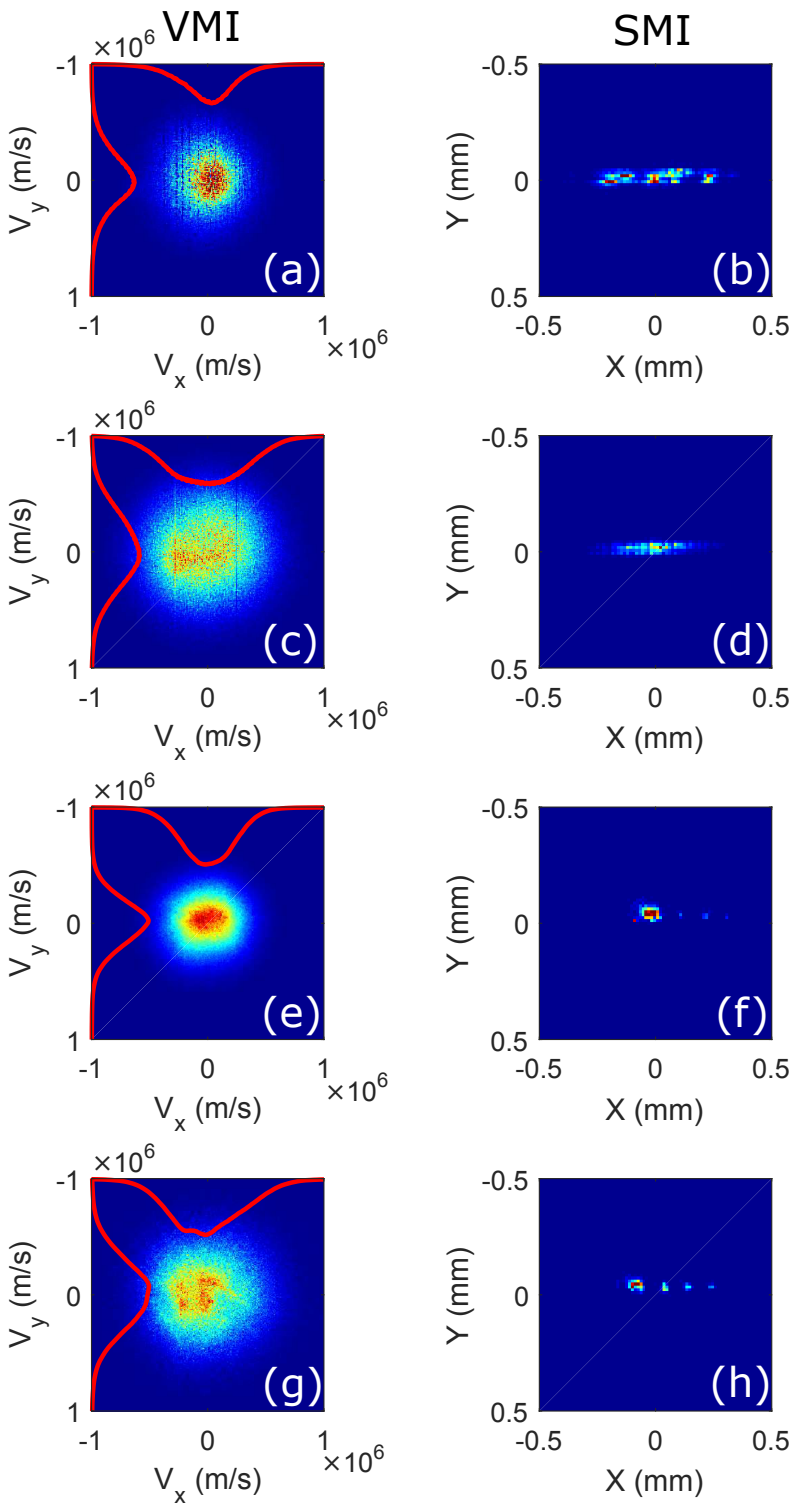

Figure 5.8: VMI and SMI images of (a) and (b) a planar Au surface multiphoton emission at 800 nm under p-polarization; (c) and (d) 500 nm spacing Au-nanorod array for multiphoton emission at 800 nm under p-polarization; (e) and (f) 75 µm spacing Au-nanorod array for strong-field emission at 1.3 µm under p-polarization; and (g) and (h) under s-polarization.

SMI images of 75 µm Au-nanorod array, it is evident that despite the laser spot size, the actual emission region is limited to several well-defined nanorods with a dimension of 100×30 nm^2 each. Although the velocity coordinates in the VMI images can not be separated and assigned to a single nanorod, no larger velocity spread would be obtain than the mixture of several ones. Therefore, the normalized transverse emittance for a single electron bunch within the patterned electron bunch is $\varepsilon_x = 0.07$ nm·rad and $\varepsilon_y = 0.02$ nm·rad.

Chapter 6

Conclusion and Outlook

We demonstrated an electron spectrometer with SMI and VMI capabilities, which intuitively allows for the measurement of the normalized transverse emittance of photocathodes, i. e., through the direct observation of the transverse position and momentum distributions. We verified and benchmarked the capabilities of the instrument in a proof-of-concept experiment, in which we characterized the photoemitted electrons from a 400 nm thin Au film. For ultrashort femtosecond laser pulses with a peak intensity on the order of 10^{10} W/cm^2 at 800 nm central wavelength multiphoton emission is shown to be the dominant contribution to the entire electron current.

As a first proof-of-principle example, we report on quantitative measurements of multiphoton emission from a 400 nm thick Au thin film at room temperature, which was excited with 45-fs laser pulses centered at 800 nm. These measurements additionally allowed us to benchmark the performance of this new experimental setup. Quantum-yield-dependent measurements were performed by recording the events of electrons impinging on the detector when varying the average laser intensity and the polarization angle, respectively. These experimental results confirm that four-photon emission occurs at the planar Au surface. In our experiments the 2D transverse velocity/momentum distribution of photoemitted electrons was directly imaged onto the detector. An experimental 3D energy distribution was reconstructed from the measured 2D VMI data using a mathematical algorithm and compared to the theoretically derived 3D-space energy distribution from the Berglund-Spicer photoemission model. The very good agreement of our experimental results with the theoretical model demonstrates the applicability of VMI for the characterization of the normalized transverse emittance of photoelectron emitters.

Therefore, we utilized this new setup for the emittance characterization of electron bunches strong-field emitted from nanorods under optical field irradiation. Two different types of nanorod samples, i. e., the 500 nm and 75 µm spacing Au-nanorod array with a single nanorod of dimension 100×30 nm^2, were studied. The

multiphoton emission process has been observed from 500 nm spacing Au-nanorod array by 45-fs 800-nm Ti:sapphire laser pulses. The quantum-yield-dependent measurements on the laser intensity and polarization both confirm the 4-th photon process. The velocity spread is found to be larger than the one from a planar Au surface due to the surface structure of intense nanorods, which broaden the emission angle by the reason of photoemission from the sidewalls.

The experiments on the 75 µm spacing Au-nanorod array were carried out using 1300-nm 100-fs laser pulses operated at 1 kHz. A patterned electron bunch has been observed, each emitted from a single nanorod within the array. The number of photoemitted electrons as a function of laser field shows an emission process happening at conjunction of multiphoton and field emission using pulse energy of 75 nJ. A plateau due to the rescattering electrons steered by the laser field has been observed. Further approach to the well-confined tunneling regime is prevented by the detection system. A polarization dependent photoemission study has been performed showing a smaller rms-normalized divergence of 0.8 mrad with the laser polarization normal to the sample surface, compared to 1.15 mrad for the parallel case. Despite this, the quantum-yield dependence on the polarization is non-committable, alternatively on the individual nanorods.

Outlook

On the basis of our studies, future investigations are expounded from two perspectives. Improvements of the spectrometer will enable improved control in the experiments. The characterization will enhance our understanding the fundamentals of light-matter interaction of the solids and nanostructures.

- Improvement of the spatial resolution in SMI mode

  As the current spectrometer has a spatial resolution of tens of microns, which prevents our observation of the photoemission area and the characterization of the electron source size, in particular for nanostructures. A detailed study to characterize the parameters of SMI imaging process has been presented describing the influence of different parameters by means of a Taylor expansion [95]. A spatial resolution of better than 4 µm out of a focal volume of several mm in diameter has been achieved experimentally. Learning from scanning electron microscopy, where the electron beam is focused to a spot about 0.4 nm to 5 nm in diameter by one or two condenser lenses, a magnetic lens could be implemented into the spectrometer located between the ground electrode and the MCP, which holds the promise to improve the spatial resolution into sub-µm via focusing and defocussing. In this case, in addition to the magnification factor determined by the voltage settings of the electrodes, the overall magnification can be controlled by the current supplied to the

magnetic lens.

- Characterization of contamination deposited on samples

  Following the discussion of the polarization dependence on the 75 µm spacing Au-nanorod array, the nonidentical morphology of nanorods within the array would be the primary reason for different behaviors from different nanorods. However, the surface contamination takes its place to influence the emission process mostly on the quantum efficiency. To investigate the pollution level of the surface, the spectrometer can be operated in analogy to a field ion microscope. With a high static field gradient on the order of GV/m on the sample, the contamination will be ionized with ions flying to the detector and electrons back into the sample. With appropriate voltage settings, the VMI spectrometer works as a mass spectrometer which would tell the contamination composition.

- Photoemission investigations with various laser pulses

  Intuitively, the laser source as an indivisible element plays an important role in photoemission related research fields. For the photoelectric emission regime, the maximum energy is $h\nu - \phi$. So varying the wavelength to match the $h\nu$ to the emitter work function in order to achieve the minimum kinetic energy upon emission is one way to decrease the transverse energy spread, so to the normalized transverse emittance. Tunable wavelength would be performed on photocathodes to see the transverse velocity spread dependency. For the strong-field emission regime, upon illumination with femtosecond laser pulses, electrons become photoemitted and accelerated by the laser near field. Therefore, the maximum kinetic energy an electron would obtain scales up with the laser wavelength until the electron has a larger oscillation amplitude and therefore experiences the decay of the near field. A study has demonstrated that the quiver motion of the electron can be quenched for infrared radiation [96].

- Coherent control at various nanostructured emitters

  The carrier-envelope (CE) phase of the laser pulses has an important influence on the emission process from these emitters and the generated ultrashort electron bunches. This CE phase dependence has been demonstrated in [33] from a tungsten nanotip, as well as the first observation of the plateau at tips caused by the electron rescattering. Recently, a ∼200 as electron source has been achieved from these tips [97]. The ultrafast generation of electrons from tailored metallic nanoparticles has been demonstrated to unravel the role of plasmonic field enhancement by comparing resonant and off-resonant particles [98]. A field emitter array consisting of resonant nanotriangles has

been demonstrated to have the CE phase effect on the emission [35]. In addition to all these interesting phenomena, we would like to characterize the two-dimensional transverse velocity distribution from these emitters under comparable experimental conditions. Overall, it serves an electron bunch with great brightness.

Our ongoing work targets the characterization of electron emission from a single nanotip or field emitter arrays, which are predicted to provide high-current low-emittance coherent electron bunches in the strong-field emission regime. The demonstrated imaging spectrometer will thereby foster the further development of ultrafast electron microscopy and diffraction [36, 99] and also open up new opportunities in the study of correlated electron emission from surfaces [100] and vacuum nanoelectronic devices [101].

I would like to devote the last paragraph of this dissertation to thank the funding agencies. Besides DESY, this work has been supported by the excellence cluster "The Hamburg Center for Ultrafast Imaging – Structure, Dynamics and Control of Matter at the Atomic Scale" (CUI, DFG-EXC1074), the priority program QUTIF (SPP1840 SOLSTICE) of the Deutsche Forschungsgemeinschaft, the European Research Council under the European Union's Seventh Framework Programme (FP7/2007-2013) through the Consolidator Grant COMOTION (ERC-Küpper-614507) and the Synergy Grant AXSIS (ERC-Kärtner-609920), the Helmholtz Association "Initiative and Networking Fund", and the accelerator on a chip (ACHIP) program funded by the Betty and Gordon Moore foundation.

Appendix A

COMSOL simulations of velocity mapping for a tungsten nanotip

COMSOL was used to carry out the simulations of the electrostatic lenses performance of the spectrometer for a single tungsten nanotip, as a prediction for future experiments. Different from the planar metal surface or arrays on a planar substrate, the nanotip (5 mm in length, 100 µm in diameter, with a curvature of 50 nm at the tip apex) is planned to be mounted upright on the sample holder (see Fig. A.1), and brought into the middle between the repeller and the extractor plates without touching the repeller plate. Therefore, an additional voltage is required to be applied to the sample holder to configure the electrostatic field for imaging. In the simulations, the tip cone is designed as a square pyramid.

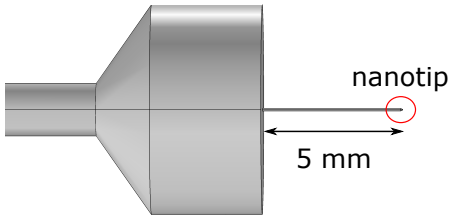

Figure A.1: Geometry of a tungsten tip on the sample holder

As shown in Fig. A.2(a), the field configuration of the electrostatic lenses surrounding the metal nanotip is highly distorted by the presence of the nanotip. The color bar applies to the voltage (in V) of the electrostatic field. Compared with the one simulated for the planar Au surface, in Fig. A.2(b), the field lines adjacent to the sample surface are considerable flat, which is crucial for effectively mapping the velocity coordinates. Therefore, with fixed repeller voltage at -6 kV, by adjusting the voltages applied to the sample holder/nanotip and extractor, we aimed to make the field lines, close to the free end of the nanotip, parallel to the

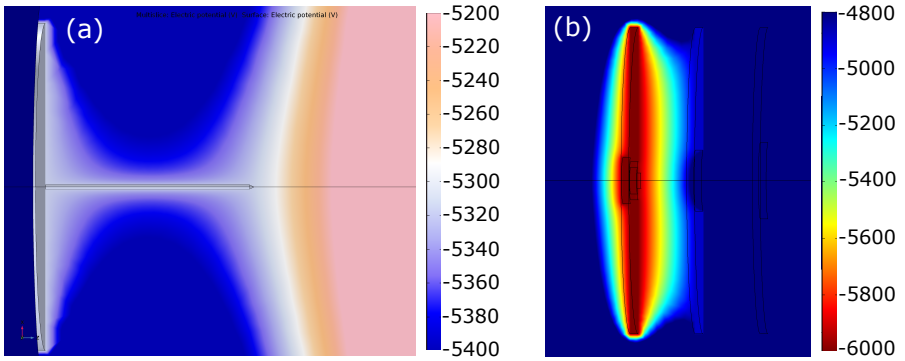

Figure A.2: Electrostatic field configuration for (a) the single nanotip and (b) the planar surface under velocity-mapping condition. The color bars represent the voltage (in V) of the electrostatic field.

sample holder surface. The nanotip location with respect to the distance between repeller and extractor plates, by means of adjusting the length of the nanotip, plays an important role along with the voltages.

The best achievable VMI voltages via COMSOL simulation are founded as R: -6000 V, E: -4575 V, G: 0 V and sample holder: -5315 V. The electron trajectories are calculated under this voltage settings, showing the results in Fig. A.3. The color bar indicates the scale (in m/s) of the transverse velocity $V_{2D} = \sqrt{{V_x}^2 + {V_y}^2}$. A thousand of photoemitted electrons are initialized from the surfaces of the square pyramid with zero transverse momentum and only accelerated by the potential gradient of the electrodes. The time of flight to the detector, which is ∼500 mm apart from the nanotip, is 13 ns. The electron bunch suffers a transverse velocity spread of $\sim 10^5$ m/s (corresponding to 0.0284 meV) at the detector plane from the field distortion.

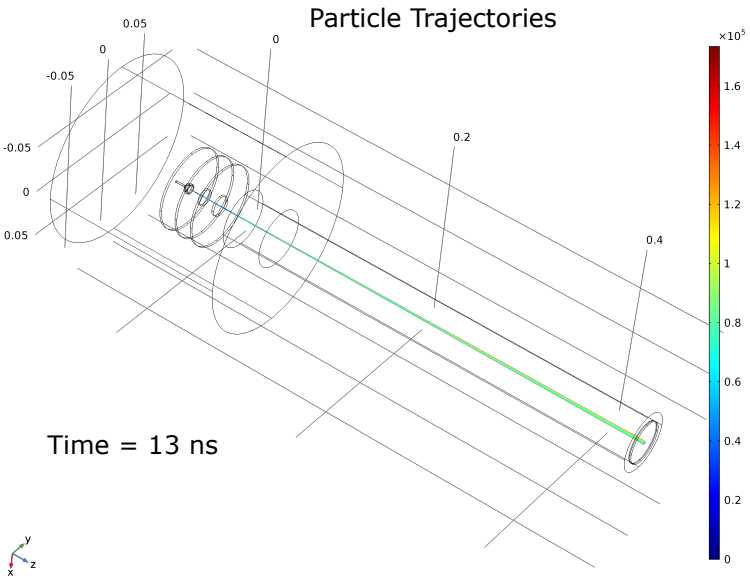

Figure A.3: Electron trajectories simulated for a tungsten tip using the velocity-mapping field configuration. The color bar indicates the scale (in m/s) of the transverse velocity V_{2D}.

Appendix B

Electron and lattice temperatures

The theoretical method to study the temperature evolution of the electron system and the lattice due to the absorption of a laser pulse within the solid is the well-known two-temperature model (TTM) [83]. According to the TTM, the time evolution of the electron temperature T_e and lattice temperature T_l, through the energy transfer between electrons and phonons, is governed by two coupled nonlinear differential equations:

$$C_e \frac{\partial T_e}{\partial t} = \frac{\partial}{\partial x}(k_e \frac{\partial T_e}{\partial x}) - G(T_e - T_l) + S \tag{B.1}$$

$$C_l \frac{\partial T_l}{\partial t} = \frac{\partial}{\partial x}(k_l \frac{\partial T_e}{\partial x}) + G(T_e - T_l) \tag{B.2}$$

where t is the time, x the depth, T_e the electron temperature, T_l the lattice temperature. C_e is the electron heat capacity, which is proportional to the electron temperature, when the electron temperature is less than the Fermi temperature, as $C_e = \gamma\ T_e$ and $\gamma = \pi^2 n_e k_B / 2T_F$, where n_e is the density of electrons, k_B is the Boltzmann constant. C_l the lattice heat capacity. As the temperature changes, the variation of the lattice heat capacity is relatively small, we take it as a constant. k_e is the electron thermal conductivity $k_e = k_{e0} B T_e / (A T_e^2 + B T_l)$ with k_{e0}, A and B representing material constants. k_l is the lattice thermal conductivity. G is the electron lattice coupling factor. Many of the ultrafast laser heating analyses have been carried out with a constant electron-lattice coupling factor G. Due to the significant changes in the electron and lattice temperatures caused by high-power laser heating, $G = G_0(A(T_e + T_l)/B + 1)$ should be temperature dependent. S the laser heat and can be modeled with a Gaussian temporal profile:

$$S = \sqrt{\frac{4 \cdot ln(2)}{\pi}} \frac{I(1-R)}{t_p \alpha} \exp[-\frac{x}{\alpha} - \beta \left(\frac{t - 2t_p}{t_p} \right)^2] \tag{B.3}$$

where I is the incident energy, R the reflection coefficient, t_p the FWHM, and α is the penetration depth including the ballistic range.

The TTM model has been adopted to simulate the energy transfer between electron and lattice induced by intense laser pulses, showing the results in Fig. B.1 using a laser energy of 80 nJ. The parameters implemented into the TTM model are listed in Table B.1 and mostly taken from [102].

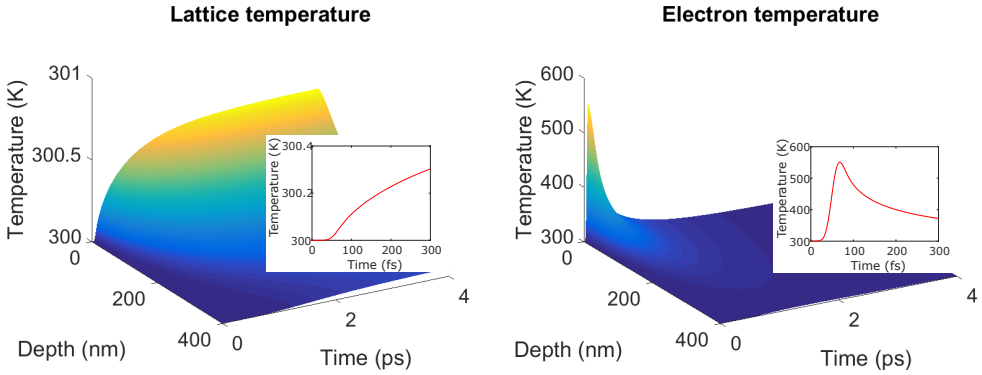

Figure B.1: (Left) lattice and (right) electron temperature evolutions of bulk Au under ultrafast laser pulse excitation versus time and depth. The two curves in the insets clearly shows the temperature variation at the surface.

Table B.1: Parameters taken into TTM

Material parameters for Au			Laser parameters		
G_0	$(10^{17}\mathrm{Jm^{-3}s^{-1}K^{-1}})$	0.21	R		0.96
γ	$(\mathrm{Jm^{-3}K^{-2}})$	68	I	(nJ)	80
k_{e0}	$(\mathrm{Jm^{-1}s^{-1}K^{-1}})$	318	τ_p	(fs)	45
C_l	$(10^{6}\mathrm{Jm^{-3}K^{-1}})$	2.5	σ_x	(µm)	240
α	$(10^{-9}\mathrm{m})$	13.7	σ_y	(µm)	30
A	$(10^{7}\mathrm{s^{-1}K^{-2}})$	1.18			
B	$(10^{11}\mathrm{s^{-1}K^{-1}})$	1.25			
T_m	(°C)	1064			

The results show that the electron system reaches the highest temperature of around 550 K after 70 fs, while the lattice system are kept almost unchanged. This is not consistent with the high temperature we investigated in the Berglund-Spicer model but stands to reason. Since the assumption for the TTM, which is in principle. where the thermal equilibrium among the electron systems is initially established and constantly kept, so does the lattice system. The laser-matter interaction driven by the ultrafast laser pulse breaks the assumption.

Appendix C

Definition of Notations

Table C.1: Definition of notations used in the dissertation

Notation	Definition
c	Vacuum speed of light
e	Electron charge
m	Free electron mass
h	Planck constant
$\hbar$	Reduced Planck constant
ϵ_0	Vacuum permittivity
μ_0	Vacuum permeability
γ	Lorentz factor
ν	Light frequency
λ	Light wavelength
ε	Emittance
ε_n	Normalized emittance
f	Focal length
L_x	Transverse coherent length
k_{B}	Boltzmann constant
T	Absolute temperature
f_{FD}	Fermi-Dirac distribution
β_{F}	Electric field enhancement factor
E_{F}	Fermi energy
E_{kin}	Kinetic energy

Continued on next page

Table C.1: Definition of notations used in dissertation

Notation	**Definition**
E_{ph}	Photon energy
ϕ	Work function
ϕ_{eff}	Effective work function
ϕ_{Schottky}	Schottky barrier
$\lambda_{\mathrm{e\text{-}e}}$	Electron-electron scattering length
VMI	Velocity map imaging
SMI	Spatial map imaging
1D	One dimensional
2D	Two dimensional
3D	Three dimensional
FEL	Free electron laser
XFEL	X-ray free electron laser
ICS	Inverse Compton scattering
UED	Ultrafast electron diffraction
UEM	Ultrafast electron microscopy
SASE	Self-amplified spontaneous emission
DLA	Dielectric laser acceleration
MTE	Mean transverse energy
DOS	Density of state
COM	Center of mass
RMS	Root mean square
FWHM	Full width half maximum
FROG	Frequency-resolved optical gating
SHG	Second harmonic generation
THG	Third harmonic generation
SEM	Scanning electron microscope

Bibliography

[1] B. W. J. McNeil and N. R. Thompson, "X-ray free-electron lasers," *Nat. Photon.*, vol. 4, no. 12, pp. 814–821, 2010.

[2] Z. Huang and K. J. Kim, "Review of x-ray free-electron laser theory," *Phys. Rev. ST Accel. Beams*, vol. 10, no. 3, p. 034801, 2007.

[3] C. Pellegrini, A. Marinelli, and S. Reiche, "The physics of x-ray free-electron lasers," *Rev. Mod. Phys.*, vol. 88, no. 1, pp. 1–55, 2016.

[4] Y. Sakai, I. Pogorelsky, O. Williams, F. O'Shea, S. Barber, I. Gadjev, J. Duris, P. Musumeci, M. Fedurin, A. Korostyshevsky, B. Malone, C. Swinson, G. Stenby, K. Kusche, M. Babzien, M. Montemagno, P. Jacob, Z. Zhong, M. Polyanskiy, V. Yakimenko, and J. Rosenzweig, "Observation of redshifting and harmonic radiation in inverse compton scattering," *Phys. Rev. ST Accel. Beams*, vol. 18, no. 6, p. 060702, 2015.

[5] G. Mourou and S. Williamson, "Picosecond electron diffraction," *Appl. Phys. Lett.*, vol. 41, no. 1, pp. 44–45, 1982.

[6] J. Madey, "Stimulated emission of Bremsstrahlung in a Periodic Magnetic Field," *J. Appl. Phys.*, vol. 42, p. 1906, 1971.

[7] L. R. Elias, W. M. Fairbank, J. M. J. Madey, H. A. Schwettman, and T. I. Smith, "Observation of stimulated emission of radiation by relativistic electrons in a spatially periodic transverse magnetic field," *Phys. Rev. Lett.*, vol. 36, no. 13, pp. 717–720, 1976.

[8] D.A.G.Deacon, L.R.Elias, J.M.J.Madey, G.J.Ramian, H.A.Schwettman, and T.I.Smith, "First operation of a free-electron laser," *Phys. Rev. Lett.*, vol. 38, no. 16, pp. 892–894, 1977.

[9] P. Emma, R. Akre, J. Arthur, R. Bionta, C. Bostedt, J. Bozek, A. Brachmann, P. Bucksbaum, R. Coffee, F.-J. Decker, Y. Ding, D. Dowell, S. Edstrom, A. Fisher, J. Frisch, S. Gilevich, J. Hastings, G. Hays, P. Hering, Z. Huang, R. Iverson, H. Loos, M. Messerschmidt, A. Miahnahri, S. Moeller, H.-D. Nuhn,

G. Pile, D. Ratner, J. Rzepiela, D. Schultz, T. Smith, P. Stefan, H. Tompkins, J. Turner, J. Welch, W. White, J. Wu, G. Yocky, and J. Galayda, "First lasing and operation of an ångstrom-wavelength free-electron laser," *Nat. Photon.*, vol. 4, no. 9, pp. 641–647, 2010.

[10] B. D. Patterson, R. Abela, H. H. Braun, U. Flechsig, R. Ganter, Y. Kim, E. Kirk, A. Oppelt, M. Pedrozzi, S. Reiche, L. Rivkin, T. Schmidt, B. Schmitt, V. N. Strocov, S. Tsujino, and A. F. Wrulich, "Coherent science at the swissfel x-ray laser," *New J. Phys.*, vol. 12, p. 035012, 2010.

[11] H. N. Chapman, A. Barty, M. J. Bogan, S. Boutet, S. Frank, S. P. Hau-Riege, S. Marchesini, B. W. Woods, S. Bajt, W. H. Benner, L. W. A., E. Plönjes, M. Kuhlmann, R. Treusch, S. Düsterer, T. Tschentscher, J. R. Schneider, E. Spiller, T. Möller, C. Bostedt, M. Hoener, D. A. Shapiro, K. O. Hodgson, D. van der Spoel, F. Burmeister, M. Bergh, C. Caleman, G. Huldt, M. M. Seibert, F. R. N. C. Maia, R. W. Lee, A. Szöke, N. Timneanu, and J. Hajdu, "Femtosecond diffractive imaging with a soft-x-ray free-electron laser," *Nat. Phys.*, vol. 2, pp. 839–843, 2006.

[12] A. Barty, S. Boutet, M. J. Bogan, S. Hau-Riege, S. Marchesini, K. Sokolowski-Tinten, N. Stojanovic, R. Tobey, H. Ehrke, A. Cavalleri, S. Düsterer, M. Frank, S. Bajt, B. W. Woods, M. M. Seibert, J. Hajdu, R. Treusch, and H. N. Chapman, "Ultrafast single-shot diffraction imaging of nanoscale dynamics," *Nat. Photon.*, vol. 2, p. 415, Jun 2008.

[13] L. Young, E. P. Kanter, B. Kraessig, Y. Li, A. M. March, S. T. Pratt, R. Santra, S. H. Southworth, N. Rohringer, L. F. DiMauro, G. Doumy, C. A. Roedig, N. Berrah, L. Fang, M. Hoener, P. H. Bucksbaum, J. P. Cryan, S. Ghimire, J. M. Glownia, D. A. Reis, J. D. Bozek, C. Bostedt, and M. Messerschmidt, "Femtosecond electronic response of atoms to ultra-intense x-rays," *Nature*, vol. 466, no. 7302, p. 56, 2010.

[14] A. Barty, C. Caleman, A. Aquila, N. Timneanu, L. Lomb, T. A. White, J. Andreasson, D. Arnlund, S. Bajt, T. R. M. Barends, M. Barthelmess, M. J. Bogan, C. Bostedt, J. D. Bozek, R. Coffee, N. Coppola, J. Davidsson, D. P. Deponte, R. B. Doak, T. Ekeberg, V. Elser, S. W. Epp, B. Erk, H. Fleckenstein, L. Foucar, P. Fromme, H. Graafsma, L. Gumprecht, J. Hajdu, C. Y. Hampton, R. Hartmann, A. Hartmann, G. Hauser, H. Hirsemann, P. Holl, M. S. Hunter, L. Johansson, S. Kassemeyer, N. Kimmel, R. A. Kirian, M. Liang, F. R. N. C. Maia, E. Malmerberg, S. Marchesini, A. V. Martin, K. Nass, R. Neutze, C. Reich, D. Rolles, B. Rudek, A. Rudenko, H. Scott, I. Schlichting, J. Schulz, M. M. Seibert, R. L. Shoeman, R. G. Sierra, H. Soltau, J. C. H. Spence, F. Stellato, S. Stern, L. Strüder, J. H. Ullrich, X. Wang,

G. Weidenspointner, U. Weierstall, C. B. Wunderer, and H. N. Chapman, "Self-terminating diffraction gates femtosecond x-ray nanocrystallography measurements," *Nat. Photon.*, vol. 6, no. 1, pp. 35–40, 2012.

[15] B. Rudek, S. K. Son, L. Foucar, S. W. Epp, B. Erk, R. Hartmann, M. Adolph, R. Andritschke, A. Aquila, N. Berrah, C. Bostedt, N. Bozek, Johnand Coppola, F. Filsinger, H. Gorke, T. Gorkhover, H. Graafsma, L. Gumprecht, A. Hartmann, G. Hauser, S. Herrmann, H. Hirsemann, P. Holl, A. Hömke, L. Journel, C. Kaiser, N. Kimmel, F. Krasniqi, K. U. Kühnel, M. Matysek, M. Messerschmidt, D. Miesner, T. Möller, R. Moshammer, K. Nagaya, B. Nilsson, G. Potdevin, D. Pietschner, C. Reich, D. Rupp, G. Schaller, I. Schlichting, C. Schmidt, F. Schopper, S. Schorb, C.-D. Schröter, J. Schulz, M. Simon, H. Soltau, L. Strüder, K. Ueda, G. Weidenspointner, R. Santra, J. Ullrich, A. Rudenko, and D. Rolles, "Ultra-efficient ionization of heavy atoms by intense x-ray free-electron laser pulses," *Nat. Photon.*, vol. 6, pp. 858–865, Nov 2012.

[16] A. Barty, J. Küpper, and H. N. Chapman, "Molecular imaging using x-ray free-electron lasers," *Annu. Rev. Phys. Chem.*, vol. 64, pp. 415–435, Apr. 2013.

[17] B. Erk, R. Boll, S. Trippel, D. Anielski, L. Foucar, B. Rudek, S. W. Epp, R. Coffee, S. Carron, S. Schorb, K. R. Ferguson, M. Swiggers, J. D. Bozek, M. Simon, T. Marchenko, J. Küpper, I. Schlichting, J. Ullrich, C. Bostedt, D. Rolles, and A. Rudenko, "Imaging charge transfer in iodomethane upon x-ray photoabsorption.," *Science*, vol. 345, pp. 288–291, July 2014.

[18] C. Bostedt, S. Boutet, D. M. Fritz, Z. Huang, H. J. Lee, H. T. Lemke, A. Robert, W. F. Schlotter, J. J. Turner, and G. J. Williams, "Linac coherent light source: The first five years," *Rev. Mod. Phys.*, vol. 88, no. 1, 2016.

[19] K. J. Kim, "Brightness, coherence and propagation characteristics of synchrotron radiation," *Nucl. Instrum. Meth. A*, vol. 246, no. 1-3, pp. 71–76, 1986.

[20] S. Reiche, P. Musumeci, C. Pellegrini, and J. B. Rosenzweig, "Development of ultra-short pulse, single coherent spike for sase x-ray fels," *Nucl. Instrum. Meth. A*, vol. 593, no. 1-2, pp. 45–48, 2008.

[21] W. Bertozzi, J. A. Caggiano, W. K. Hensley, M. S. Johnson, S. E. Korbly, R. J. Ledoux, D. P. McNabb, E. B. Norman, W. H. Park, and G. A. Warren, "Nuclear resonance fluorescence excitations near 2 mev in u235 and pu239," *Physical Review C - Nuclear Physics*, vol. 78, no. 4, p. 041601, 2008.

[22] W. S. Graves, F. X. Kärtner, D. E. Moncton, and P. Piot, "Intense superradiant x rays from a compact source using a nanocathode array and emittance exchange.," *Phys. Rev. Lett.*, vol. 108, p. 263904, jun 2012.

[23] H. Ihee, V. Lobastov, U. Gomez, B. Goodson, R. Srinivasan, C. Ruan, and A. H. Zewail, "Direct imaging of transient molecular structures with ultrafast diffraction," *Science*, vol. 291, pp. 458–462, Jan 2001.

[24] B. J. Siwick, J. R. Dwyer, R. E. Jordan, and R. J. D. Miller, "An atomic-level view of melting using femtosecond electron diffraction," *Science*, vol. 302, pp. 1382–1385, Jan 2003.

[25] M. Gulde, S. Schweda, G. Storeck, M. Maiti, H. K. Yu, A. M. Wodtke, S. Schäfer, and C. Ropers, "Ultrafast low-energy electron diffraction in transmission resolves polymer/graphene superstructure dynamics," *Science*, vol. 345, pp. 200–204, July 2014.

[26] J. Yang, M. Guehr, X. Shen, R. Li, T. Vecchione, R. Coffee, J. Corbett, A. Fry, N. Hartmann, C. Hast, K. Hegazy, K. Jobe, I. Makasyuk, J. Robinson, M. S. Robinson, S. Vetter, S. Weathersby, C. Yoneda, X. Wang, and M. Centurion, "Diffractive imaging of coherent nuclear motion in isolated molecules," *Phys. Rev. Lett.*, vol. 117, p. 153002, Oct. 2016.

[27] M. C. Thompson, H. Badakov, A. M. Cook, J. B. Rosenzweig, R. Tikhoplav, G. Travish, I. Blumenfeld, M. J. Hogan, R. Ischebeck, N. Kirby, R. Siemann, D. Walz, P. Muggli, A. Scott, and R. B. Yoder, "Breakdown limits on gigavolt-per-meter electron-beam-driven wakefields in dielectric structures," *Phys. Rev. Lett.*, vol. 100, no. 21, p. 214801, 2008.

[28] R. J. England, R. J. Noble, Z. Wu, and M. Qi, "Dielectric laser acceleration," *Rev. Mod. Phys.*, vol. 86, no. December, pp. 1337–1389, 2014.

[29] F. X. Kärtner, F. Ahr, A. L. Calendron, H. Çankaya, S. Carbajo, G. Chang, G. Cirmi, K. Dörner, U. Dorda, A. Fallahi, A. Hartin, M. Hemmer, R. Hobbs, Y. Hua, W. R. Huang, R. Letrun, N. Matlis, V. Mazalova, O. D. Mücke, E. Nanni, W. Putnam, K. Ravi, F. Reichert, I. Sarrou, X. Wu, A. Yahaghi, H. Ye, L. Zapata, D. Zhang, C. Zhou, R. J. D. Miller, K. K. Berggren, H. Graafsma, A. Meents, R. W. Assmann, H. N. Chapman, and P. Fromme, "Axsis: Exploring the frontiers in attosecond x-ray science, imaging and spectroscopy," *Nucl. Instrum. Meth. A*, vol. 829, pp. 24–29, 2016.

[30] A. Fallahi, M. Fakhari, A. Yahaghi, M. Arrieta, and F. X. Kärtner, "Short electron bunch generation using single-cycle ultrafast electron guns," *Phys. Rev. ST Accel. Beams*, vol. 19, no. 1–8, p. 081302, 2016.

[31] D. H. Dowell and S. Linear, "Lecture 2: electron emission and cathode emittance," pp. 1–24.

[32] P. B. Corkum, "Plasma perspective on strong-field multiphoton ionization," *Phys. Rev. Lett.*, vol. 71, pp. 1994–1997, 1993.

[33] M. Krüger, M. Schenk, and P. Hommelhoff, "Attosecond control of electrons emitted from a nanoscale metal tip," *Nature*, vol. 475, pp. 78–81, jul 2011.

[34] A. Mustonen, P. Beaud, E. Kirk, T. Feurer, and S. Tsujino, "Five picocoulomb electron bunch generation by ultrafast laser-induced field emission from metallic nano-tip arrays," *Astrophys. Lett. & Comm.*, vol. 99, p. 103504, 2011.

[35] W. P. Putnam, R. G. Hobbs, P. D. Keathley, K. K. Berggren, and F. X. Kärtner, "Optical-field-controlled photoemission from plasmonic nanoparticles," *Nat. Phys.*, vol. 13, pp. 335–339, Dec. 2016.

[36] S. Tsujino, P. Das Kanungo, M. Monshipouri, C. Lee, and R. D. Miller, "Measurement of transverse emittance and coherence of double-gate field emitter array cathodes," *Nat. Commun.*, vol. 7, p. 13976, 2016.

[37] H. Wiedemann, *Particle Accelerator Physics*. 2015.

[38] M. Reiser, *Theory and Design of Charged Particle Beams*. WILEY-VCH Verlag GmbH & Co. KGaA, Weinheim, 2008.

[39] S. Lee, *Accelerator Physics*. World Scientific Publishing Co. Pte. Ltd, 2015.

[40] D. H. Dowell and J. F. Schmerge, "Quantum efficiency and thermal emittance of metal photocathodes," *Phys. Rev. ST Accel. Beams*, vol. 12, p. 074201, July 2009.

[41] T. Rao and D. H. Dowell, *An Engineering Guide to Photoinjectors*. 2013.

[42] J. Rosenzweig, A. Cahill, V. Dolgashev, C. Emma, A. Fukusawa, C. L. R. Li, J. Maxson, P. Musumeci, A. Nause, R. Pakter, R. Pompili, R. Roussel, B. Spataro, and S. Tantawi, "Next generation high brightness electron beams from ultra-high field cryogenic radiofrequency photocathode sources," 2018.

[43] P. Hawkes and E. Kasper, *Principles of Electron Optics*. 1996.

[44] J. C. H. Spence, *High-Resolution Electron Microscopy*. 2013.

[45] A. Damascelli, "Angle-resolved photoemission studies of the cuprate superconductors," *Rev. Mod. Phys.*, vol. 75, no. April, p. 473, 2003.

[46] S. Karkare, L. Cultrera, Y.-W. Hwang, R. Merluzzi, and I. Bazarov, "2-D energy analyzer for low energy electrons," *Rev. Sci. Instrum.*, vol. 86, p. 033301, Mar. 2015.

[47] I. Bazarov, L. Cultrera, A. Bartnik, B. Dunham, S. Karkare, Y. Li, X. Liu, J. Maxson, and W. Roussel, "Thermal emittance measurements of a cesium potassium antimonide photocathode," *Astrophys. Lett. & Comm.*, vol. 98, no. 22, 2011.

[48] W. J. Engelen, E. P. Smakman, D. J. Bakker, O. J. Luiten, and E. J. D. Vredenbregt, "Effective temperature of an ultracold electron source based on near-threshold photoionization," *Ultramicroscopy*, vol. 136, pp. 73–80, 2014.

[49] M. Zhang, "Emittance formula for slits and pepper-pot measurement," vol. 26, 1996.

[50] J. Feng, J. Nasiatka, W. Wan, T. Vecchione, and H. A. Padmore, "A novel system for measurement of the transverse electron momentum distribution from photocathodes a novel system for measurement of the transverse electron momentum distribution from photocathodes," *Rev. Sci. Instrum.*, vol. 86, p. 015103, 2015.

[51] A. T. J. B. Eppink and D. H. Parker, "Velocity map imaging of ions and electrons using electrostatic lenses: Application in photoelectron and photofragment ion imaging of molecular oxygen," *Rev. Sci. Instrum.*, vol. 68, no. 9, pp. 3477–3484, 1997.

[52] J. Mikosch, S. Trippel, C. Eichhorn, R. Otto, U. Lourderaj, J. X. Zhang, W. L. Hase, M. Weidemüller, and R. Wester, "Imaging nucleophilic substitution dynamics," *Science*, vol. 319, no. 5860, pp. 183–186, 2008.

[53] A. I. Chichinin, K. H. Gericke, S. Kauczok, and C. Maul, "Imaging chemical reactions — 3d velocity mapping," *Int. Rev. Phys. Chem.*, vol. 28, no. 4, pp. 607–680, 2009.

[54] G. Fraser, "The electron detection efficiency of microchannel plates," *Nuclear Instruments and Methods*, vol. 206, pp. 445–449, 1983.

[55] G. M. Rossi, L. Wang, R. E. Mainz, H. Çankaya, F. X. Kärtner, and G. Cirmi, "Cep dependence of signal and idler upon pump-seed synchronization in optical parametric amplifiers," *Opt. Lett.*, vol. 43, no. 2, pp. 178–181, 2018.

[56] M. Bellini and T. W. Hänsch, "Phase-locked white-light continuum pulses: toward a universal optical frequency-comb synthesizer," *Opt. Lett.*, vol. 25, no. 14, p. 1049, 2000.

[57] G. Cerullo and S. De Silvestri, "Ultrafast optical parametric amplifiers," *Rev. Sci. Instrum.*, vol. 74, no. 1 I, pp. 1–18, 2003.

[58] Scientific Instrument Services Inc., USA, "Simion 8.1," 2011. URL: `http://simion.com`.

[59] COMSOL Multiphysics v. 5.3. `http://www.comsol.com`. COMSOL AB, Stockholm, Sweden.

[60] N. L. M. Müller, S. Trippel, K. Długołęcki, and J. Küpper, "Electron gun for diffraction experiments on controlled molecules," *J. Phys. B*, vol. 48, p. 244001, Nov. 2015.

[61] H. Lee, S. Karkare, L. Cultrera, A. Kim, and I. V. Bazarov, "Review and demonstration of ultra-low-emittance photocathode measurements," *Rev. Sci. Instrum.*, vol. 86, no. 7, p. 073309, 2015.

[62] H. Hertz, "Ueber einen einfluss des ultravioletten lichtes auf die electrische entladung," *Annalen der Physik*, vol. 267, pp. 983–1000, june 1887.

[63] A. Einstein, "Über einen die erzeugung und verwandlung des lichtes betreffenden heuristischen gesichtspunkt," *Annalen der Physik*, vol. 322.

[64] D. E. Eastman, "Photoelectric work functions of transition, rare-earth, and noble metals," *Phys. Rev. B*, vol. 2, no. 1, pp. 1–2, 1970.

[65] C. N. Berglund and W. E. Spicer, "Photoemission studies of copper and silver: Theory," *Phys. Rev.*, vol. 136, no. 4A, p. A1030, 1964.

[66] C. N. Berglund and W. E. Spicer, "Photoemission studies of copper and silver: Experiment," *Phys. Rev.*, vol. 136, no. 1953, pp. A1044–A1064, 1964.

[67] W. F. Krolikowski and W. E. Spicer, "Photoemission studies of the noble metals. i. copper," *Phys. Rev. B*, vol. 185, no. 3, pp. 882–900, 1969.

[68] W. F. Krolikowski and W. E. Spicer, "Photoemission studies of the noble metals. ii. gold," *Phys. Rev. B*, vol. 1, no. 2, pp. 478–487, 1970.

[69] G. S. Voronov and N. B. Delone, "Many-photon ionization of the xenon atom by ruby laser radiation," *Soviet Physics JETP*, vol. 23, no. 1, pp. 78–84, 1966.

[70] H. B. Bebb and A. Gold, "Multiphoton ionization of hydrogen and rare-gas atoms," *Phys. Rev.*, vol. 143, no. 1, pp. 1–24, 1966.

[71] P. Agostini, F. Fabre, G. Mainfray, G. Petite, and N. K. Rahman, "Free-free transitions following six-photon ionization of xenon atoms," *Phys. Rev. Lett.*, vol. 42, no. 17, pp. 1127–1130, 1979.

[72] S. Luan, R. Hippler, H. Schwier, and H. Lutz, "Electron emission from polycrystalline copper surfaces by multi-photon absorption," *Europhys. Lett.*, vol. 9, no. 5, pp. 489–494, 1989.

[73] R. H. Fowler and L. Nordheim, "Electron emission in intense electric fields," *Proceedings of the Royal Society A: Mathematical, Physical and Engineering Sciences*, vol. 119, pp. 173–181, may 1928.

[74] Z. Pei and C. N. Berglund, "Angular distribution of photoemission from gold thin films," *Jpn. J. Appl. Phys.*, vol. 41, no. 1 A/B, pp. L52–L54, 2002.

[75] R. T. Poole, R. C. G. Leckey, J. G. Jenkin, and J. Liesegang, "Photoelectron angular distribution from gold," *J. Elec. Spec. Rel. Phen.*, vol. 2, pp. 371–376, 1972-1973.

[76] A. Damascelli, G. Gabetta, A. Lumachi, L. Fini, and F. Parmigiani, "Multi-photon electron emission from Cu and W: An angle-resolved study.," *Phys. Rev. B*, vol. 54, no. 9, pp. 6031–6034, 1996.

[77] D. R. Lide, *CRC Handbook of Chemistry and Physics*. CRC Press, 84 ed., 2003.

[78] M. N. Polyanskiy, "Refractive index database." `https://refractiveindex.info`, 2017. Accessed on 24. July 2017.

[79] C. J. Dasch, "One-dimensional tomography: a comparison of Abel, onion-peeling, and filtered backprojection methods," *Applied Optics*, vol. 31, no. 8, p. 1146, 1992.

[80] W. S. Fann, R. Storz, H. W. K. Tom, and J. Bokor, "Direct measurement of nonequilibrium electron-energy distributions in sub-picosecond laser-heated gold films," *Phys. Rev. Lett.*, vol. 68, pp. 2834–2837, 1992.

[81] W. S. Fann, R. Storz, H. W. K. Tom, and J. Bokor, "Electron thermalization in gold," *Phys. Rev. B*, vol. 46, no. 20, pp. 13592–13595, 1992.

[82] M. Aeschlimann, C. A. Schmuttenmaer, H. E. Elsayed-Ali, R. J. D. Miller, J. Cao, Y. Gao, and D. A. Mantell, "Observation of surface enhanced multi-photon photoemission from metal surfaces in the short pulse limit," *J. Chem. Phys.*, vol. 102, no. 21, pp. 8606–8613, 1995.

[83] J. Fujimoto, J. Liu, E. Ippen, and N. Bloembergen, "Femtosecond laser interaction with metallic tungsten and nonequilibrium electron and lattice temperatures," *Phys. Rev. Lett.*, vol. 53, pp. 1837–1840, 1984.

[84] F. Banfi, C. Giannetti, G. Ferrini, G. Galimberti, S. Pagliara, D. Fausti, and F. Parmigiani, "Experimental evidence of above-threshold photoemission in solids," *Phys. Rev. Lett.*, vol. 94, no. 3, p. 037601, 2005.

[85] W. Schottky, "über den einfluss von strukturwirkungen, besonders der thomsonschen bildkraft, auf die elektronenemission der metalle," *Phys. Zeitschr.*, vol. 15, pp. 872–879, 1914.

[86] H. Jeffreys, "On ceetain approximate solutions of linear differential equations of the second oeder," *Proceedings of the London Mathematical Society*, vol. 23, pp. 428–436, 1924.

[87] E. L. Murphy and R. H. Good, "Thermionic emission, field emission, and the transition region," *Phys. Rev.*, vol. 102, no. 6, pp. 1464–1473, 1956.

[88] P. A. Chatterton, "A theoretical study of field emission initiated vacuum breakdown," *Proceedings of the Physical Society*, vol. 88, no. 1, p. 231, 1966.

[89] A. Polyakov, C. Senft, K. F. Thompson, J. Feng, S. Cabrini, P. J. Schuck, H. A. Padmore, S. J. Peppernick, and W. P. Hess, "Plasmon-enhanced photocathode for high brightness and high repetition rate x-ray sources," *Phys. Rev. Lett.*, vol. 110, p. 076802, 2013.

[90] R. K. Li, H. To, G. Andonian, J. Feng, A. Polyakov, C. M. Scoby, K. Thompson, W. Wan, H. A. Padmore, and P. Musumeci, "Surface-plasmon resonance-enhanced multiphoton emission of high-brightness electron beams from a nanostructured copper cathode," *Phys. Rev. Lett.*, vol. 110, no. 7, p. 074801, 2013.

[91] K. C. Kulander, K. Schafer, and J. Krause, *Super-Intense Laser-Atom Physics*, vol. 316 of the NATO Advanced Study Institue Series book series. 1993.

[92] K. J. Schafer, B. Yang, L. F. Dimauro, and K. C. Kulander, "Above threshold ionization beyond the high harmonic cutoff," *Phys. Rev. Lett.*, vol. 70, no. 11, pp. 1599–1602, 1993.

[93] F. Krausz and M. Ivanov, "Attosecond physics," *Rev. Mod. Phys.*, vol. 81, pp. 163–234, feb 2009.

[94] M. Busuladžić, A. Gazibegović-Busuladžić, and D. B. Milošević, "High-order above-threshold ionization in a laser field: Influence of the ionization potential on the high-energy cutoff," *Laser Physics*, vol. 16, no. 2, pp. 289–293, 2006.

[95] M. Stei, J. von Vangerow, R. Otto, A. H. Kelkar, E. Carrascosa, T. Best, and R. Wester, "High resolution spatial map imaging of a gaseous target," *J. Chem. Phys.*, vol. 138, p. 214201, 2013.

[96] G. Herink, D. R. Solli, M. Gulde, and C. Ropers, "Field-driven photoemission from nanostructures quenches the quiver motion.," *Nature*, vol. 483, pp. 190–193, mar 2012.

[97] M. Kozák, T. Eckstein, N. Schönenberger, and P. Hommelhoff, "Inelastic ponderomotive scattering of electrons at a high-intensity optical travelling wave in vacuum," *Nature Physics*, vol. 14, no. October 2017, pp. 121–126, 2017.

[98] P. Dombi, A. Hörl, P. Rácz, I. Márton, A. Trügler, J. R. Krenn, and U. Hohenester, "Ultrafast strong-field photoemission from plasmonic nanoparticles," *Nano Letters*, vol. 13, pp. 674–678, 2013.

[99] G. Sciaini and R. J. D. Miller, "Femtosecond electron diffraction: heralding the era of atomically resolved dynamics," *Rep. Prog. Phys.*, vol. 74, no. 9, p. 096101, 2011.

[100] M. Hattass, T. Jahnke, S. Schössler, A. Czasch, M. Schöffler, L. P. H. Schmidt, B. Ulrich, O. Jagutzki, F. O. Schumann, C. Winkler, J. Kirschner, R. Dörner, and H. Schmidt-Böcking, "Dynamics of two-electron photoemission from Cu(111)," *Phys. Rev. B*, vol. 77, no. 16, p. 165432, 2008.

[101] A. Evtukh, H. Hartnagel, O. Yilmazoglu, H. Mimura, and D. Pavlidis, *Vacuum Nanoelectronic Devices: Novel Electron Sources and Applications*. Wiley, 2015.

[102] T. Wang, J. Guo, J. Shao, T. Sun, A. Chen, H. Liu, and D. Ding, "Heating process and damage threshold analysis of Au film coated on Cu substrate for femtosecond laser," *Optics and Laser Technology*, vol. 44, no. 5, pp. 1551–1555, 2012.

Erklärung der Urheberschaft

Ich versichere an Eides statt, dass ich die Dissertation im Studiengang Physik selbstständig verfasst und keine anderen als die angegebenen Hilfsmittel – insbesondere keine im Quellenverzeichnis nicht benannten Internet-Quellen – benutzt habe. Alle Stellen, die wörtlich oder sinngemäß aus Veröffentlichungen entnommen wurden, sind als solche kenntlich gemacht. Ich versichere weiterhin, dass ich die Arbeit vorher nicht in einem anderen Prüfungsverfahren eingereicht habe und die eingereichte schriftliche Fassung der auf dem elektronischen Speichermedium entspricht.

Ort, Datum Unterschrift

Erklärung zur Veröffentlichung

Ich erkläre mein Einverständnis mit der Einstellung dieser Dissertation in den Bestand der Bibliothek.

Ort, Datum Unterschrift